EXPERIMENTAL AND MODELING INVESTIGATIONS OF BIOMASS PARTICLE COMBUSTION

by

Hong Lu

A dissertation submitted to the faculty of

Brigham Young University

in partial fulfillment of the requirements for the degree of

Doctor of Philosophy

Department Chemical Engineering

Brigham Young University

December 2006

BRIGHAM YOUNG UNIVERSITY

GRADUATE COMMITTEE APPROVAL

of a dissertation submitted by

Hong Lu

This dissertation has been read by each member of the following graduate committee and by majority vote has been found to be satisfactory.

Date	Larry L. Baxter, Chair
Date	Thomas H. Fletcher
Date	William C. Hecker
Date	Calvin H. Bartholomew
Date	Merrill W. Beckstead

BRIGHAM YOUNG UNIVERSITY

As chair of the candidate's graduate committee, I have read the dissertation of Hong Lu in its final form and have found that (1) its format, citations, and bibliographical style are consistent and acceptable and fulfill university and department style requirements; (2) its illustrative materials including figures, tables, and charts are in place; and (3) the final manuscript is satisfactory to the graduate committee and is ready for submission to the university library.

Date

Larry L. Baxter
Chair, Graduate Committee

Accepted for the Department

W. Vincent Wilding
Department Chair

Accepted for the College

Alan R. Parkinson
Dean, Ira A. Fulton College of Engineering and Technology

ABSTRACT

EXPERIMENTAL AND MODELING INVESTIGATIONS OF

BIOMASS PARTICLE COMBUSTION

Hong Lu

Department of Chemical Engineering

Doctor of Philosophy

This investigation provides a comprehensive analysis of entrained-flow biomass combustion processes. Experimental and theoretical investigations indicate how particle shape and size influence biomass combustion rates. Experimental samples include flake-like, cylinder-like, and equant (nearly spherical) shapes with similar particle masses and volumes but different surface areas. Samples of small (less than 500 μm) particles were passed through a laboratory entrained-flow reactor in a nitrogen/air atmosphere and a maximum reactor wall temperature of 1600 K, while large samples were reacted in suspension in a single particle furnace operated at similar conditions as the entrained-flow reactor. A separately developed computer and image analysis system was used to determine particle surface-area-to-volume ratios based on three orthogonal particle silhouettes. Experimental data indicate that equant (spherical) particles react more slowly than the other shapes, with the conversion time ratio required for complete

combustion becoming greater as particle mass increases and reaching a factor of two or more for particles larger than 1 mm in diameter (which includes most particles in commercial application).

A color-band, non-contact pyrometer developed in this project measured particle surface temperatures and flame temperatures during pyrolysis and char burning processes. This technique employs widely available and relative inexpensive cameras and detectors. The camera-measured temperature data agree with black body calibration data within the accuracy of the data (± 20°C) and with thermocouple-measured data and model predictions within the repeatability of the data (± 50 °C) in most cases.

A one-dimensional, transient particle combustion model simulates the drying, pyrolysis, and char oxidation and gasification processes of particles with different shapes. The model also predicts the shrinking/swelling and surrounding flame combustion behaviors of a single particle. Model simulations of the three shapes agree nearly within experimental uncertainty with the data. For biomass particle devolatilization processes, model predictions extended to a wider range of sizes predict the effects of shape and size on yields and overall mass conversion rates. The near-spherical particle loses mass most slowly and its conversion time significantly differs from those of flake-like particles and cylinder-like particles as particle equivalent diameter increases. Little difference exists between cylinder- and plate-like particles.

ACKNOWLEDGEMENTS

I wish to express my sincere thanks to those who helped in completion of this thesis. First of all I would like to thank my advisor, Professor Larry Baxter, for his kind guidance, helpful suggestions, and encouragement. Truly concerned for welfare of others and committed to excellence in both research and teaching, he is a leader in engineering education. I would like to thank Dr. Thomas Fletcher for his assistance in the particle combustion model development and Dr. Hecker for discussions in char oxidation kinetics. Appreciation is also expressed to Dr. Dale Tree for suggestions and discussions in the color-band pyrometry development and the entrained-flow reactor design.

Financial support from various offices of DOE and Sandia National Laboratories is gratefully acknowledged.

Thanks go to Elvin Ip, Warren Roberts, and Andrew Mackrory for their help and valuable discussions. It's a great experience to work with them. Contributions of my other co-workers for this project are also greatly appreciated: Luke Werret, Justin Scott, Gregory Peirce, Kelly Echols, Paul Foster, Bryan Ripa, and Todd Gunderson.

I would like to thank my mom, Changyu Qu, and my parents-in-law, Zhihuang Zhao and Zhongliu Li, without whose assistance and encouragement this work would not have been possible.

Finally and most importantly, I would like to thank my wife, Yi Li, for her love, understanding, support, and encouragement.

TABLE OF CONTENTS

LIST OF FIGURES

LIST OF TABLES

NOMENCLATURE

a	—	Pixel/cell area of CCD or CMOS sensor, m^2 Ash content,
A	—	Pre-exponential factor, s^{-1}; area, m^2;
AR	—	Aspect ratio, /
B	—	Radiance, $W.Sr^{-1}.m^{-2}.nm^{-1}$
BLT	—	Boundary layer thickness, m
C_1, C_2	—	Constants in Planck's law
Cp	—	Heat capacity, $J.kg^{-1}.K^{-1}$
d	—	Working distance, m
d_{pore}	—	Pore diameter, m
D	—	Lens diameter, m
D_{eff}	—	Effective diffusivity, $m^2.s^{-1}$
D_{AB}	—	Molecular diffusivity, $m^2.s^{-1}$
D_K	—	Knudson diffusivity, $m^2.s^{-1}$
DN	—	Digital number / pixel intensity,
E	—	Photon energy, J Irradiance on sensor, $W.nm^{-1}$
E_i	—	Activation energy, $J.mol^{-1}$
F	—	Geometric configuration factor,

g	—	Camera gain value,
h	—	Planck's constant, 6.626068×10^{-34} $m^2.kg.s^{-1}$
h_f	—	Heat transfer coefficient, $W.m^{-1}.K^{-1}$
h_m	—	Mass transfer coefficient, $m.s^{-1}$
$\hat{H}$	—	Enthalpy, $J.kg^{-1}$
k	—	Rate constant, devolatilization reaction — s^{-1}; heterogeneous reaction — $m.s^{-1}$
K	—	Thermal conductivity, W/m.s
M	—	Molecular weight, $kg.kmol^{-1}$
M_W	—	Gas average molecular weight, $kg.kmol^{-1}$
n	—	Shape factor
Nu	—	Nusselt number,
p	—	Pressure, Pa
Pr	—	Prandtl number,
q	—	Radiant energy flux, $J.m^{-2}$
r	—	Radius coordinate, m Reaction rate, $kg.m^{-3}.s^{-1}$
Re	—	Reynolds number
R, R_g	—	Universal gas constant, $J.mol^{-1}.K^{-1}$
Rp	—	Particle radius, m
R_{SA}	—	Surface area ratio,
t	—	Time, s
S_a	—	Particle specific surface area, $m^2.m^{-3}$
SA	—	Surface area, m^2

S_i — Source term in conservation equation

T — Temperature, K

u — Gas velocity, $m.s^{-1}$

v — Volume, m^3

x — Conversion,

X — Area ratio of effective sensor over light source,

Y — Mass fraction,

Z — Third coordinate of reconstructed particle surface point, m

Greek symbols

α — Proportional factor,

β — Particle/droplet swelling/shrinking factor,

ε — Porosity,

γ — Gas specific heat ratio,

μ — Viscosity, Pa.s

η — Permeability, Darcy

λ — Wavelength, nm

θ — Blowing factor,

ρ — Density, $kg.m^{-3}$

σ — Stefan-Boltzman constant, $W.m^{-2}.K^{-4}$

ω — Emissivity,

τ — Transmitter,

Ω — Solid angle, Sr

ΔH — Heat of reaction, $J.kg^{-1}$

Δt	_	Camera exposure time, s

Subscript

0	_	Initial value or reference state
A	_	Ash
B	_	Biomass
C	_	Char
con	_	Conductivity
eq.	_	Equivalent
g	_	Gas phase
G	_	Light gas
HC	_	Hydrocarbon
i	_	Species or component in solid phase
j	_	Species or component in gas phase
k	_	Species or component in liquid phase
I	_	Inert gas
M	_	Moisture
p	_	Particle
rad	_	Radiation
V	_	Water vapor
T	_	Tar
w	_	Wall

1. Introduction

During the last two decades, a interest has grown in renewable energy sources. There are two driving forces for this interest: (1) the increasing concern about the environmental impact of fossil and nuclear energy sources; and (2) the increasing anxiety regarding the security and longevity of fossil fuel.

The threat of regional and global climate change (global warming) may require significant reduction in the emissions of greenhouse gases — most notably CO_2. One potential strategy for reducing such emissions is the replacement of fossil fuels with renewable biomass fuels. Renewable fuels can be essentially CO_2-neutral (considering the carbon cycle in the atmosphere) if derived from sustainable cultivation practices with minimal fossil fuel usage. Unlike fossil fuels, biomass fuels can be renewable and CO_2-neutral in the sense that the CO_2 generated by biomass utilization is removed from the atmosphere by the plants that replace the fuel, closing the carbon loop on a short timescale. If the biomass is renewably produced (as is generally the case in developed nations), there is little net increase in atmospheric CO_2 content. Since most biomass, including essentially all biomass residue, decays in any case, often producing methane and other decomposition products that greatly exceed the potency of CO_2 as greenhouse gases, use of biomass residues as fuel has the potential of actually decreasing greenhouse gas impacts, not just being neutral (Mann, 2001).

Today, various forms of biomass energy account for nearly 3 % of all energy consumed in the U.S., and 47 % of renewable energy used in the U.S (EIA, 2003), as illustrated in Figure 1.

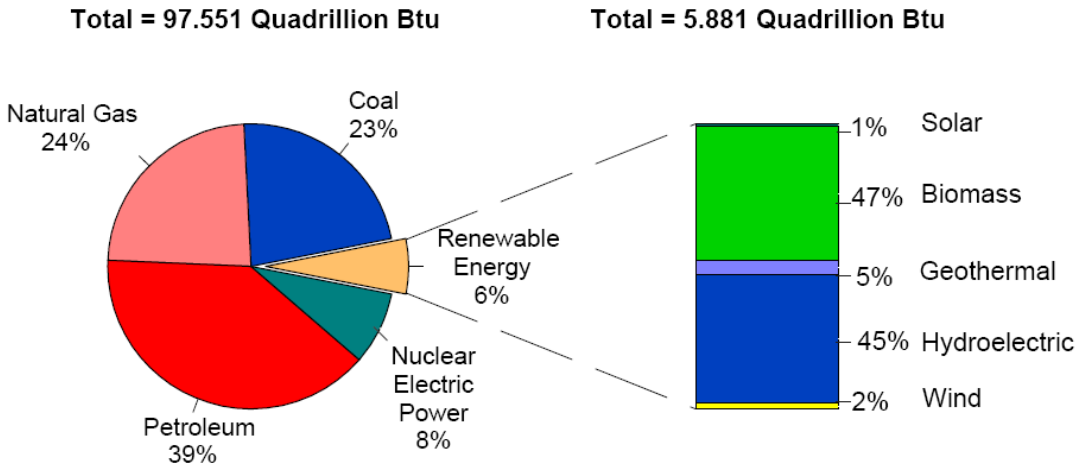

Figure 1 The role of renewable energy consumption in energy supply of US, 2002 (EIA, 2003)

Biomass represents about 80 % of non-hydro renewable energy generated in the US. Additionally, biomass energy represents among the least costly renewable energy options in many cases (Baxter, 2005). Biomass meets a variety of energy needs, including generating electricity, heating homes, and providing process heat for industrial facilities. Biomass can be utilized with the following approaches:

- Direct combustion to produce steam and generate electricity;
- Gasification to produce combustible gas, which may drive a high-efficiency, combined-cycle gas turbine if current technical roadblocks are resolved;
- Pyrolysis to obtain pyrolysis oil and different kinds of chemicals;

- Thermal or chemical conversion to transportation fuels, such as ethanol, methanol, and Fischer-Tropsch fuels.

Of these uses, by far the largest use is conversion to steam for process use and power generation.

For biomass to achieve its potential as an energy resource, further research is needed throughout the biomass energy production chain from plant genetics to fuel processing (Baxter, 2005). This is due to a major problem: the relatively low power generation efficiency of biomass power plants (typically 12~25%, but 33~38% for cofiring in a coal-fired power plant), which partially makes biomass energy more expensive than fossil fuel energy. Therefore, new approaches are likely required to substantially increase the efficiency of the conversion of biomass to heat and power. The identification and design of these novel approaches require fundamental understanding of the unique combustion characteristics of biomass fuels.

Coal combustion research represents a relatively mature science in that a lot of promising models have been developed to describe coal devolatilization and oxidation processes, and comprehensive models and CFD codes are available to predict the performance of coal-fired boilers. However it is unreasonable to apply these models directly for biomass combustion, since biomass is much different from coal in both physical and combustion properties.

Some major property differences between biomass and coal are listed in Table 1 (Baxter, 2000).

All of these major property differences make biomass combustion behavior dramatically different from that of coal. Advanced high-efficiency biomass conversion

technologies may take advantage of some of the unique biomass characteristics but further research is needed.

Table 1 Properties comparison of coal and biomass fuel (Baxter, 2000)

	Density (kg/m^3)	Size (mm)	Shape	H/C (molar)	O/C (molar)	Heating value (MJ/kg) (daf)	Volatile (%) (daf)
Coal	~1300	~0.1	spherical	~0.8	0.02~0.4	~25	40+
Biomass	~500	~3.0	irregular	~1.5	0.4~1.0	~16	80+

The large variations in biomass particle sizes and shapes play significant roles in biomass combustion. For small size particles, such as pulverized coal, the Biot number (hL/k) is generally much less than one, justifying the assumption of uniform intra-particle temperature and concentration distributions. But biomass particles, with a typical size of 3 mm and particle-gas heat transfer coefficient of 30 W/m K generally have Biot numbers of about 0.8, which makes the uniform temperature and concentration distribution assumption no longer valid during combustion. Larger particle sizes establish the potential for large internal temperature and composition gradients (Lu et al., 2006), which fact complicates combustion models.

Furthermore, various particle shapes result in different particle exterior surface area to volume ratios and non-uniform heat fluxes in the particle, which can further affect the devolatilization and oxidation rates. Figure 2 shows the surface area ratios of aspherical particles to spherical particles with the same volume, plotted as a function of aspect ratio. Both cylinders and plates have higher surface-area-to-mass ratios than spheres, and the

difference increases with increasing aspect ratio. At high-temperature and high-heating-rate conditions in entrained-flow systems, these phenomena may play significant roles in the overall conversion process. Therefore, particle shape strongly impacts commercial biomass conversion systems, and fundamental investigations are required.

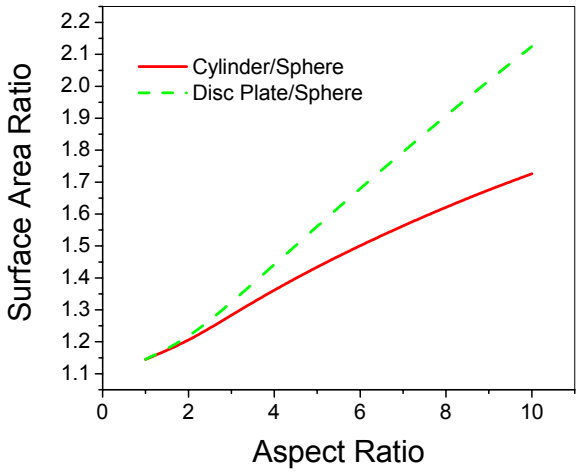

Figure 2 Surface area ratios of aspherical particles to spherical particles with the same volume, plotted as a function of aspect ratio

2. Literature Review

This literature review is divided into four sections. Section 1 describes biomass composition and chemical structure. In Section 2, the pyrolysis mechanisms and kinetics of biomass and biomass components are summarized, including biomass particle conversion models. Section 3 discusses influences of various factors on biomass pyrolysis, including temperature, heating rate, particle size and shape, and inorganic contents. Section 4 discusses biomass char oxidation processes, char reactivity and related issues. Section 5 summarizes the current state of knowledge and discusses areas needing attention.

2.1. Biomass Composition

Biomass contains many compounds, but the dominant chemical species can be categorized as cellulose, hemicellulose, and lignin. Several minor components, including lignans, volatile oils, tannins, resins, proteins, etc. complete the organic fraction of the fuel. The inorganic fractions include both biologically active materials, such as potassium and chlorine, particulate materials biologically incorporated into the plant, such as silica, and adventitious material included in the form of soil, process-related compounds such as clay in paper, and often impurities unrelated to biomass itself ranging from wastes (nails, paint, bottles, pipes, refrigerators, etc.) to process or shipping components (bale wires,

mill blades, etc.). As a group, the inorganic materials represent ash-forming components. Each of these major components is discussed separately below.

2.1.1. Cellulose

Cellulose represents about 50 wt% of biomass, ranging from about 30 wt% for some trees and nut shells to over 90 wt% for cotton balls and similar materials. Cellulose is typically comprised of less than 10,000 anhydroglucose units (indicated in Figure 3), containing 49 wt% oxygen. Its chemical formula is $(C_6H_{10}O_5)_n$, and there are covalent bond, hydrogen bond and Van Der Waal forces within the polymer. It is a glucose-based polysaccharide, illustrated below in Figure 3. A note of passing significance to this project is that the mer of a cellulose polymer contains two, not one, glucose units because of the geometric arrangement of the units relative to one another.

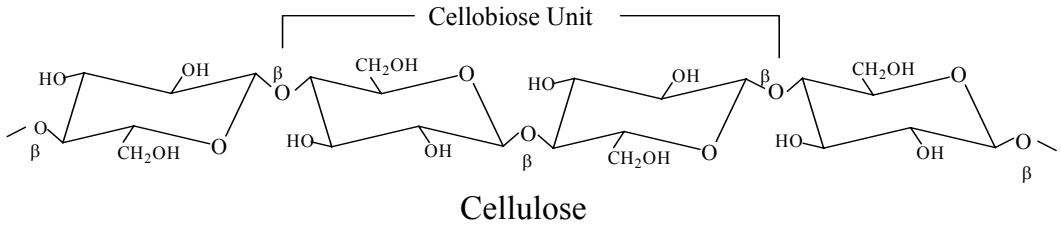

Cellulose

Figure 3 Chemical structure of cellulose
(Northey, 1998)

2.1.2. Hemicellulose

Hemicellulose accounts for about 25 wt% of biomass in many plants. Hemicellulose and extractives are chemically similar to cellulose except that they are not polymers in that they have no consistently recurring monomer unit and they are much shorter, with a degree of polymerization (DP) between 100~200. Hemicellulose includes several

carbohydrate monomers (heteropolysacharides), mainly heterogeneously linked by six-carbon and five-carbon anhydro-sugars, with the five-carbon sugar containing about 54 wt% oxygen by mass.

The chemical structure of some major hemicelluloses (including galacto-glucomannans, arabinoglucuronoxylan, glucurono-xylans, and glucomannan) found in hard wood and soft wood appear in Figure 4 (Northey, 1998).

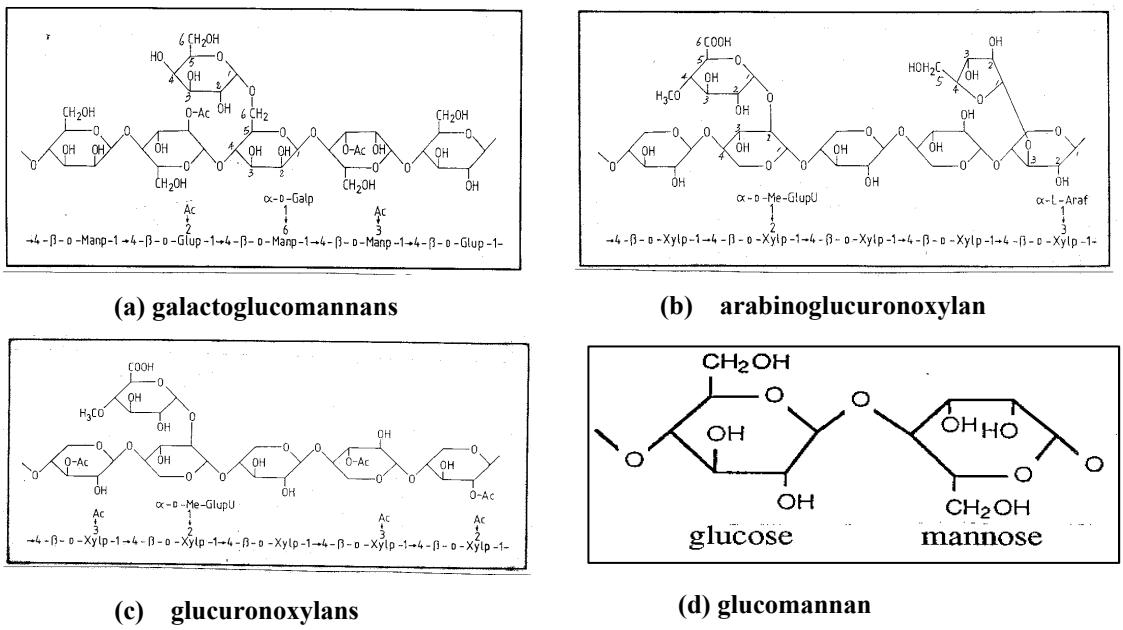

Figure 4 Chemical structures of some typical hemicelluloses (Northey, 1998)

2.1.3. Lignin

Lignin contributes about 25 wt% of biomass mass, with generally higher contents in woody material and generally lower contents in herbaceous material. Lignin is a branched, long-chain molecule similar to polymers except that it has a variety of monomer components, mostly derived from phenylpropane units and joined by

carbon-carbon and ether linkages. Lignin appears to be a primarily random, three-dimensional polymer of 4-propenyl phenol (p-coumaryl alcohol), 4-propenyl-2-methoxy phenol (guaicyl alcohol), and 4-propenyl-2, 5-dimethoxy phenol (syringl alcohol). Figure 5 (a) (Abreu et al., 1999) illustrates their chemical structures. Lignin can also be represented as coniferyl ($C_{10}H_{12}O_3$), p-coumaryl ($C_9H_6O_3$), and sinapyl ($C_{11}H_{14}O_4$) alcohols (see Figure 5 (b) (Stenius, 2000)).

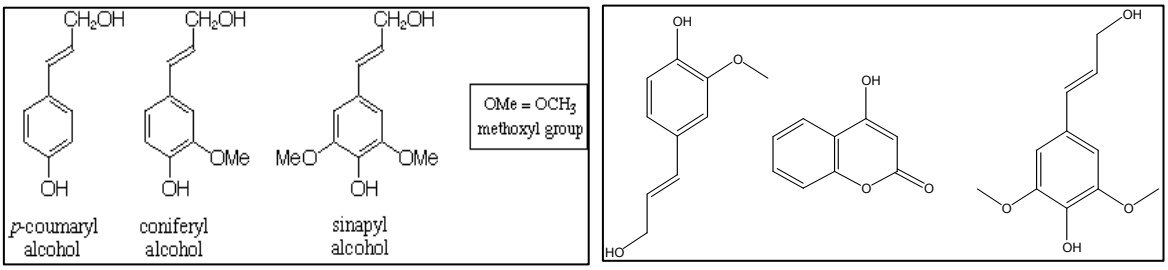

(a) structure one (Abreu et al., 1999) (b) structure two (Stenius, 2000)

Figure 5 Three compounds comprising the bulk of lignin

The ratio of these phenols in lignin is a function of the plant species and ecosystems (Stenius, 2000). Normal softwood lignins are usually referred to as “guaiacyl lignins” because the structural elements are derived principally form trans-coniferyl alcohol (more than 90%), with the remainder consisting mainly of trans-p-coumaryl alcohol. In contrast, hardwood lignins, generally termed “guaiacyl-syringyl lignins”, are mainly composed of trans-coniferyl alcohol and trans-sinapyl alcohol-type units in varying ratios (about 50% of trans-coniferyl alcohol and about 50% of trans-sinapyl alcohol). The major linkage in lignin, the arylglycerol-β-aryl ether substructure, comprises about half of the total inter-unit linkages. The oxygen content of these lignin model compounds ranges between

12-29 wt%, much lower than cellulose or hemicellulose. One chemical structure model of softwood lignin is proposed in Figure 6.

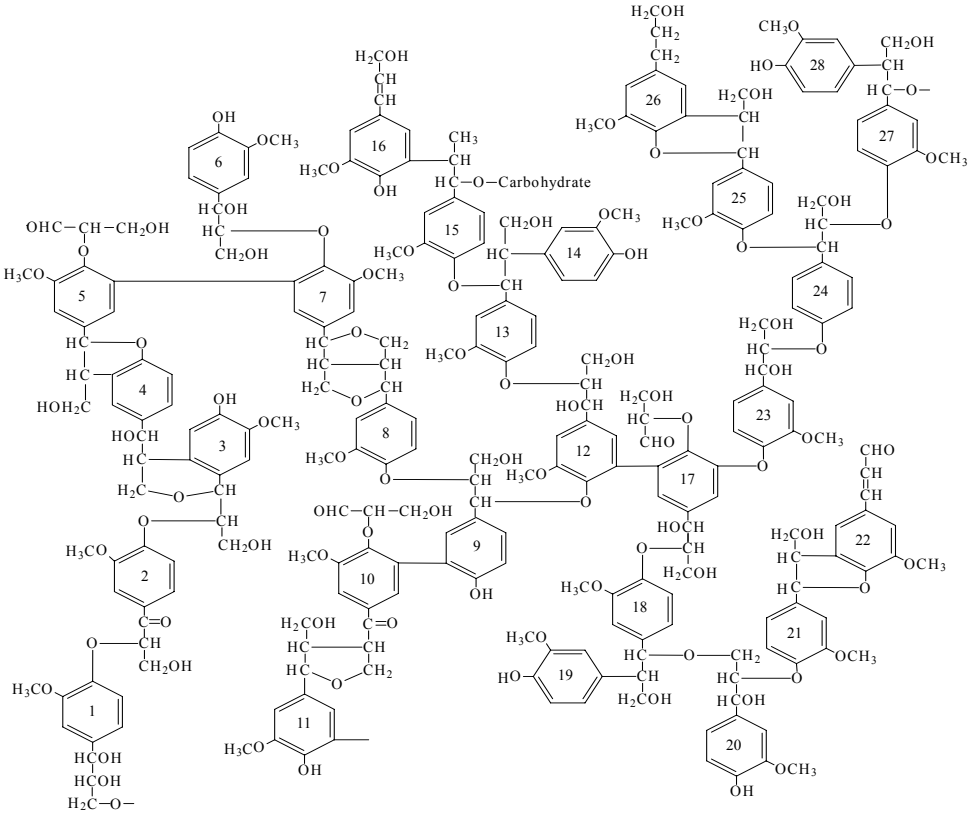

Figure 6 A model of chemical structure of softwood lignin (Northey, 1998)

2.2. Mechanism and Kinetics of Biomass Pyrolysis

Currently, the exact pyrolysis mechanisms of biomass are not clear, although substantial literature sources on biomass devolatilization kinetics and mechanisms are available. Cellulose thermal decomposition models, together with phase changes and tar production, provide a framework from which a lot of investigators have developed mathematical descriptions of biomass devolatilization.

In general, kinetic models of biomass pyrolysis process can be grouped into three main categories:

- One-step reaction, successive reactions, or two-stage models;
- Chemical structure-based models;
- Superposition models, which are based on the kinetics of individual component (cellulose, hemicellulose and lignin) of biomass.

2.2.1. One-step Reaction, Successive Reactions or Two-stage Model

Some simple models of cellulose devolatilization appear in the literature. Broido and Nelson suggested a competitive reaction model for large cellulose samples (see Figure 7 (a) (Broido and Nelson, 1975)), followed by a multi-step model (see Figure 7 (b) (Broido, 1976)) reported by Broido; and a third multi-step model by Bradbury, Sakai, and Shafizadeh (Bradbury et al., 1979) (see Figure 7 (c)). All of these models were usually used to describe low- or medium-temperature and low-heating-rate pyrolysis conditions. They are not applicable for simulating biomass conversion because they assume a constant ratio of the char to volatiles yield and cannot be extended to systems different from the one on which they were based.

Two-stage models (Di Blasi, 1996a) can be profitably applied to simulate thermal conversion since they include the description of the primary degradation of solid and the secondary degradation of primary pyrolysis products. A typical wood pyrolysis two-stage model appears in Figure 8. The tar reactions (K_4 and K_5 in Figure 8) will only be discussed as they occur in the particle interior, since any exteior reactions generally become part of the overall furnace calculation.

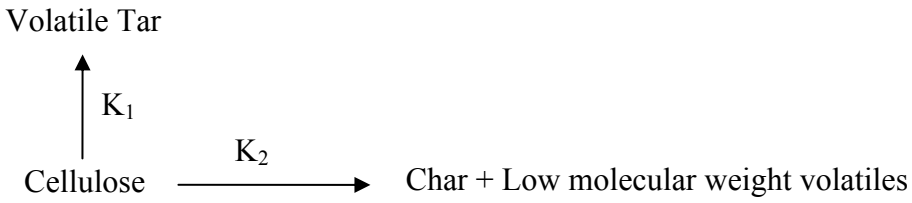

(a) Broido and Nelson model (Broido and Nelson, 1975)

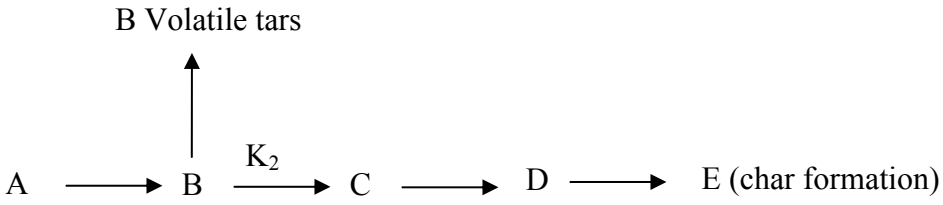

(b) Broido multi-step model (Broido, 1976)

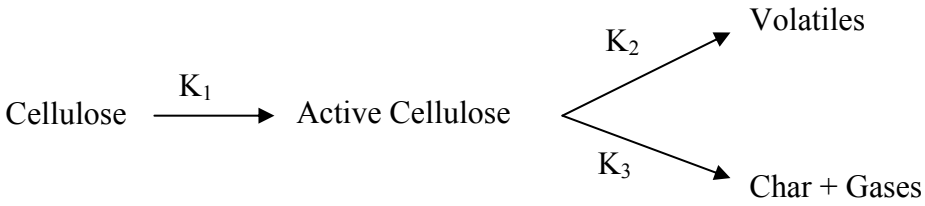

(c) Bradbury multi-step model (Bradbury et al., 1979)

Figure 7 Some basic cellulose pyrolysis models

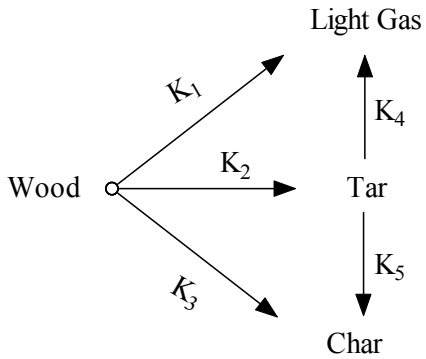

Figure 8 Two-stage wood pyrolysis model
(Di Blasi, 1996a)

A similar mechanism considering secondary reactions was used by Jalan and Srivastava (Jalan and Srivastava, 1999). The model appears in Figure 9 and accounts for the secondary reaction between the volatile, gas, and char.

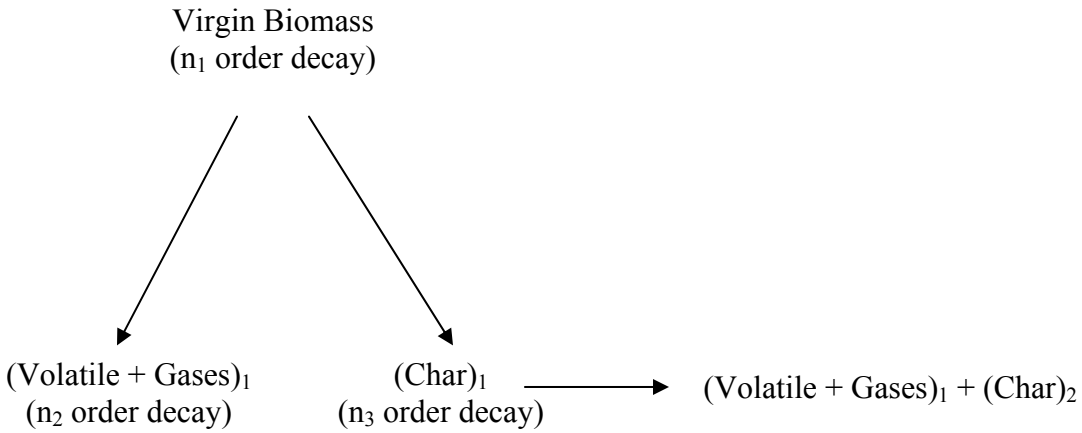

Figure 9 Srivastava pyrolysis model
(Jalan and Srivastava, 1999)

In these models, k_i is the reaction rate constant, which can be expressed as the Arrhenius formula: $k = A*exp(-E/RT)$. A is the pre-exponential factor; E is the apparent activation energy; R is the universal gas constant and T is the temperature. All reactions are assumed to be first-order. With a few modifications, these models have been widely used to predict the pyrolysis characteristics of biomass and its components.

2.2.2. Chemical Structure Model

In recent years, chemical structures have played more significant roles in the description of thermal decomposition of fuels, especially for coal combustion. Three recent models, Functional-Group-Depolymerization Vaporization Cross-linking Model (FG-DVC), FLASHCHAIN, and Chemical Percolation Devolatilization (CPD) (Fletcher

et al., 1992; Fletcher et al., 2003) have been developed with parameters defined at least in part by chemical composition of the fuel. The fuel chemical structures can be characterized by NMR, FTIR or standardized (typically ASTM) procedures. As a group, these models illustrate how the chemical forms of fuel influence its thermal decomposition. They can also predict the amount of tar formation and cross-linking, the latter representing condensed-phase reactions that lead to the formation of a relatively non-reactive char.

With some modification of the FG-DVC coal devolatilization model, Chen and Charpenay (Chen et al., 1998) applied it to model biomass pyrolysis kinetics. Biomass chemical structure data were collected from ultimate, proximate and TG-FTIR analyses. This model was demonstrated to have predictive capacity when extrapolated to modestly high heating rate conditions (10^3 K/sec). The predicted overall weight loss and CO_2 yields agree very well with experimental data, but not for other species. The observed discrepancies could result from the secondary reactions and/or catalytic role of inorganic material, so improvements are needed to properly account for effects of inorganic material and secondary reactions.

Niksa (Niksa, 2000) investigated the rapid devolatilization of diverse forms of biomass with a bio-FLASHCHAIN model. Given the proximate and ultimate analyses and thermal history and pressure, the model reportedly predicts the complete primary product distribution, though this claim seems exaggerated given the significant influence of inorganic material on yields and rates (discussed later) which is not among the input parameters.

2.2.3. Superposition Model

More sophisticated approaches to describe biomass devolatilization kinetics involve superposition of the behavior of typical biomass components such as lignin, cellulose, and hemicellulose (Koufopanos et al., 1989; Koufopanos et al., 1991; Miller and Bellan, 1997; Orfao et al., 1999; Raveendran et al., 1996). In these models, biomass components in the mixture behave in the same way as they do separately or with weak interactions. In Miller and Bellan's (Miller and Bellan, 1997) work, the pyrolysis of general biomass materials was modeled via a superposition of cellulose, hemicellulose and lignin kinetics. All three of the primary biomass components are modeled with multi-step kinetics involving both competitive primary pyrolysis and secondary tar decomposition reactions. Their model results agree well with micro-particle data, but discrepancy exists for macro-particles, as illustrated in Figure 10. This spherical particle model results suggest that particle shape (geometry) plays an important role during biomass thermal decomposition.

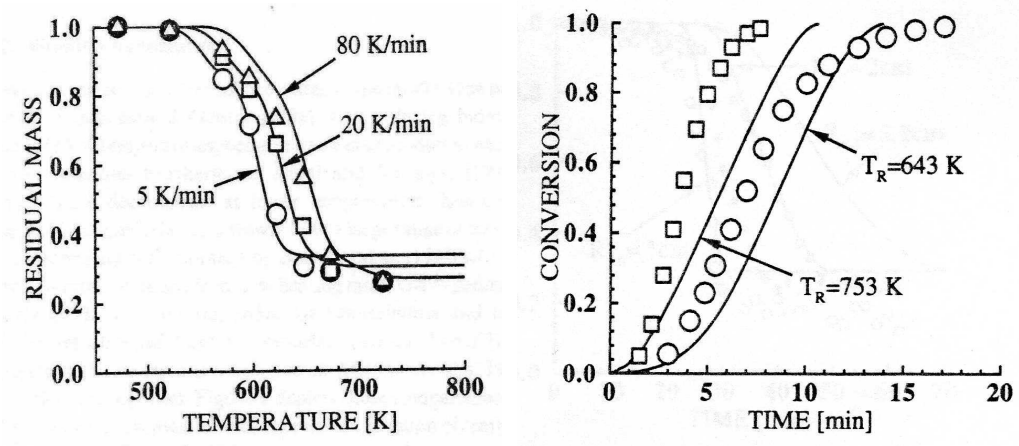

(a) Micro-particle (b) Macro-particle

Figure 10 Comparisons of superposition model predictions with experimental data for micro-particle and macro-particle
(Miller and Bellan, 1997)

Based on the chemical structure of each biomass component, Demirbas (Demirbas, 2000) proposed individual pyrolysis mechanism for cellulose, hemicellulose and lignin. In his cellulose mechanism scheme, the kinetics of the reaction proceeds through three distinct stages of pyrolysis. In the first stage, a rapid decomposition takes place with a weight loss that increases with rising temperature. In the second stage, decomposition and volatilization occur. Finally, hemicellulose reacts more readily than cellulose during heating, and undergoes rapid thermal decomposition. Lignin decomposition includes cleavage of aliphatic C-O bonds, aromatic C-O bonds and side-chain C-C bonds. All these mechanism are limited to low-temperature pyrolysis processes.

This superposition model is an appealing approach since cellulose thermal decomposition has been widely studied and satisfying data are available, and the composition (the weight fraction of cellulose, hemicellulose, and lignin) of biomass can be estimated based on ultimate and proximate analysis and heating value.

2.3. Factors Affecting Biomass Pyrolysis

Generally speaking, biomass pyrolysis characteristics are influenced by the chemical and physical properties (composition, inorganic content, density, thermal conductivity, heat capacity, particle size and shape) of biomass, as well as operating conditions such as temperature, pressure, and heating rate.

2.3.1. Composition

Pyrolysis yields and product distributions are mainly determined by the composition of the original biomass. Usually cellulose has the lowest char yield; lignin produces highest char yield; hemicellulose has a medium char yield, as shown in Figure 11 (Miller

and Bellan, 1997). The tar yield is associated with that of char, exhibiting the opposite trends.

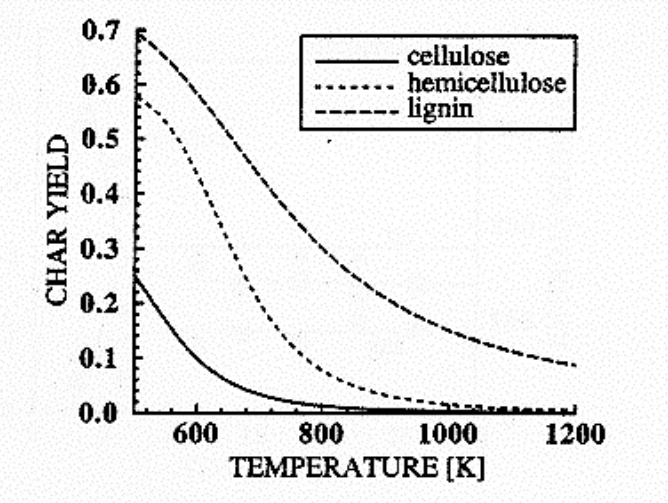

Figure 11 Char yield as functions of temperature for primary biomass components (Miller and Bellan, 1997)

2.3.2. Physical Properties, Temperature and Heating Rate

Di Blasi (Di Blasi, 1997) investigated the influences of physical properties on biomass devolatilization. A detailed particle energy and mass transport model was used to predict the effects of density, thermal conductivity, and permeability to gas flow and specific heat capacity. For conversion in a thermally thick regime (intra-particle heat transfer control), it was found that variations in the physical properties mainly affect the reactivities of secondary reactions of tar vapors and the conversion time. The highest sensitivity is associated with the biomass density and the char thermal conductivity.

Miller and Bellan (Miller and Bellan, 1996) performed a parametric investigation using a spherically symmetric particle pyrolysis model. The effects of reactor temperature, heating rate, porosity, initial particle size and initial temperature on char yields and

conversion times were illustrated. The largest effect of the heating rate was observed in the variation of the conversion times for both cellulose and wood. An increase in heating rate decreased both the char yield and the conversion time. Additionally, both char yield and conversion time are increasing functions of initial particle size, as shown in Figure 12 (Miller and Bellan, 1996), where conversion time refers to time to reach 90% (daf) conversion. The char yield increase is due to the secondary reactions between tar vapor and solid in the particle and the lower temperature heatup.

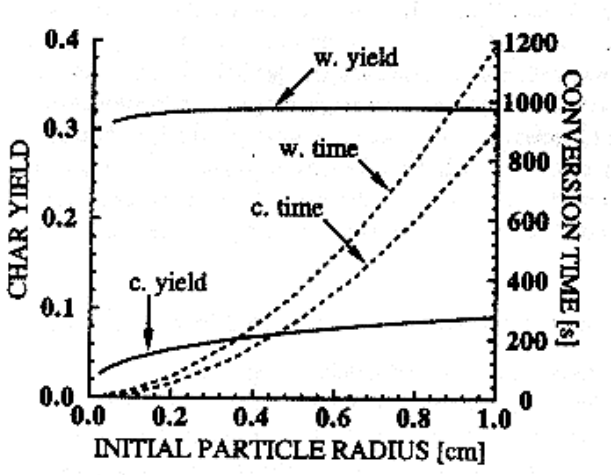

Figure 12 Char yield and conversion time of cellulose and wood vs. initial particle size
(Miller and Bellan, 1996) (w --- wood, c – cellulose)

Baxter and Robinson (Baxter and Robinson, 2000) applied engineering models of kinetics, heat transfer, and mass transfer to predict the effects of particle size and density, shape, internal temperature gradients, and composition. The results of mass loss history of biomass particles were compared with data collected from several highly instrumented furnaces. Drying and devolatilization were found to be primarily heat-transfer controlled whereas oxidation was found to be primarily mass-transfer controlled for most biomass

of practical concern. In their later research, they found devolatilization removes most of the mass. Under rapid, high-temperature pyrolysis conditions, up to 95 wt% (daf) of the mass is released during devolatilization, significantly more than ASTM tests.

The effects of particle size, reactor heating rate, and final reactor temperature were theoretically and experimentally investigated by Di Blasi (Di Blasi, 1996b). Similar results were obtained: large particle size increases char yields; higher heating rates result in higher volatile yields and lower char yields (see Figure 13, where equivalent particle diameters are indicated in units of cm). Her researech indicates three main regimes of solid-fuel pyrolysis: the thermally thick (diameter = 0.625 cm), the thermally thin(diameter = 0.04 cm), and the pure kinetic regime. The pure kinetic limit involves only particles at least one order of magnitude smaller than those allowing conversion in the thermally thin regime, except at very low temperatures.

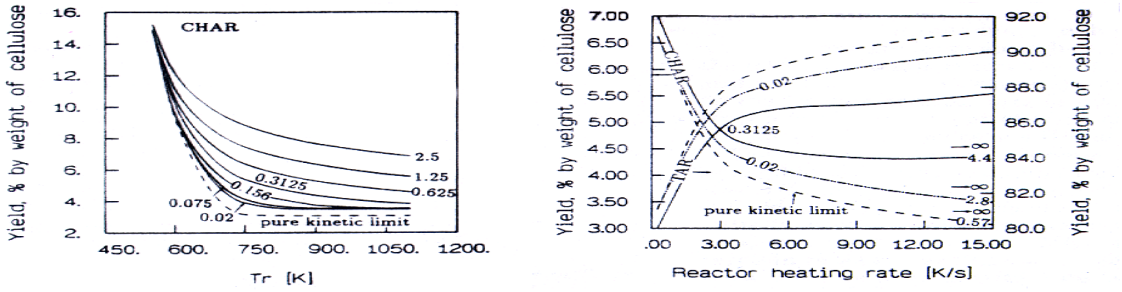

(a) Char yield vs. reactor temperature for different particle sizes

(b) Char and tar yield vs. heating rate for different particle sizes

Figure 13 Effects of particle size and heating rate on char and tar yields (Di Blasi, 1996b)

2.3.3. Particle Shape and Size

As for particle shape, a spherical particle shape is usually assumed in modeling work for convenience. Other particle shapes have been considered. Jalan and Srivastava (Jalan and Srivastava, 1999) studied pyrolysis of a single cylindrical biomass particle, and particle size and heating rate effects were investigated. In Horbaj's model (Horbaj, 1997) and Liliddahl's model (Liliedahl and Sjostrom, 1998) , a particle geometric factor was introduced to account for the particle shape, which can deal with a prism (or slab), a cylinder (or rod), and a sphere.

In 2000, Janse and Westerhout (Janse et al., 2000) simulated the flash pyrolysis of a single wood particle. To investigate the influence of particle shape, simulations have been carried out with spherical, cylindrical and flat particle shapes (see Figure 14 (Janse et al., 2000)).

Results show that spherical particles react most quickly compared to other particle shapes if the characteristic size is taken as the minium particle dimension. The higher surface-area-to-volume ratio of spherical particles on this basis explains this observation; flat particles react most slowly. In the work reported later in this document, the characteristic dimension is taken as the spherical-equivalent diameter – the diameter of a sphere with the same volume/mass as the aspherical particle. As will be shown, using the spherical-equivalent diameter results in the opposite trend – spherical particles react most slowly. There is no inconsistency in these results, just a difference in basis of comparison. At small particle diameters (typically less than 200 micron), the rate of reaction becomes dominant and the different particle shapes exhibit nearly equal conversion times. Flat particles seem to yield less gas and more char. This research also showed that an increase in particle diameter (or conversion time) caused no change in bio-oil yield, a slight

decrease in gas yield and slight increase in char yield. This might be due to the low reactor temperature (surface temperature 823 K) they used to simulate this process.

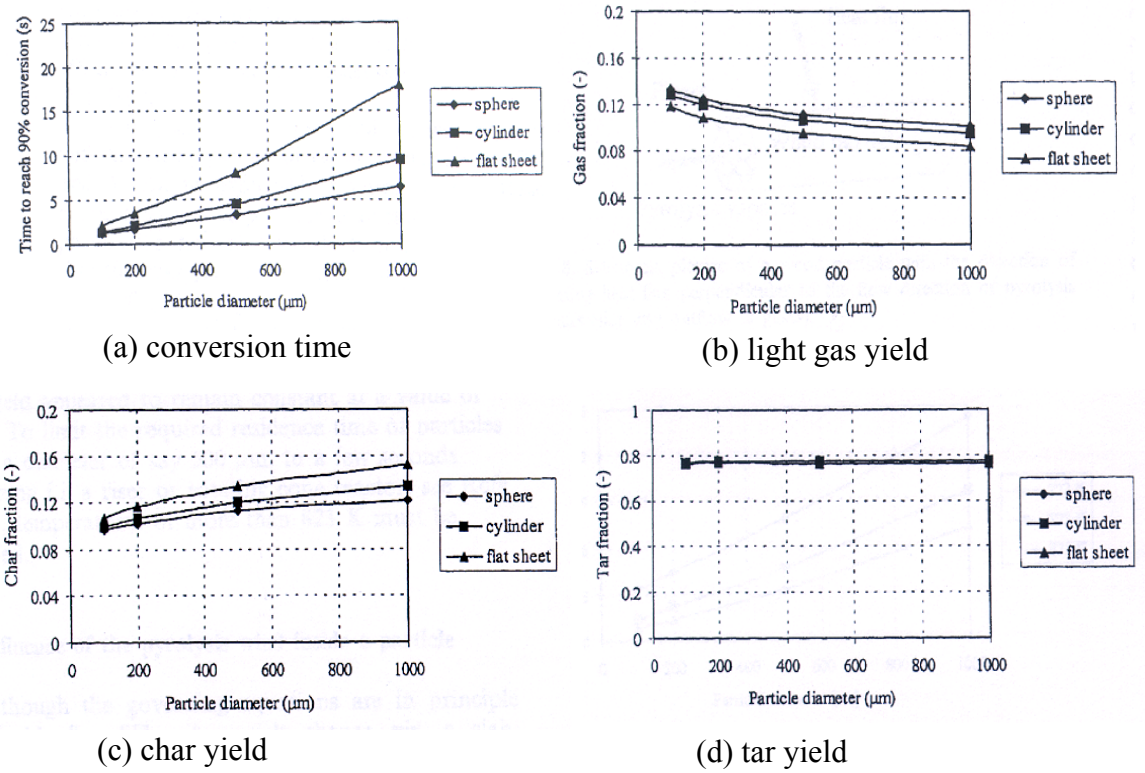

(a) conversion time (b) light gas yield

(c) char yield (d) tar yield

Figure 14 Effects of particle shape and size on conversion time and char, tar, and light gas yields during biomass pyrolysis
(Janse et al., 2000)

2.3.4. Inorganic Material

Inorganic material combined with organic components strongly influence biomass pyrolysis kinetics, total char yield, and char oxidation kinetics due to its catalytic role. Some investigators in the biomass (and coal) communities refer to such material as mineral matter. Inorganic material is a more precise term since much of the material in low-rank coals and biomass does not have mineral characteristics but is largely atomically dispersed in the organic matrix. However, this distinction is rarely recognized

in the literature and the two terms can be assumed to be synonymous in most papers. Numerous investigations have been carried out using washed and doped samples of actual fuels and pure biopolymers (e.g., cellulose, lignin, xylan), but the mechanistic details of inorganic material impacts on devolatilization remain unclear (Antal and Gabor, 1995). It is clear that removal of inorganic material, particularly compounds containing sodium and potassium, increases tar yield and decreases light gas yield. The total yields (ASTM) of char and volatiles differ among different biomass (Jensen et al., 1998; Raveendran et al., 1995), as indicated in Figure 15.

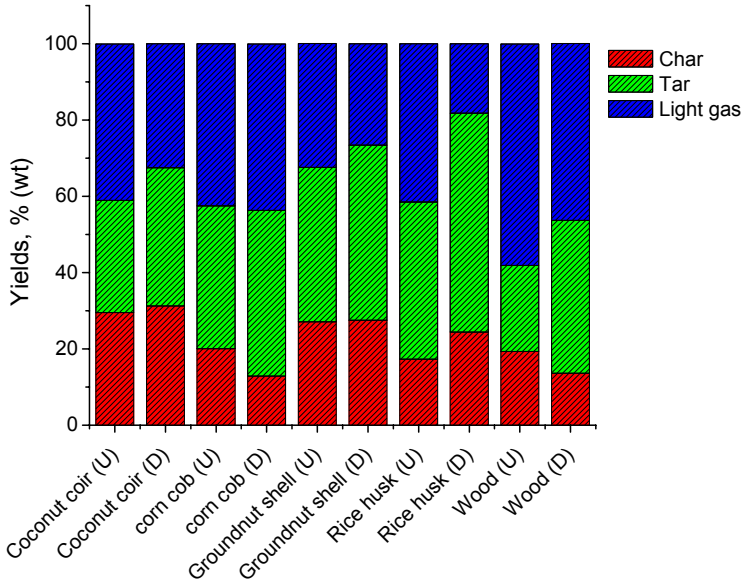

Figure 15 Influences of ash on pyrolysis products distribution (Raveendran et al., 1995), U–untreated, D–demineralizated

Williams and Horne (Williams and Horne, 1994) found that even low concentrations of metal salt significantly affect thermal degradation of cellulose and the production of residual char. Removal of inorganic material also influences the kinetics of the process.

For high-temperature and high-heating-rate conditions, little data have been obtained regarding the influence of inorganic materials on biomass pyrolysis.

2.4. Char Reactivity and Oxidation

Coal char reactivity and oxidation processes enjoy an extensive literature developed during the last decades. Char, either from coal or biomass, is usually considered to be mainly composed of carbon, containing far fewer heteroatoms (O, H, S, and N) than the fuels from which they derive but nonetheless retaining some heteroatoms and in any case having structures and reactivity very different from graphite. In this sense, the chemical structure of biomass char is similar to coal char, but large physical differences exist between them, such as density, thermal conductivity, porosity, surface area, and particle shape and size.

Mermoud and his coworkers (2006) collected experimental steam gasification reactivity data with beech char and compared with model predictions. It was demonstrated that the usual homogeneous or shrinking core particle models are not satisfying and that only the assumption of thermal equilibrium between the particle and the surrounding gas is valid for a model at bed scale.

With birch wood chars obtained from a free-fall tubular reactor and a thermobalance, Chen et al. (Chen et al., 1997) studied the char reactivity with carbon dioxide and steam in the thermobalance. It was found that the reaction rates of the char were strongly affected by the particle temperature history during char formation. Chars obtained from rapid pyrolysis possessed higher reactivity (2.3-2.4 times higher) in the reaction with carbon dioxide or steam compared with chars from slow pyrolysis. In other words,

kinetic rates of char increase with increasing particle heating rate during the thermal decomposition process.

The reactivity of two kinds of biomass chars from Southern pine and switchgrass was investigated by Wornat et al. (Wornat et al., 1999). Results showed that at early stages of char conversion, both of the chars were quite reactive. However, their reactivity decreased somewhat during char conversion as more reactive carbon is preferentially depleted and the inorganic constituents of the chars underwent physical and chemical transformations that render them less catalytically active. They also found that even with small biomass char particles (75-106 micron), the irregular morphologies and their wide range of burning rates made a more rigorous and detailed kinetic analysis quite difficulty.

Results from Di Blasi and coworkers (Di Blasi et al., 1999) indicate that in the kinetically controlled regime (low temperature ~873 K) and under non-isothermal conditions (10, 20-80 K/min heating rate), the reactivities (*dm/dt*) of three biomass chars (wheat straw, olive husks and grape residues) increased with conversion first, reaching a maximum, and decreased or remained constant then increased again as a function of conversion. A one-step global model interprets the mass loss curves in their work with conversion-dependent parameters. Again at low temperature in a TGA, Adanez and his coworkers (Adanez et al., 2001) determined combustion reactivities of five biomass chars with a combined method, with similar results.

In the chemically controlled oxidation regime, Zhang et al. (Zhang et al., 1996) concluded that the total porosity of biomass char increased from an initial value of 0.6-0.76 to a final value of 0.83-0.88; the particle shrinkage of char was the result of the

increased ordering of the graphitic microstructures in carbons with increased carbon conversion.

2.5. Summary

This chapter reviewed previous works on both biomass devolatilization and char oxidation, and discussed factors impacting biomass combustion process.

All the previously-cited investigations were conducted at low or medium temperature ranges and with a relatively small particle size. Generally speaking, during biomass char oxidation of relevance to this investigation, oxygen diffusion to a particle surface dominates the net biomass oxidation rates in practical combustion systems due to the relatively large size and rapid kinetics of biomass chars and the high temperatures of entrained-flow systems. Predictions of diffusion-limited burning of non-spherical biomass particles cannot be accurately accomplished by standard models without accounting for the geometric influences (Baxter and Robinson, 2000). Investigations including particle shape and size, and accounting for surface-area-to-volume ratios, are required to predict accurate heat transfer (and hence devolatilization) and oxidation rates of biomass particles and chars. The current investigation addresses this issue.

3. Objectives and Approach

3.1. Objectives

The objective of this project was to develop experimental and modeling descriptions of non-spherical particle/droplet combustion and to demonstrate their applicability to biomass-fired, entrained flow boilers.

This overall objective included the following experimental and theoretical components:

- Establish a comprehensive database including burning rate and thermal decomposition rate of single biomass particles with differing shapes and sizes;
- Develop a comprehensive particle combustion model, including particle drying, devolatilization, and char gasification and oxidation processes, based on the experimental data and theoretical analysis. The model also accounts for the effects of particle/droplet shape and size, reactor temperature, heating rate, and local environment (temperature, oxygen concentration, slip velocity, etc.).

3.2. Approach

The objectives of this project were met by completing the following tasks.

- Construction of an entrained-flow reactor

Build an entrained-flow reactor to generate the following data as functions of time during biomass combustion: particle surface temperature, size and shape, velocity, residence time, and mass loss. The reactor provided up to 3.0 seconds of residence time, a maximum wall temperature of 1500 K, and optical accesses for an imaging system at three positions along the reactor. *In situ* techniques generated all of these data except particle mass, which was based on particle sampling.

- Particle imaging system

Measure the particle surface temperature, particle shape, and size change during the combustion process using an imaging system built to take three images simultaneously from three orthogonal directions during heat up and combustion. This system included three CCD or complementary metal oxide semiconductor (CMOS) cameras, three image acquisition cards, and a high-performance computer. The color cameras were of high speed, high sensitivity, and at least three channels (typically red, green, and blue). The imaging system recorded videos for the complete combustion process of a single particle in a single-particle reactor, and captured images for particles traveling in the entrained-flow reactor at different residence times.

- 3-D particle shape reconstruction algorithm development

Due to irregular shapes of biomass particle, a three-dimensional particle shape reconstruction algorithm was developed and coded. By combining the three particle images taken from three orthogonal directions into a three-dimensional computer-generated particle shape, the particle surface area, volume, and shape were approximately determined. Such an algorithm led to time-resolved measurement of the surface-area-to-volume ratio and similar important particle properties.

- Color-band pyrometry development

For a particle traveling in the entrained-flow reactor or a particle undergoing shrinking/swelling during combustion, a non-contact pyrometry is preferred to measure its surface temperature. In this project, a color-band pyrometry (first-ever applied to particle combustion) was developed and applied. With images taken by the imaging system, the local particle surface temperature was calculated by the image pixel intensity ratio of any two of the three channels (red, blue, and green) by assuming gray body radiation for the particle. If the particle surface temperature is lower than the reactor wall temperature, the reflection effect on the particle surface will be considered in the calculation and thus limit the useful range of the device. The local surface temperature can also be superimposed on the 3-D particle shape model generated by the shape reconstruction algorithm, resulting in pixel-by-pixel temperature data for most of the 3D particle reconstruction.

- Data collection and analysis

With a single-particle reactor and the entrained-flow reactor system built in this project, experiments for the drying, devolatilization, and oxidation processes of biomass particles produced mass loss and temperature data, from which kinetic rate constants for both devolatilization and oxidation models can be determined. Particle mass, surface temperature, center temperature, particle surface area and volume were measured using techniques developed in this project. The data were reconciled with the model.

- Develop a comprehensive solid/droplet particle combustion model.

For the particle drying process, a mass and heat transfer coupled model were used to simulate the evaporation and recondensation of moisture in the particle. Biomass

devolatilization kinetics was described using a two-step global scheme model. Detailed particle mass and heat transfer models including kinetics, particle physical properties (including particle size and shape) and surrounding gas phase properties, were developed to describe the particle drying, devolatilization, char gasification and oxidation processes. For biomass char oxidation, this is generally a diffusion-controlled process due to the typically large particle size. In this case, a simple mass transport model, instead of a complex one, might be used. However, oxidation kinetic expressions were included in the model with some simplifying assumptions. Specifically, intrinsic, single-step surface kinetics was used. It was expected that even global kinetics would have little impact on the diffusion-limited burning rates. However, shape and size would impact such rates substantially. Based on the above three sub-models, a comprehensive particle combustion model has been developed.

4. Experimental Method

Pyrolysis and combustion experiments were conducted in a single-particle reactor and an entrained-flow reactor for wood samples of different sizes and shapes. Measurements of particle mass loss, surface temperature, internal temperature, and particle size change were performed, as described below.

4.1. Samples

Four types of biomass samples were prepared and used in this investigation. Hard wood sawdust particles with sizes ranging from 300 to 500 μm were prepared for the entrained-flow reactor since its maximum residence time is 3.0 seconds. Large poplar dowel particles with sizes ranging from 3 mm to 12 mm were used in the single-particle reactor so that the samples could be suspended using thermocouple wire; knees and stalks of wheat straw were also prepared and burned in the single-particle reactor.

4.1.1. Sawdust Particles

Sawdust particles have broad distributions both in size and shape. Three shapes were prepared in this project: near-spherical, flake-like, and cylinder-like. For each shape, samples with more than two different sizes were prepared. To obtain enough sample with uniform properties for each specific shape and size, sawdust was first separated using sieves, then aerodynamically classified. Finally, different aspect ratios were separated by

sieves again. The detailed preparation procedure appears in four steps, as illustrated in Appendix A.

With this procedure, sawdust particle samples with fairly uniform shape and size have been prepared. Two sets of samples were used to conduct pyrolysis and combustion experiments in the entrained-flow reactor. The particle volume and surface area were calculated using the 3-D particle shape reconstruction algorithm developed in this project. The particle volume and surface-area-to-volume ratio of each shape was verified by measuring over 2000 particles and assuming an average particle density of 650 kg/m^3, consistent with the literature (Koufopanos et al., 1991; Miller and Bellan, 1997). Particle shapes are pictured in Figure 16. Other particle properties appear in Table 2 and Table 3. The samples were put in an oven at 90 °C for two hours before use.

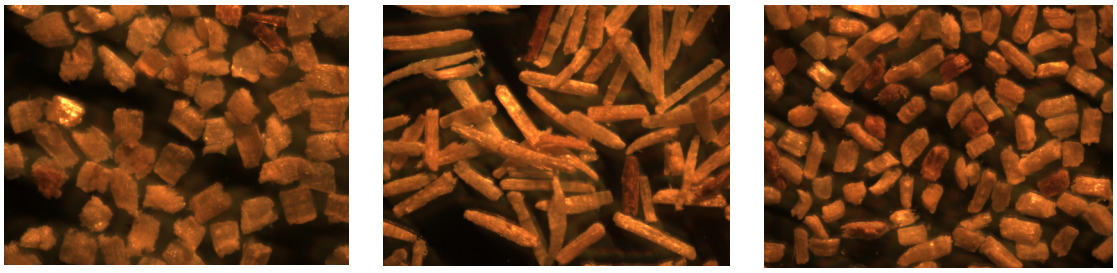

(a) flake-like particle (b) cylinder-like particle (c) near-spherical particle

Figure 16 Photographs of sawdust particles of different shapes

Table 2 Properties of sawdust sample set I

Sample	Flake-like	Cylinder-like	Equant
Volume ($\times 10^{-11}$ m^3)	1.697	1.682	1.794
Equivalent diameter (mm)	0.32	0.32	0.325
Surface area ($\times 10^{-7}$m^2)	4.91	4.79	3.44
Aspect ratio	4.0 (width/thickness)	6.0	1.65

Table 3 Properties of sawdust sample set II

Sample	Flake-like	Cylinder-like	Equant
Volume ($\times 10^{-11}$ m^3)	1.88	1.97	1.99
Equivalent diameter (mm)	0.33	0.34	0.34
Surface area ($\times 10^{-7} m^2$)	5.26	5.25	4.1
Aspect ratio	3.8 (width/thickness)	5.8	1.5

4.1.2. Wood Dowel Particles

The single-particle reactor uses larger wood particles. Three regular shapes, cylinder, disc, and near-sphere, were obtained by cutting poplar dowel rod to different aspect ratios. Particle diameters ranging from 3 mm to 12 mm. Aspect ratios (AR=length/diameter) ranging near 1.0 for spheres, 0.2 to 0.125 for discs, and 5.0 to 8.0 for cylinders. Figure 17 illustrates typical samples.

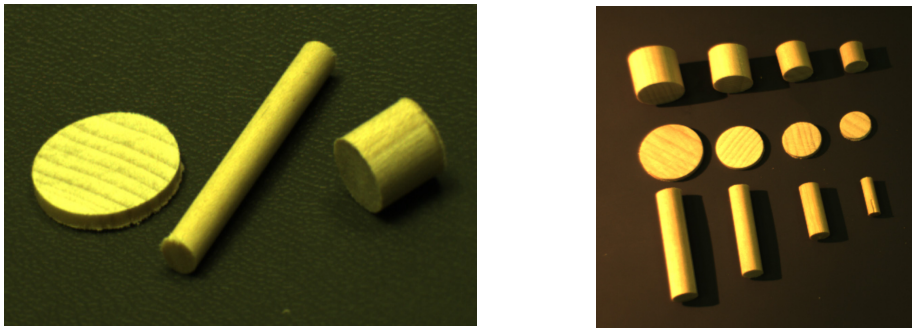

(a) Different shape (b) Different sizes

Figure 17 Poplar dowel particle samples

Two sets of poplar dowel particles were used in this investigation. Sample data are tabulated in Table 4 and Table 5. Moisture content of the samples is about 6%. To study

the drying behavior of biomass particle, samples with different moisture contents were also prepared by soaking samples in water.

Table 4 Properties of poplar dowel particle sample set I

	Diameter (inch)	AR
Near-sphere	0.25, 0.375, 0.5	1.0
Disc	0.188, 0.375, 0.75	0.125 (thickness/diameter)
Cylinder	0.125, 0.188, 0.25	8.0 (length/diameter)

Table 5 Properties of poplar dowel particle sample set II

	Diameter (inch)	AR
Near-sphere	0.125 - 0.625	1.0
Disc	0.125 – 1.0	0.2 (thickness/diameter)
Cylinder	0.125 – 0.438	5.0 (length/diameter)

4.1.3. Wheat Straw Samples

Wheat straw knees and stalks with same mass have been prepared. The particle mass is about 0.04 gm. Stalks appear to be larger than knees due to the density difference, as shown in Figure 18. The diameter of a knee is about 4 mm, and ~4 mm × ~ 12 mm for stalks.

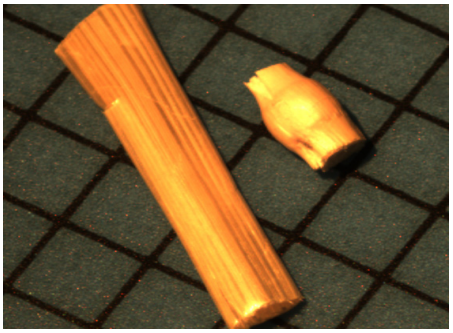

Figure 18 Wheat straw samples: knee and stalk

4.2. Experimental Setups

Devolatilization and combustion experiments used both entrained-flow and single-particle reactors, both facilities designed and built as part of this project. The entrained-flow reactor focused on small particles, and the single-particle reactor focused on large particles.

4.2.1. Entrained-flow Reactor

The process diagram of the entrained-flow reactor designed and built as part of this project appears in Figure 19. The experimental setup consists of six parts: a particle feeding system, a secondary gas preheater, an entrained-flow reactor body, a sample collection and separation system, an imaging system, and a temperature control system. Each of the above six parts is explained in detail.

In this project, two entrained-flow reactor configurations were used: a short one with only one section and no imaging system and a longer one with four sections and an imaging pyrometry.

A syringe feeder regulated biomass feed rate, with biomass particles entrained in entering the reactor through the feed probe. The preheater heats secondary gas heated to 1400 K as it flows into the top of the reactor. The reactor heats biomass samples as they

undergo drying, devolatilization, gasification, and oxidation. A water-cooled nitrogen quench probe collects char which is subsequently separated from entrainment gases by two cyclone separators in series. The distance between the feed probe and the collection probe and the entraining air flow fix particle residence time in the reactor.

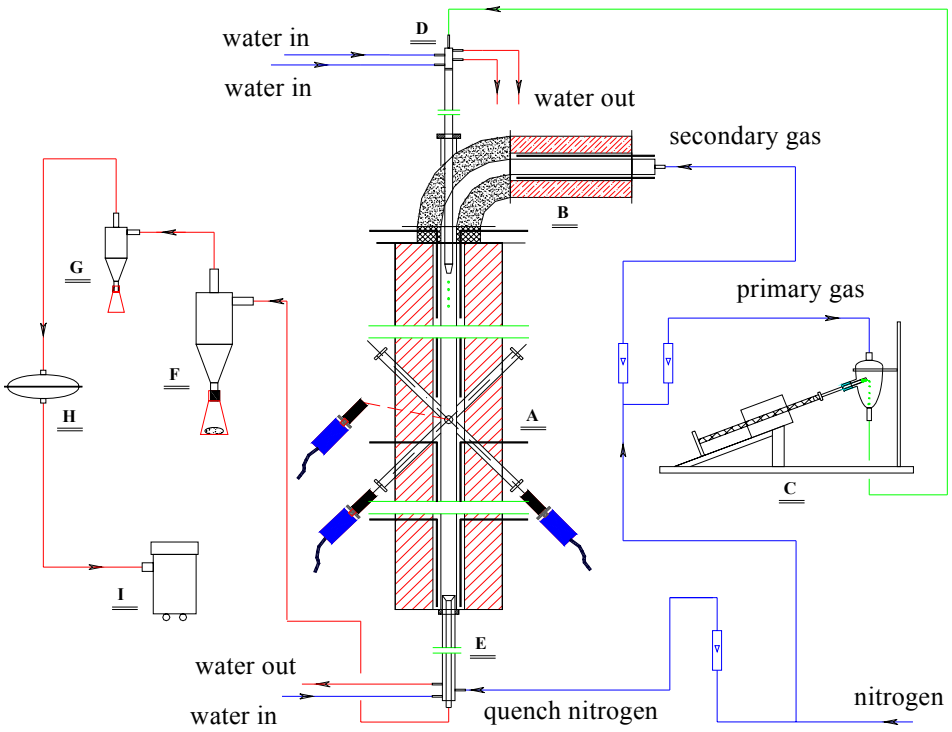

A - entrain flow reactor B - preheater C - syringe feeder D - feeding probe
E - collection probe F - 1st cyclone separator G - 2nd cyclone separator
H - filter I - vacuum

Figure 19 Process diagram of the entrained-flow reactor

Particle mass loss was determined by either weighing both the initial total mass of the feedstock samples and the collected char samples in the first cyclone separator or by an ash tracer method. The ash tracer method assumes ash is a conserved particle property

(does not vaporize or otherwise leave the particle). Under such assumptions, the total ash content indicates the mass loss as follows

$$m_0 a_0 = m a, \tag{1}$$

$$\frac{m}{m_0} = \frac{a_0}{a}, \tag{2}$$

$$1 - \frac{m}{m_0} = 1 - \frac{a_0}{a}, \tag{3}$$

where, m and a are total sample mass and ash content respectively. The subscript 0 stands for initial state. A specific single inorganic component can also be used to calculate the mass loss with the total ash contents replaced by the component contents in Equation (3).

The imaging system described below provides particle surface temperature and particle velocity.

Separate valves and choked-flow orifices control and meter primary gas, secondary gas, and quench gas flow rates according to the Equation (4) (Saaddjian et al., 1996):

$$m^* = A^* \frac{p_0}{\sqrt{T_0}} \sqrt{\left(\frac{\gamma}{R}\right)\left(\frac{2}{\gamma+1}\right)^{(\gamma+1)/(\gamma-1)}}, \tag{4}$$

where, m^* is the gas mass flow rate, A^* is the orifice cross-sectional area where Mach number is 1, p_0 and T_0 are stagnation pressure and temperature respectively, γ is gas specific heat ratio, and R is the gas constant.

A LabVIEW program records and monitors all gas flow rates and temperature distributions along the reactor and in the preheater.

- Particle feeding system

The feeding system, as shown in Figure 20, comprises a feed-rate-control motor, a syringe feeder, a vibrator, a funnel, and a water-cooled feed probe. The particle feed rate is controlled by a computer program through the control motor. The vibrator helps maintain a constant feed rate. This system reliably feeds material as slow as 1.0 gm/hr. Particle samples, carried by the primary gas, enter the reactor through the feed probe. The feed probe is 1.27 meters long, with a 3 mm inner diameter and 25 mm outer diameter. Two water jackets control the probe and sample temperatures before they enter the reactor. The detailed structure of the feed probe appears in Figure 21. Figure 22 shows the assembly of the feed probe.

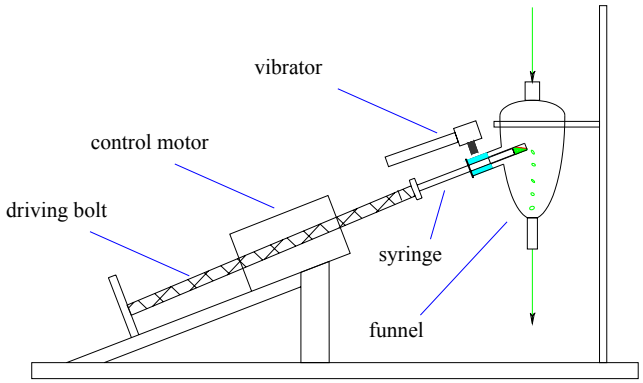

Figure 20 The biomass syringe feeding system for the entrained-flow reactor

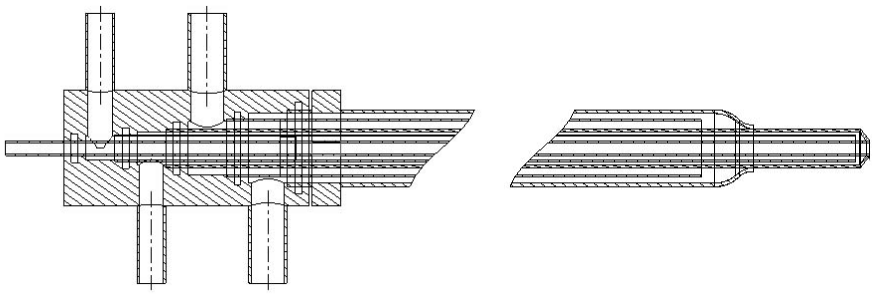

Figure 21 Feed probe structure design drawing

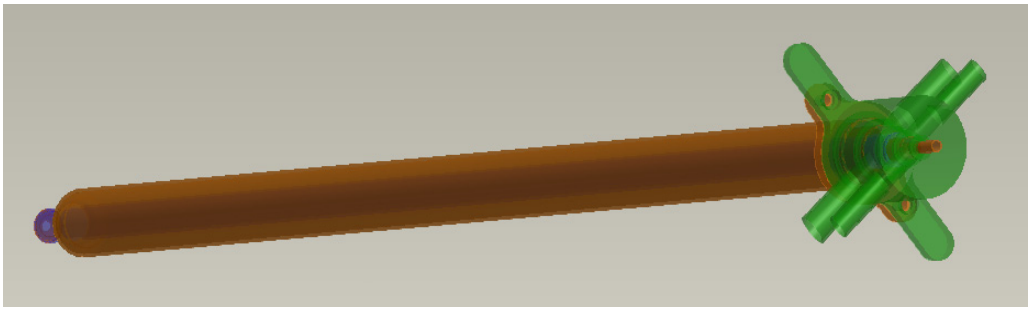

Figure 22 Assembly of the feed probe

- Preheater

A preheater controls the secondary gas temperature, typically comparable to the reactor temperature. The preheater uses a Globar heating rod installed in the center, which heats the crushed ceramics packed in the gap between the recrystallized silicon carbide tube and the refractory cast in the steel cylinder. The crushed ceramics heat secondary gas as it flows through. Specifications of the preheater appear in Table 6. The structure appears in Figure 23 in detail. The preheater wall can be heated to 1400 K. A Silicon Controlled Rectifier (SCR) coupled with a temperature controller maintains temperature setpoints.

Table 6 Preheater specifications

Diameter (inch)	12.7
Length (inch)	32
Heating element	Globar SiC SGR
Inner tube material	Re-crystallized SiC Halsic-R

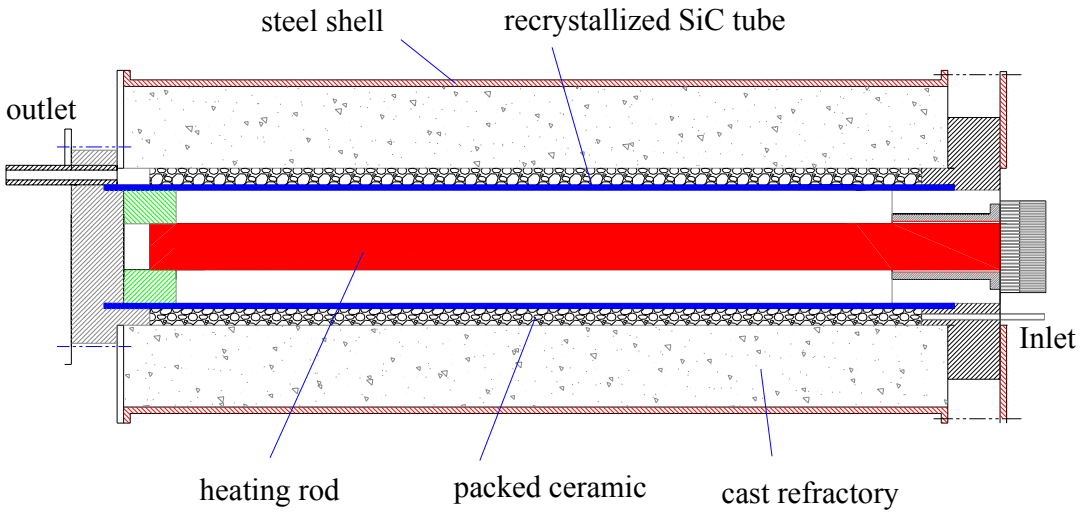

Figure 23 Schematic diagram of the preheater for the entrained-flow reactor

- Entrained-flow reactor

Recrystallized SiC tubes of 60 mm OD and 50 mm ID line the reactor main body. The reactor is 1.8 m long, providing a residence time of up to 3 seconds. The reactor insulation includes one layer of alumina fiber board and two layers of high-temperature blankets. Molybdenum disilicide Kanthal Super heating elements placed between the reactor tube and the inner alumina fiber board control the reactor temperature. The design calls for a maximum outer surface temperature of 50 ^{o}C. The entrained-flow reactor can reach wall temperatures up to 1600 K and a particle heating rate of 10^{3}~10^{4} K/s. The temperature profile along the reactor is controlled separately by adjusting wall temperatures in each of four sections of the reactor with SCR temperature controllers.

Windows at three levels along the reactor body provide optical access, allowing three orthogonal measurements of particle surface temperature and particle shape with CCD/CMOS cameras. These windows divide the reactor into four sections. Each of the windows provides optical access for image acquisition from three orthogonal directions,

as shown in Figure 24. Quartz window glass seals the outside end of each view port. Supported by a SiC plate, each window section includes six view tubes and a short collar tube.

Figure 24 Window section with optical accesses in three orthogonal directions - the insulation was not been placed yet

A detailed structural photo of the reactor body appears in Figure 25. In each of the four sections of the reactor, four U-shaped heating elements hang over refractory bricks immediately adjacent the recrystallized SiC reactor tube, with about 20 mm separation. Four pieces of short reactor tubes reduce thermal expansion stresses compared to a single piece, and these are pinned together through three collar tubes.

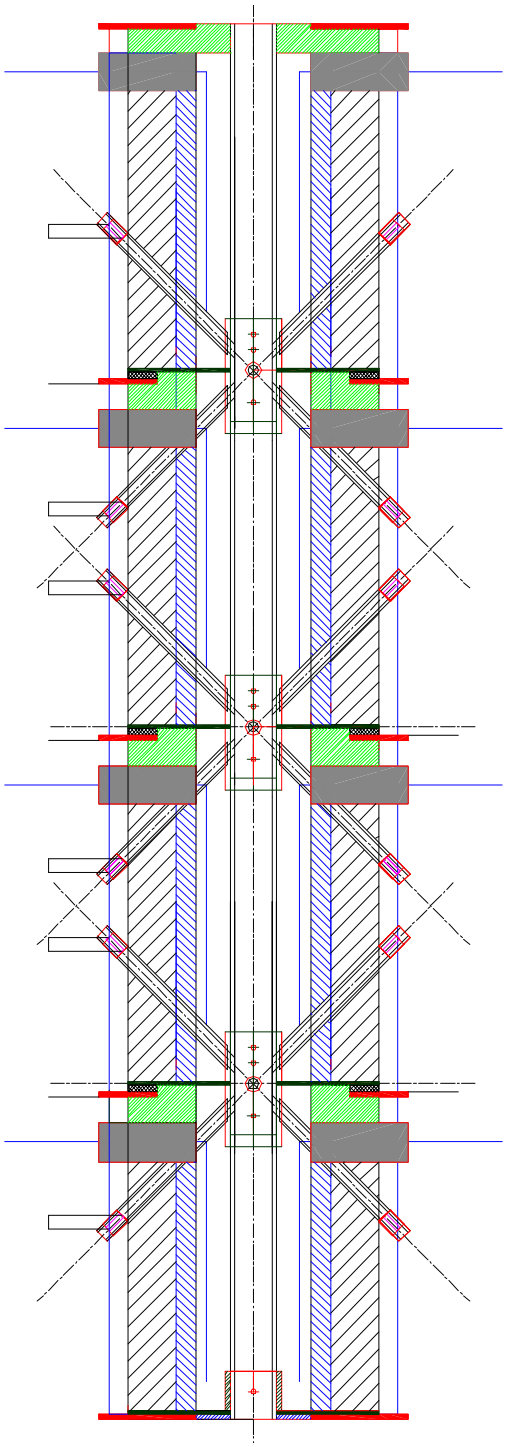

Figure 25 Schematic diagram of the entrained-flow reactor main body

Four steel plates support the reactor body. The plates are located below the four SiC plates and welded to four metal uprights. The base of the four uprights is bolted into the

floor and the tops are secured by four cables. Figure 26 illustrates the assembly of the entrained-flow reactor body supported by the four uprights.

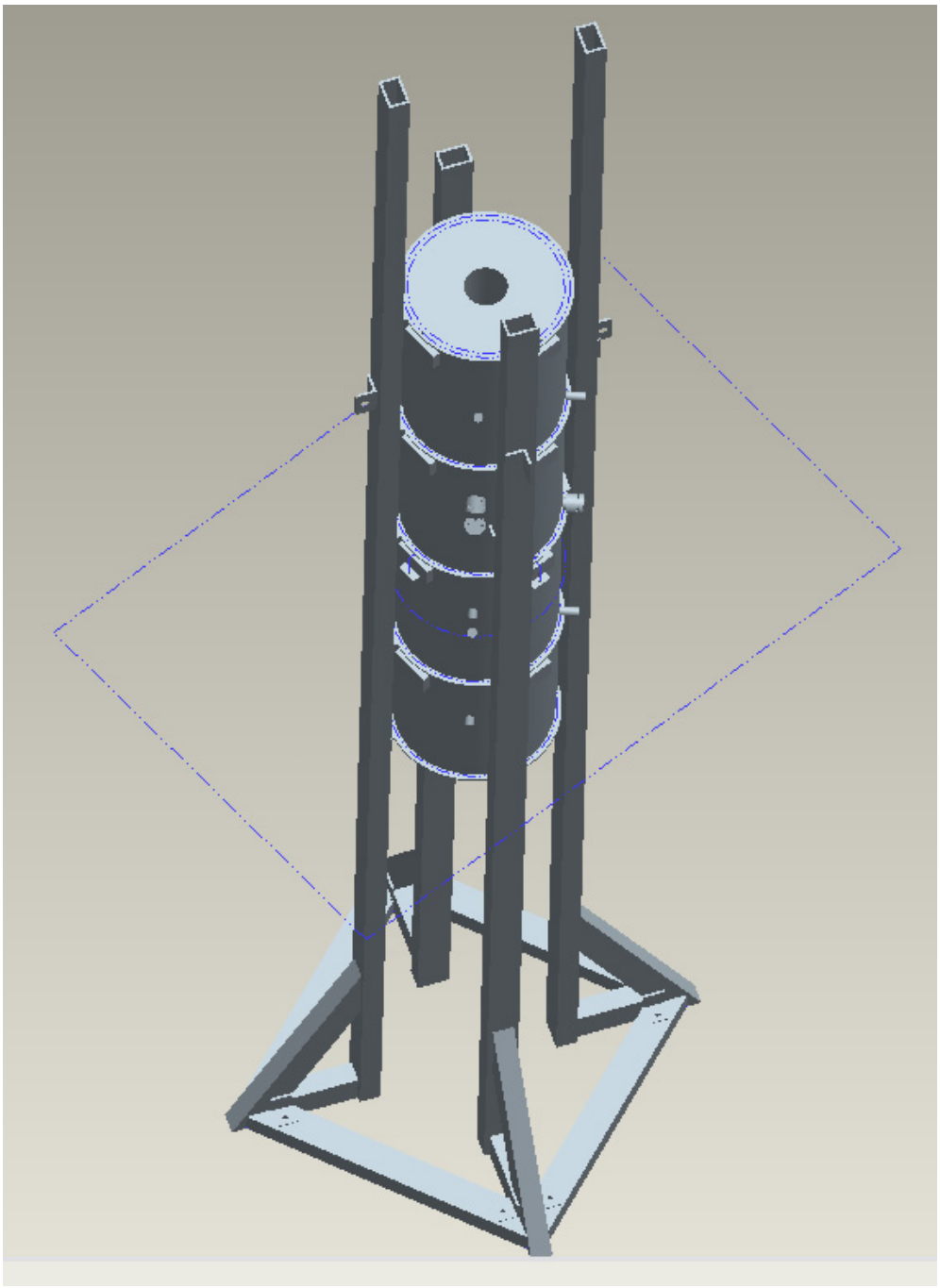

Figure 26 Assembly of the entrained-flow reactor

Specifications of the entrained-flow reactor are listed in Table 7.

Table 7 Entrained-flow reactor specifications

Height (m)	1.8
Outer diameter (m)	0.4
Inner diameter (mm)	50
First layer insulation	Rescor 3360UHT
Secondary layer insulation	Rescor 3370UHT
Third layer insulation	Rescor 370
Heating elements	2-shank Kanthal Super ST and N 6/12 mm
View tube material & size	Re-crystallized SiC Type Halsic-R
Reactor tube material & size	
Collar tube material & size	
Supporting plate material & size	

- Sample collection and separation system

The particle collection system includes a water-cooled collection probe, two cyclone separators in sequence, and a filter assembly. A Venturi vacuum pump drives flow through this system. The hot gas and particles enter the collection probe, quenched by nitrogen gas or air introduced through the end of the collection probe. The volume flow rate ratio of the quench gas to the hot gas is about 7:1. A water-bath heat exchanger appears between the filter and Venturi vacuum to cool the exhaust gas.

A detailed structure of the collection probe appears in Figure 27 and its assembly appears in Figure 28.

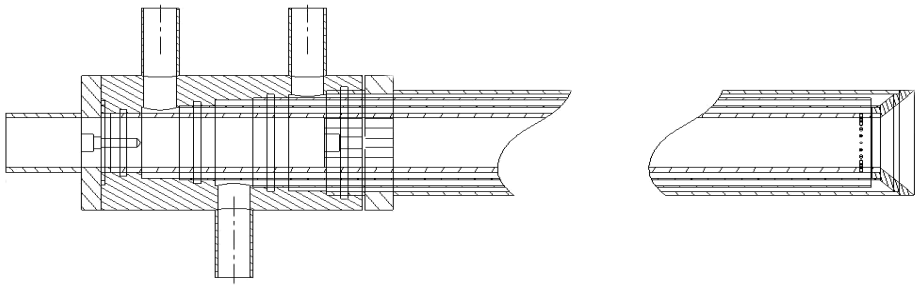

Figure 27 Collection probe structure design drawing

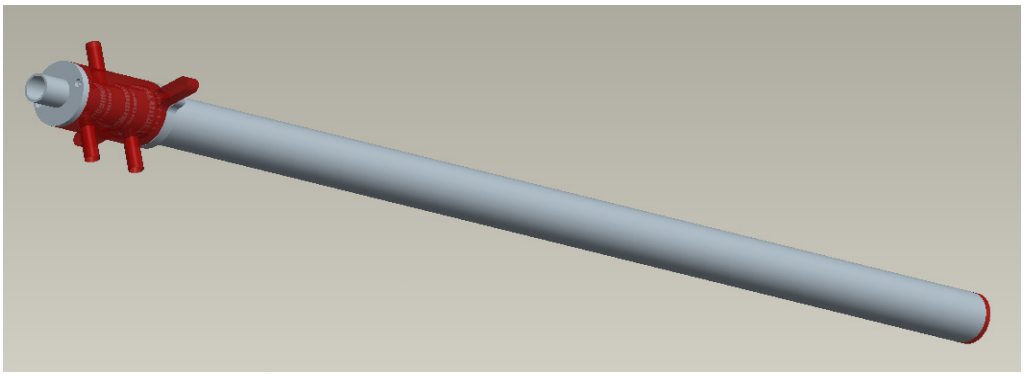

Figure 28 Assembly of the collection probe

The cyclone separators have design cut points of 20 μm and 5μm, respectively. The filter pore size is 1μm. With sawdust samples sized from 300 μm to 500 μm, most of the char samples appear in the first cyclone separator (99 %). Soot and condensed tar sometimes appear on the filter membrane. The cyclone separator drawing appears in Figure 29 (only the 20 μm cut point one), and Figure 30 shows the assembly.

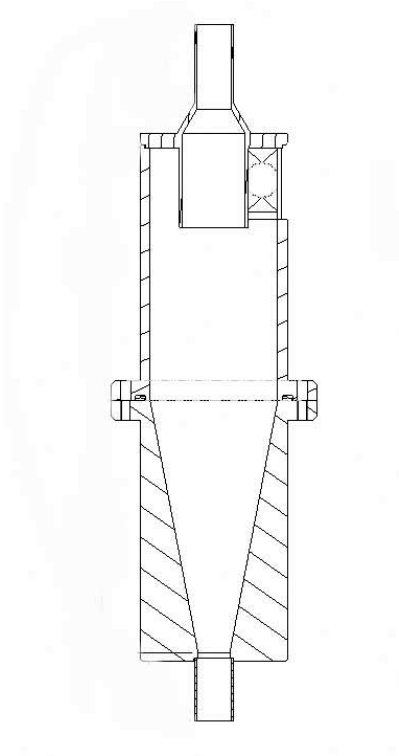

Figure 29 Cyclone separator structure design drawing

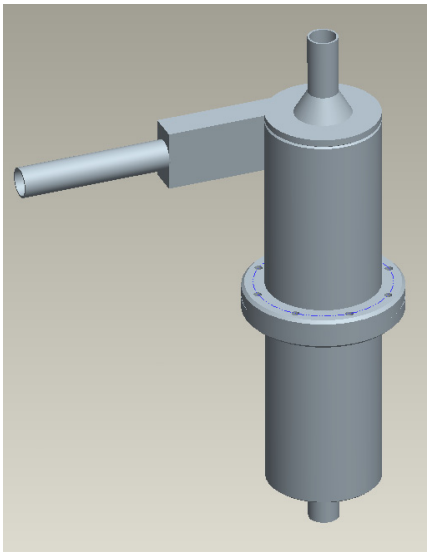

Figure 30 Assembly of the cyclone separator

- Imaging system

The imaging system includes three cameras, three image acquisition boards, cameral control and image processing software, and a high-performance computer. When taking videos or images, the three cameras image along three mutually orthogonal directions. The imaging system can record up to two-minute videos with full resolution (1036x1024), and longer record time can be obtained at reduced resolution. The camera uses a SONY ICX285AQ CCD sensor with microlenses, which is more sensitive in the near infrared (NIR) range than traditional CCD sensor. The electrical shutter speed is as short as 62 μs. Detailed components specifications of the imaging system appear in Table 8.

Table 8 Components and specifications of the imaging system

Camera	SVS-285CSL, 10 bit, shutter speed, frame rate
CCD sensor	Sony ICX285AQ, Cell size 6.45x6.45 μm, Resolution 1036x1024
Lens model	Computar MLH-10X
Image acquisition board	Epix Inc. PIXCI D2X
Camera control software	XCAP2.0
Computer configuration	XEON CPU 3.06 G Hz, 3.5G RAM

The three cameras are pre-focused on the center of reactor through the window section, which is the cross-point of the three optical paths. The recorded videos undergo shape reconstruction analysis (explained later) and temperature analysis (also explained later) to yield a three-dimensional shape and surface temperature computer image.

- Temperature control system

The reactor wall temperatures in each of four sections behave independently. Each section has 4 U-shaped 90^{o}-bent Kanthal Super heating elements and the power output can be adjusted by the transformer and SCR controllers to regulate temperature. Two three-phase SCR controllers and two three-phase transformers control the 12 heating elements in the top three sections of the reactor according to the setpoints using three fuzzy logic controllers. Each of the 6 heating elements is star-connected with the three-phase transformer. The bottom section is controlled by a single-phase SCR controller a single-phase tranformer and an additional fuzzy logic controller with the 4 heating elements connected in series. Specifications of each component of the temperature control system are listed in Table 9.

Table 9 Components and specifications of the temperature control system

Temperature controller	FuzyPro 1/16 DIN
SCR controller	Halmar Electronics Inc., 3P-4860-CL-D Single phase: AVATAR B2P -24-60, SCR71Z-230
Transformer	Matra Electric Inc. Model 90165346K, 480-70Y/40.4 Single phase: Olsun Electrics Corp. H-115 208-50/60

4.2.2. Single-particle Reactor

A single-particle reactor with the same optical access features as the entrained-flow reactor, designed and built by Ip (Ip, 2005), was used to conduct biomass particle devolatilization and combustion experiments on particles whose conversion/residence times exceed those of the entrained-flow reactor. The detailed structure explanation of the reactor can be found in Ip's thesis (Ip, 2005).

Figure 31 schematically illustrates the experimental reactor for the single-particle combustion investigations. Single biomass particles of various shapes (equant, disc, and cylinder) and diameters (3 - 12 mm) suspended on type-B thermocouples provide simultaneous size, shape, internal temperature, external temperature, and mass loss data. A wireless data logger, from PACE Scientific (Model XR440), records internal/center temperature data from the thermocouple at 20 Hz. The data logger, thermocouple, and biomass particle rest on top of a balance (Model SCIENTECH SA310IW). A small hole about the size of the thermocouple wire (~0.01 inch) through the center the particle provides access for the bead at the particle center. The balance records mass loss data at a resolution of 0.1 mg and an accuracy of $\pm$0.2 mg. The imaging system and optical pyrometer focus on the surface and record physical changes in shape/size and surface temperature data. An experiment begins with the balance, data logger and biomass sample entering the reactor. The data logger, the balance, and the imaging system begin recording data simultaneously, synchronized within 0.1 second. During devolatilization, a second thermocouple pressed against the particle surface records particle surface temperature in addition to the imaging system measurements. To reduce the influence of thermal conduction on surface temperature measurement, a shallow and narrow groove in the particle surface housed the wire.

This single-particle reactor provides time-resolved, simultaneous mass loss, surface and internal temperatures, size, and shape data during pyrolysis and combustion processes.

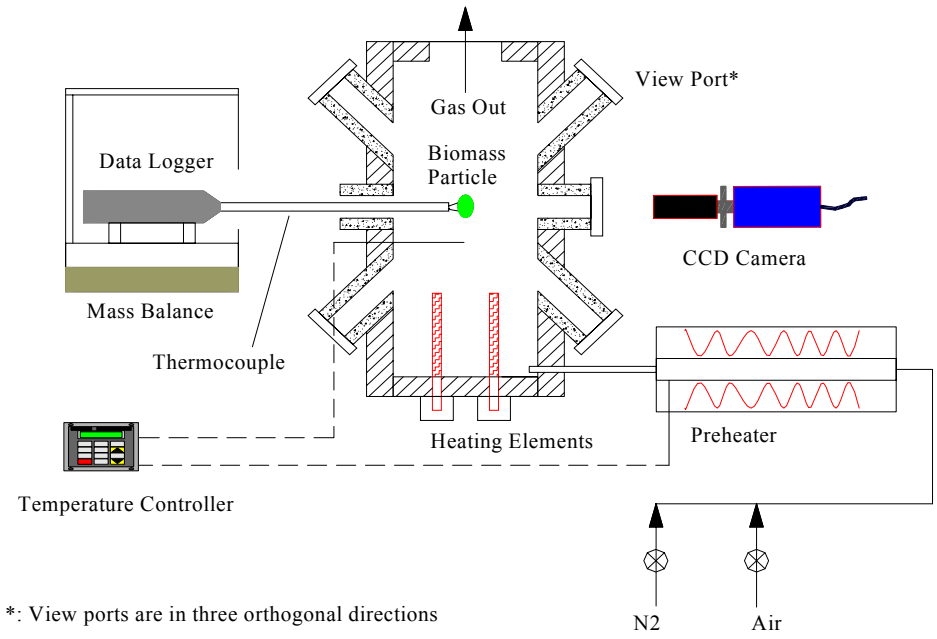

Figure 31 Schematic diagram of the single-particle reactor

4.3. Color-Band Pyrometry Development

Non-contact surface temperature measurements provide significant advantages for particles traveling in the entrained-flow reactor or particle undergoing shrinking/swelling or surrounded by flames or other reacting gases in the single-particle reactor. Traditionally, two-color pyrometry provides such data. The disadvantages of this traditional technique include a complicated, expensive, and sensitive imaging system including Photo Multiplier Tubes (PMT) and notch filters, a lack of particle shape information, relatively low signal strengths, crude estimates of size, and no spatial resolution of temperature data. This project developed and applied a conceptually similar but simpler technique that addresses all of these issues. This is the first-ever application of this technique to particle combustion. The technique, named multi-color band pyrometry, appears in detail below.

4.3.1. Color-band Pyrometry Principles

Black body spectral radiance (Ingle Jr. and Crouch, 1988), expressed as $B_\lambda^b = C_1\lambda^{-5}/\left(e^{C_2/\lambda T} - 1\right)$, forms the basis of Planck's law. For a gray body: $B_\lambda = \varepsilon_\lambda B_\lambda^b$, where $\varepsilon(\lambda)$ is the spectral emissivity. The total radiance is $B = \int_0^\infty B_\lambda d\lambda$. In the wavelength range between λ_1 and λ_2, the total radiance is $B = \int_{\lambda_1}^{\lambda_2} B_\lambda d\lambda$. For a typical pyrometry setup illustrated in Figure 32, the solid angle is $\Omega = \pi D^2/4d^2$, where D is the lens (receptor) diameter, and d is the working distance between the lens and the light source .

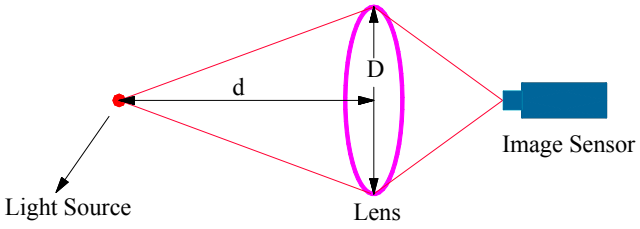

Figure 32 Schematic diagram of the color-band pyrometry

Assuming the total effective extended source area is A_1, the spectral radiant power and total radiant power incident on the lens is $\Phi_{i,\lambda} = B_\lambda A_1 \pi D^2/4d^2$, and $\Phi_i = BA_1 \pi D^2/4d^2$.

If the transmittance (which is the is the ratio of the total radiant or luminous flux transmitted by a transparent object to the incident flux, usually given for normal incidence) of the optical system is τ_λ, the spectral energy incident on the imaging sensor will be $\Phi_{i,\lambda,sensor} = B_\lambda \tau_\lambda A_1 \pi D^2/4d^2$. With an effective image area of A_2 on the imaging sensor, which corresponds to the effective extended light source area, and a

pixel/cell area of a on the CCD or CMOS sensor, the spectral irradiance obtained by a specific pixel/cell will be $E_\lambda = B_\lambda \tau_\lambda a A_1 \pi D^2 / 4 d^2 A_2$. Generally, A_2 / A_1 is proportional to the magnification factor of the lens, and here we can use X to replace it.

Usually there are two methods to describe the spectral sensitivity/responsivity, S_λ, of an imaging sensor. One is quantum efficiency (QE, electrons/photon), which is the photon-to-electron conversion efficiency; the other one uses the energy to electron conversion efficiency. In addition, the electron to digital number (pixel intensity) conversion is related the gain value of the CCD or CMOS camera.

The energy of a photon with specific frequency or wavelength is $E = hc/\lambda$. If QE is used as the spectral sensitivity/responsivity, with an exposure time of Δt , the digital number (DN) or pixel intensity of any pixel in the image is calculated by Equation (5) for an ideally performing (perfectly linear) black-and-white CCD or CMOS camera based on the optical system and camera characteristics illustrated above.

where, α is a proportional factor which ensures the units consistent for the equation,

$$DN = \alpha \cdot \frac{\pi}{4} \cdot \left(\frac{D}{d}\right)^2 \cdot f(g) \cdot \frac{a}{X} \cdot \Delta t \cdot \int_{\lambda_1}^{\lambda_2} \varepsilon_\lambda \tau_\lambda S_\lambda \cdot \frac{C_1 \cdot \lambda^{-5}}{e^{C_2/\lambda \cdot T} - 1} \cdot \left(\frac{h \cdot c}{\lambda}\right)^{-1} \cdot d\lambda \,, \qquad (5)$$

and $f(g)$ is a function of gain value of the camera; all other variables are explained earlier and in the nomenclature.

The spectral radiances of the object surface from the lowest wavelength to the highest wavelength that can be detected by the image sensor all contribute to the pixel intensity, by contrast to only two narrow wavelengths in traditional two-color pyrometry. This dramatically increased the signal strength.

If the spectral responsivity uses the energy to electron conversion efficiency, $(h \cdot c/\lambda)^{-1}$ needs to be removed from the above equation, as shown in Equation (6). This equation can be simplified if spectral emissivity is independent of wavelength.

$$DN = \alpha \cdot \frac{\pi}{4} \cdot \left(\frac{D}{d}\right)^2 \cdot f(g) \cdot \frac{a}{X} \cdot \Delta t \cdot \int_{\lambda_1}^{\lambda_2} \varepsilon_\lambda \tau_\lambda S_\lambda \cdot \frac{C_1 \cdot \lambda^{-5}}{e^{C_2/\lambda \cdot T} - 1} d\lambda \tag{6}$$

By far the most common method of rendering color images in commercial digital cameras involves creating a color filter mosaic array (CFA) on top of a light intensity (black-and-white) imager. In most cases, a 3-color, red-green-blue (RGB) pattern appears in the CFA, though there are other options, including 3-color complementary YeMaCy arrays, mixed primary/complementary colors, and 4-color systems where the fourth color is white or a color with shifted spectral sensitivity. One manufacturer (Foveon) uses a system that separates color based on penetration depth of the signal in the silicon detector with no mosaic filter.

A Bayer filter mosaic, as shown in Figure 33, represents the most commonly used CFA for arranging RGB color filters on a square grid of photo sensors. This term comes from the name of its inventor, Bryce Bayer of Eastman Kodak, and refers to the particular arrangement of color filters used in most single-chip digital cameras. Bryce Bayer's patent called the green photo sensors luminance-sensitive elements and the red and blue ones chrominance-sensitive elements. He used twice as many green elements as red or blue to mimic the human eye's greater resolving power with green light. These elements are referred to as samples and after interpolation become pixels.

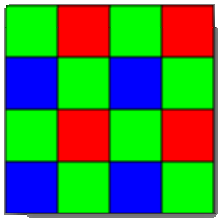

Figure 33 Bayer filter color pattern (Bayer)

There are a number of different ways the pixels are arranged in practice, but the pattern shown in Figure 33 with alternating values of red (R) and green (G) for odd rows and alternating values of green (G) and blue (B) for even rows is very common. The raw output of Bayer-filter cameras is referred to as a Bayer Pattern image. Since each pixel is filtered to record only one of the three colors, two-thirds of the color data are missing from each, as illustrated in Figure 34. The green is usually read out as two separate fields or as one field with twice as many points.

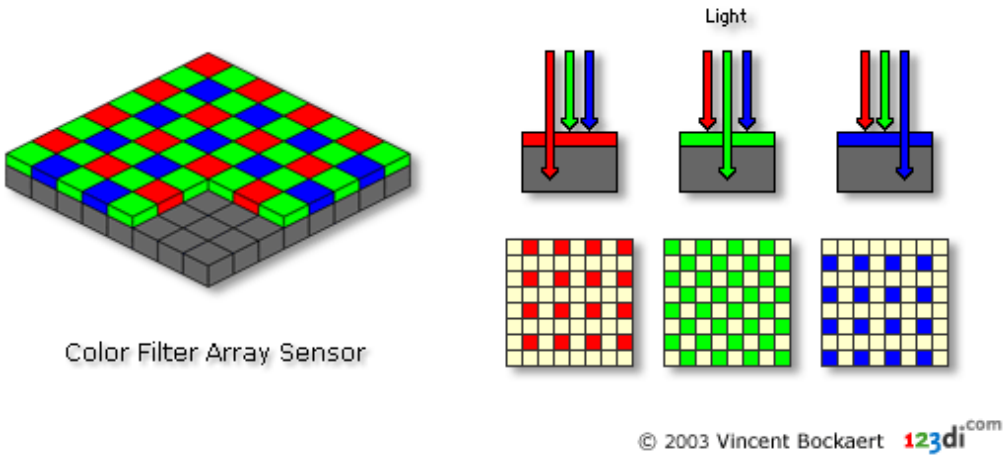

Figure 34 Color image reconstruction from a Bayer filter (Bockaert, 2003)

A demosaicing algorithm interpolates a complete RGB set for each point and produces the RGB image. Many different algorithms exist and they are one of the distinguishing factors in commercial cameras that otherwise often use the same sensors. The simplest is the bilinear interpolation method. In this method, the red value of a non-red pixel is computed as the average of the adjacent red pixels, and similar for blue and green.

With the Bayer filter in front of the CCD or CMOS sensor, sensor spectral responsivity can be measured for each individual color. As a result, the pixel intensity (or digital number) of the red color/channel is correlated with object temperature and red color/channel spectral responsivity as shown in Equation (7), and similarly for the other two colors/channels.

$$DN_{\mathrm{Re}\,d} = \alpha \cdot \frac{\pi}{4} \cdot \left(\frac{D}{d}\right)^2 \cdot f\left(g_{\mathrm{Re}\,d}\right) \cdot \frac{a}{X} \cdot \Delta t \cdot \int_{\lambda_1}^{\lambda_2} \varepsilon_\lambda \tau_\lambda S_{\lambda,\mathrm{Re}\,d} \cdot \frac{C_1 \cdot \lambda^{-5}}{e^{C_2/\lambda \cdot T} - 1} d\lambda \qquad (7)$$

Occasionally, a manufacturer provides the color or black-and-white spectral responsivity of CCD or CMOS cameras. To calculate the object surface temperature, Equation (7) applies to each color (typically RGB) channels. Assuming both spectral emissivity and spectral transmission are independent of wavelength and setting the gain value of each color to be the same, a new equation with only one (implicit) unknown – the temperature – results, as shown in Equation (8). This is the basic equation for the color-band method. Any two of the three channels/colors can be used to calculate the object surface temperature based on the pixel intensity of each color. This technique is flexible. The camera doesn't have to be focused on the surface of the object for a reliable temperature, though it does have to be focused for reliable spatial distributions of

temperature and, in all cases, only pixels with light that originates from the surface are valid pixels for temperature measurement. Images with poor focus contain many pixels with mixed particle-background light. In addition, working distance, lens aperture size, and exposure time all provide additional adjustable parameters that impact signal level. It is not necessary to measure working distance and aperture size. Only exposure time might be needed, which can be controlled and read through the camera control software.

$$\frac{DN_{Blue}}{DN_{Red}} = \frac{\int_{\lambda_1}^{\lambda_2} S_{\lambda,Blue} \cdot \frac{C_1 \cdot \lambda^{-5}}{e^{C_2/\lambda \cdot T} - 1} d\lambda}{\int_{\lambda_1}^{\lambda_2} S_{\lambda,Red} \cdot \frac{C_1 \cdot \lambda^{-5}}{e^{C_2/\lambda \cdot T} - 1} d\lambda} \tag{8}$$

4.3.2. CMOS-Camera-Based Color-band Pyrometry

In this project, a CMOS camera from EPIX Inc. (model SV2112) was first used to measure black-body temperature (Mikron Model M330). The camera uses a PixelCam™ ZR32112 CMOS sensor. Spectral responsivities of each color/channel, as well as the monochrome, are shown in Figure 35. The IR filter in front of the CMOS sensor in the camera was removed to obtain maximum response from the camera since near-infrared signal is critical at low temperature measurements, as indicated by Planck's law.

Using the spectral responsivity curves obtained from the manufacture and without calibrating the SV2112 CMOS camera, temperatures of a black body were measured by both a type-K thermocouple and the CMOS camera. The XCAP image acquisition and process software provided Pixel intensity of each color. The junction-compensated-thermocouple data compared with the camera measurements appear in Figure 36.

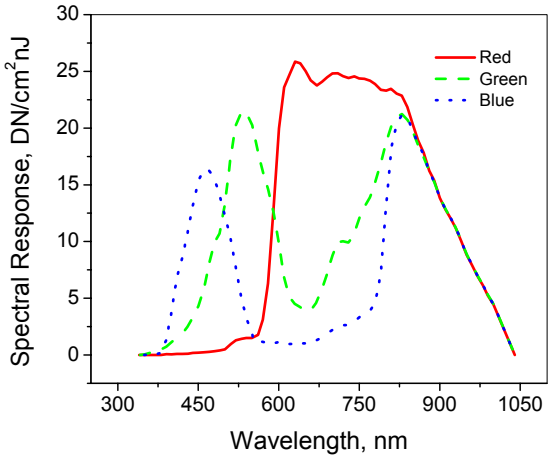

Figure 35 Spectral responsivity of the ZR32112 CMOS sensor (Epix Inc)

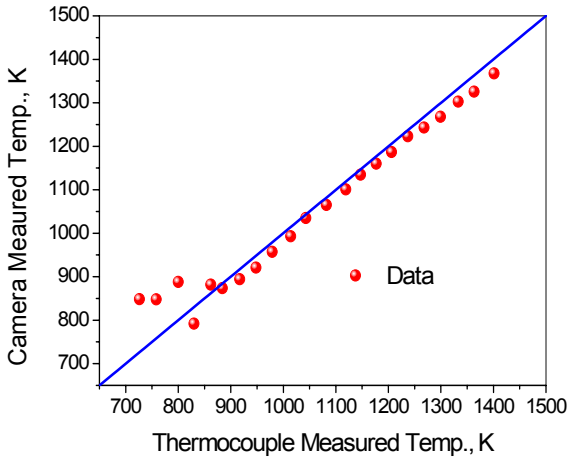

Figure 36 Temperature comparison of thermocouple and CMOS camera measurements

When the black-body temperature was higher than 900 K, the differences between the camera-measured temperature data and the thermocouple results were less than 50 K. Due to the spectral responsivity similarity of the three colors/channels in the near IR range (λ >800 nm) where low temperature radiation dominates, the camera measurements differ by more than 100 K from the black-body temperature and are

scattered at temperatures below 900 K. Figure 37 illustrates this issue, the data for which are based on Equation (8). When the black-body temperature is lower than 900 K, the pixel intensity ratio of any two colors/channels approaches 1.0, making accurate temperature measurement difficult.

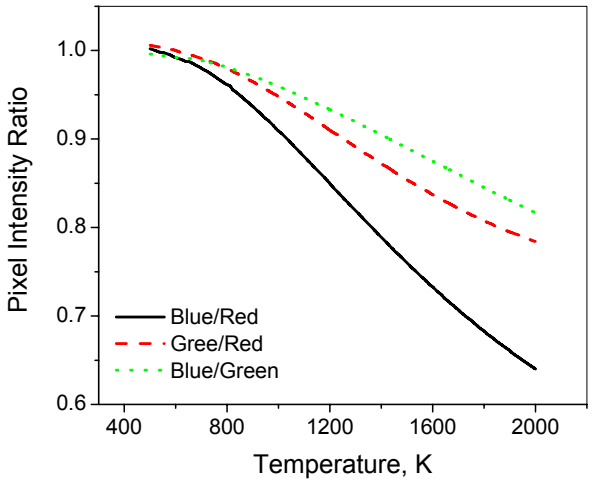

Figure 37 CMOS camera pixel intensity ratios as functions of temperature

It is commonly believed that CMOS sensors exhibit a slightly higher spectral responsivity than CCD sensors, especially at the near infrared (NIR) range. But CCD sensors commonly perform better than CMOS sensors with respect to uniformity, signal to noise ratio, and dynamic range. The low to moderate uniformity and signal to noise ratio may also contribute to the inaccuracy of temperature measurement of the SV2112 COMS camera at the low temperature range.

To obtain better temperature measurement results, a CCD camera was also used in this project.

4.3.3. CCD-Camera-Based Color-band Pyrometry

The SVS285CLCS camera uses a Sony Exview HAD CCD, which has very high sensitivity and low smear. This sensor shows higher sensitivity at the NIR range than traditional CCD due to the Exview HAD CCD technology. Similar to the CMOS camera, the IR filter was removed from the camera to maximize detectivity. The available spectral responsivity graph from the manufacturer appears in Figure 38, which only gives the visible spectral range.

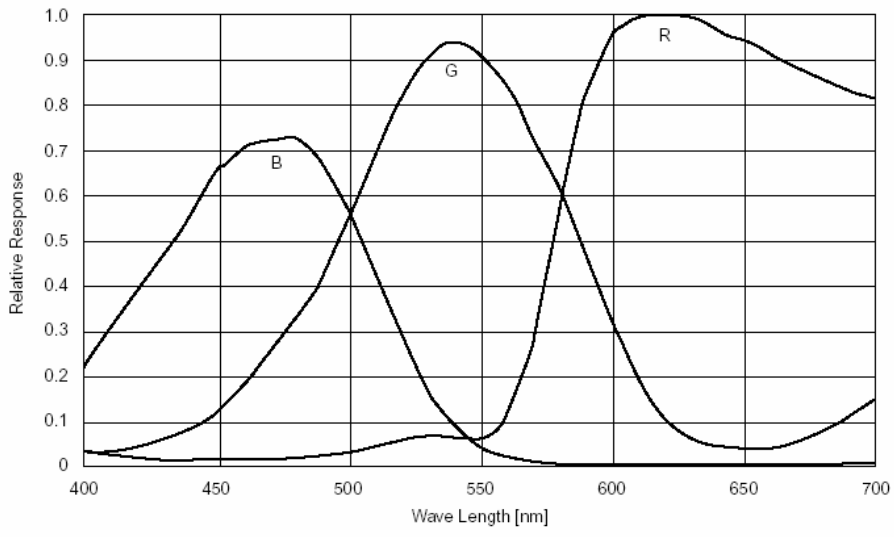

Figure 38 Manufacturer provided ICX285AQ CCD sensor spectral responsivity (Sony Inc, 2005)

The complete spectral responsivity of each color/channel was measured with a black body as light source and a monochromator (CornerStone 130) separating the broad-band light into narrow-wavelength signals with a resolution of 0.5 nm. The black body temperature was set to 1600 ^{o}C to maximize the signal/noise ratio. The measured wavelength range is from 300 nm to 1150 nm. A high-pass filter (LPF750 Lot NNB)

placed between the camera and the outlet of the monochromator blocked the second- and higher-order diffractions when measuring wavelengths longer than 750 nm. Both the spectral efficiency of the monochromator and the transmission efficiency of the filter impact the calculation of the spectral responsivity of the CCD sensor. Energy carried by a specific wavelength signal was calculated by Plank's law. The mathematical calculation of spectral responsivity for each color/channel appears as Equation (9).

$$S_{\lambda,color} = \frac{DN_{color,\lambda}}{\tau_{filter,\lambda} \quad \xi_{mono,\lambda} \quad \frac{C_1 \quad \lambda^{5}}{e^{C_2/\lambda \; T_B} \quad 1}}, \tag{9}$$

where, $color$ = Red, Green, and Blue. $\tau_{filter,\lambda}$ is the transmittance of the high pass filter, $\xi_{mono,\lambda}$ is the spectral efficiency of the monochromator, $DN_{color,\lambda}$ is the digital number or pixel intensity of each color at λ.

A complete relative spectral responsivity of each color/channel normalized by the maximum value, which occurred in the red color/channel, appears in Figure 39. The spectral responsivity data for each channel as a function of wavelength appears in Appendix B. The measured spectral responsivity curves of the CCD camera have similar shapes as those obtained from manufacturer for the CCD sensor. The small differences may arise from sample-to-sample variations in the sensors (manufacturer's data are typical but not obtained on each sensor), the camera characteristics, and the transmittance of the camera lens.

With the measured relative spectral responsivity curves, the pixel intensity ratios of any two colors/channels appear in Figure 40. The ratio of blue to red depends more

strongly on temperature than the other two ratio values, as would be expected since they differ the greatest in average wavelength. This ratio should result in the most sensitive/accurate temperature measurement.

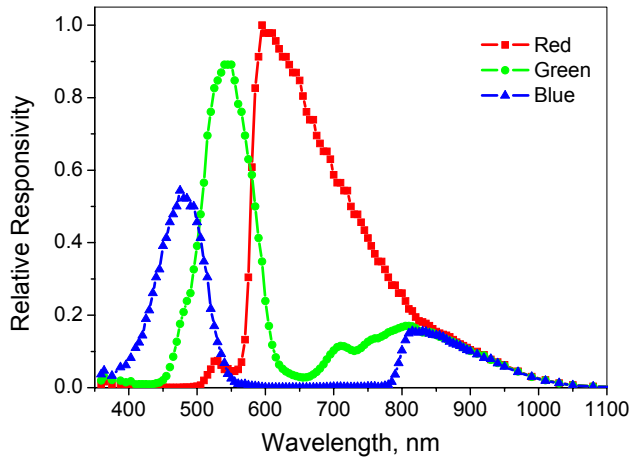

Figure 39 Measured relative spectral responsivity of the SVS285CSCL camera

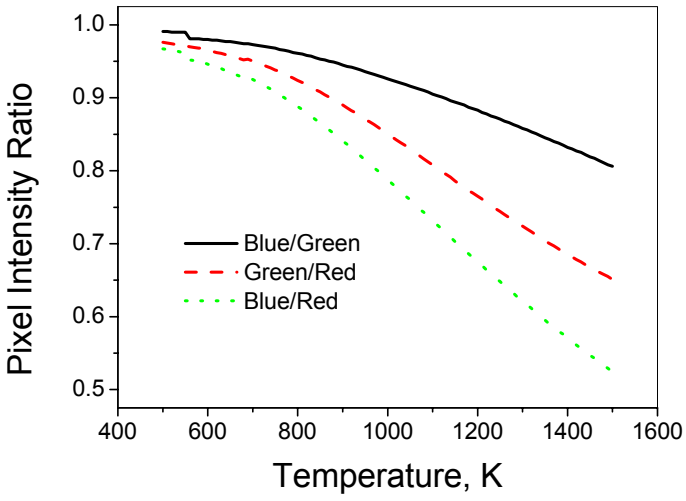

Figure 40 CCD camera pixel intensity ratios as functions of temperature

Figure 40 shows that the CCD camera is able to measure a wider temperature range compared with the CMOS camera since the CCD camera pixel intensity ratios approach 1.0 at lower temperature (~650 K). The black-body temperatures were then measured with this CCD camera and calculated using Equation (8) and the complete spectral responsivities. The camera measured data compared with thermocouple measurements appear in Figure 41, again without calibration. The results show that the CCD camera measurements were within 50 K of the thermocouple measured values when black-body temperature is lower than 1050 K, but the sensor appears to begin to saturate at higher temperatures. Further calibration is necessary for more accurate and wider temperature measurements.

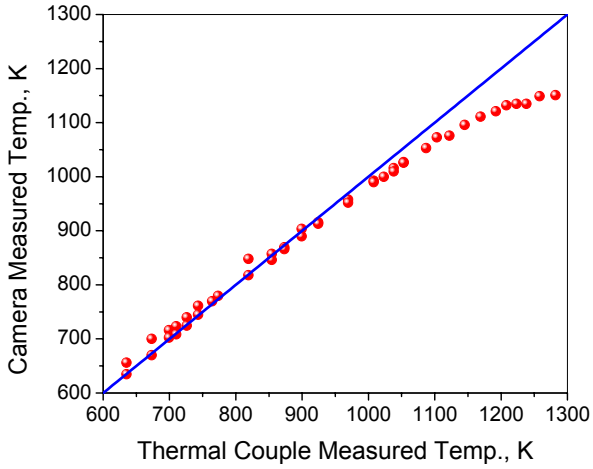

Figure 41 Temperature comparison of thermocouple and CCD camera measurements

To calibrate the CCD camera and make this method more robust, four variables were studied: the square of lens aperture size divided by the square of the working distance, D^2/d^2 ; exposure time, Δt ; black-body temperature, T ; and camera gain value, g .

The first investigation explored the linearity implied by Equation (6) between the pixel intensity and D^2/d^2. Aperture size adjustments produced image pixel intensity data as a function of D^2 at a variety of temperatures and exposure times. Results indicated an almost perfectly linearity in all cases (Figure 42). Here only two cases appear: low temperature and long exposure time data appear in Figure 42 (a) and high temperature and short exposure time data appear in Figure 42 (b). In the calibration, working distance remained constant and only aperture size changed since D^2 and $1/d^2$ should have identical effects.

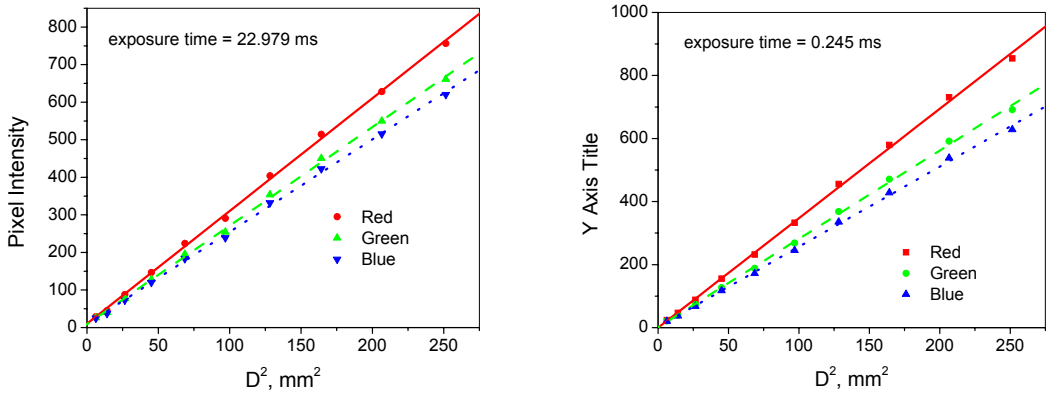

(a) low temperature at 927 K (b) higher temperature at 1224 K

Figure 42 Pixel intensity vs. effective aperture area

The camera gain value function, $f(g)$, was calibrated for each channel at different temperatures and exposure times. For each channel at any condition, the gain value function, $f(g)$, followed the form of $e^{\gamma \cdot g}$, as shown in Figure 43. The parameter γ in this function was found almost constant, so an average value was calculated for each

channel: 3.424, 3.424, and 3.428, respectively for red, green, and blue channels. They can be treated as the same for each channel to simplify the color-band method.

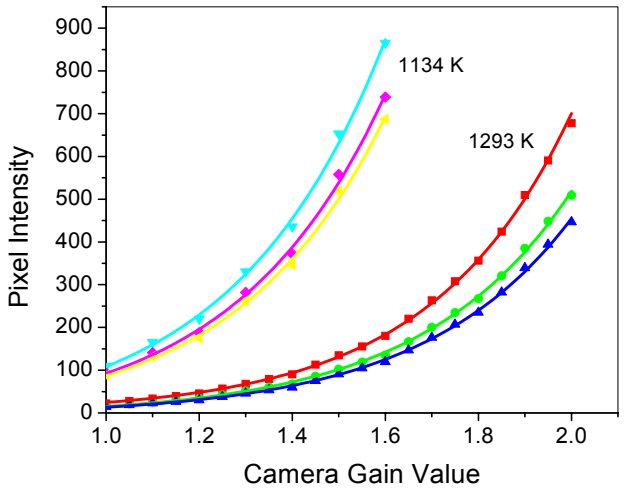

Figure 43 Camera gain value calibration

During the calibration, it was also found when black body temperature was higher than about 850 K, the image pixel intensity was nearly proportional to exposure time, but both the slope and intercept of the straight line started to increase with increasing black body temperature, as shown in Figure 44. The green channel and blue channel behaved similarly, and only the red channel appears here. These data follow a linear correlation but with a non-zero intercept, Equation (10), between the pixel intensity and exposure time when black body temperature is higher than 850 K. Both the slope and intercept are functions of the energy received by the CCD camera sensor, increasing with black body temperature increase.

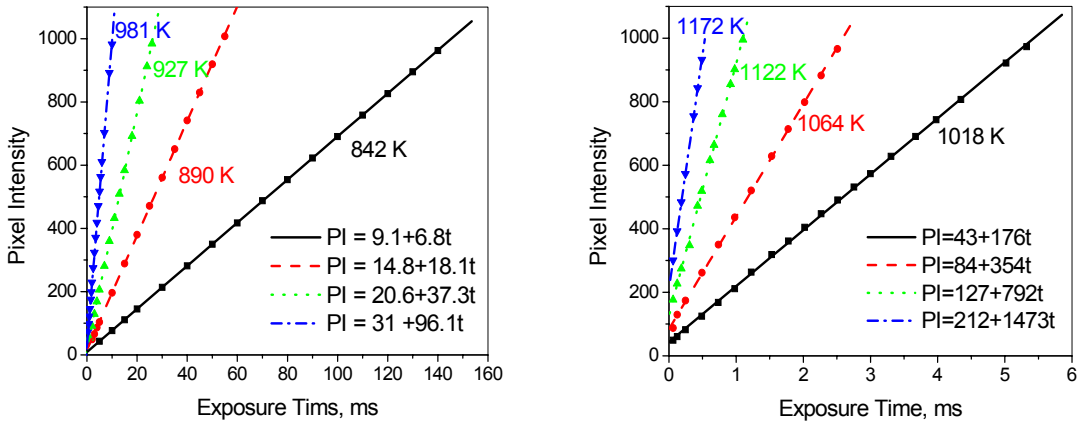

(a) low temperature (b) higher temperature

Figure 44 Red channel pixel intensity vs. exposure time at different temperature

$$DN_{Red} = a_{Red}(E_{Red})\Delta t + b_{Red}(E_{Red})$$

where,

$$E_{Red} = \int_{\lambda_1}^{\lambda_2} S_{\lambda,Red} \cdot \frac{C_1 \cdot \lambda^{-5}}{e^{C_2/\lambda \cdot T} - 1} d\lambda \qquad (10)$$

To determine the exact relation between the energy and slope, as well as that between the energy and intercept, black-body temperature was changed from about 850 K to 1312 K in increments of about 80 K. The slope and intercept in Equation (10) were calculated by adjusting the exposure time at each temperature. Both slope and intercept fit power functions of the energy, as shown in Figure 45. The camera was also calibrated at higher temperature range (>1273 K) with a high-power black body. The fitted functions were slightly different from what fitted for moderate temperature range, as shown in Figure 46.

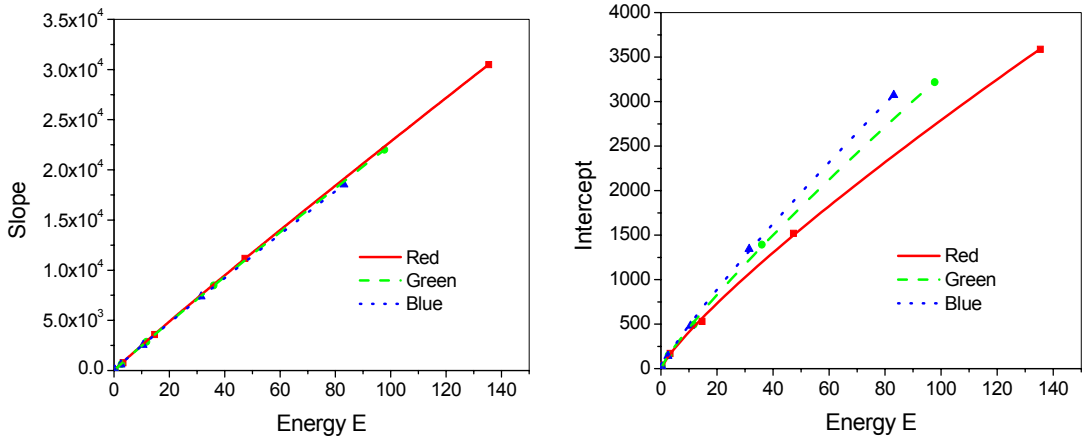

(a) Slope (b) Intercept

Figure 45 Slope and intercept vs. energy at moderate temperature range

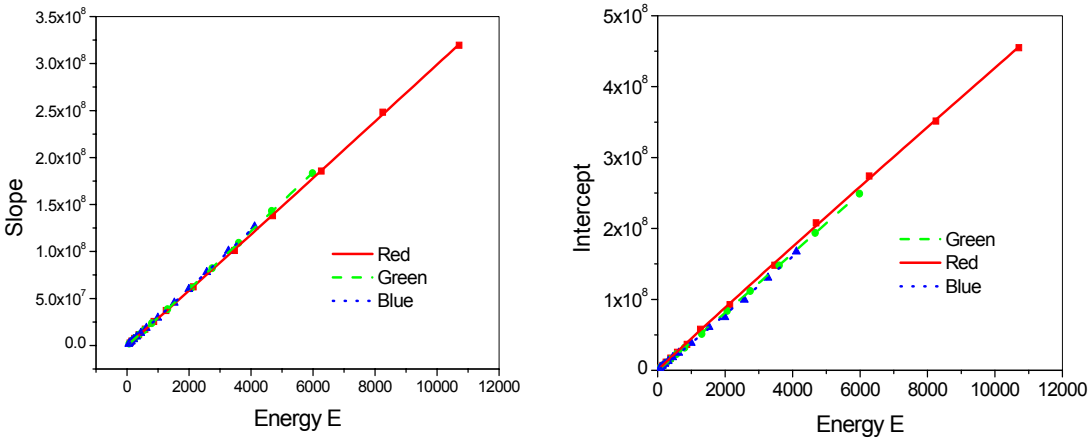

(a) Slope (b) Intercept

Figure 46 Slope and intercept vs. energy at higher temperature range (>1273 K)

The final calibrations appear as Equation (11) for moderate- and Equation (12) for high-temperature ranges. The simplest form Equation (7) can be used to calculate low-temperature results by the color-band method.

$$
\begin{aligned}
DN_{\mathrm{Re}\,d} &= \alpha \cdot \left(\frac{D}{d}\right)^2 \cdot e^{3.424 \cdot g} \cdot \left(\Delta t \cdot 280 \cdot E_{\mathrm{Re}\,d}(T)^{0.958} + 60.5 \cdot E_{\mathrm{Re}\,d}(T)^{0.83}\right) \\
DN_{Green} &= \alpha \cdot \left(\frac{D}{d}\right)^2 \cdot e^{3.424 \cdot g} \cdot \left(\Delta t \cdot 272 \cdot E_{Green}(T)^{0.959} + 63.4 \cdot E_{Green}(T)^{0.86}\right) \\
DN_{Blue} &= \alpha \cdot \left(\frac{D}{d}\right)^2 \cdot e^{3.428 \cdot g} \cdot \left(\Delta t \cdot 272 \cdot E_{Blue}(T)^{0.955} + 65 \cdot E_{Blue}(T)^{0.87}\right)
\end{aligned} \tag{11}
$$

$$
\begin{aligned}
DN_{\mathrm{Re}\,d} &= \alpha \cdot \left(\frac{D}{d}\right)^2 \cdot e^{3.424 \cdot g} \cdot \left(\Delta t \cdot 264 \cdot E_{\mathrm{Re}\,d}(T)^{1.013} + 526 \cdot E_{\mathrm{Re}\,d}(T)^{0.977}\right) \\
DN_{Green} &= \alpha \cdot \left(\frac{D}{d}\right)^2 \cdot e^{3.424 \cdot g} \cdot \left(\Delta t \cdot 254 \cdot E_{Green}(T)^{1.022} + 344 \cdot E_{Green}(T)^{1.022}\right) \\
DN_{Blue} &= \alpha \cdot \left(\frac{D}{d}\right)^2 \cdot e^{3.428 \cdot g} \cdot \left(\Delta t \cdot 252 \cdot E_{Blue}(T)^{1.024} + 307 \cdot E_{Blue}(T)^{1.032}\right)
\end{aligned} \tag{12}
$$

If the CCD sensor spectral responsivities were measured accurately enough, all three colors/channels of the camera should have the same digital number vs. energy correlation. The discrepancy might be introduced by the errors in spectral responsivity measurements.

Both Figure 45 and Figure 46, as well as Equations (11) and (12) showed that the slope and intercept became more linear with respect to the received energy when black body temperature increased. With the equations obtained, the black-body temperature was measured by the color-band method at random working distance and random exposure time. Results compared with thermocouple data appear in Figure 47.

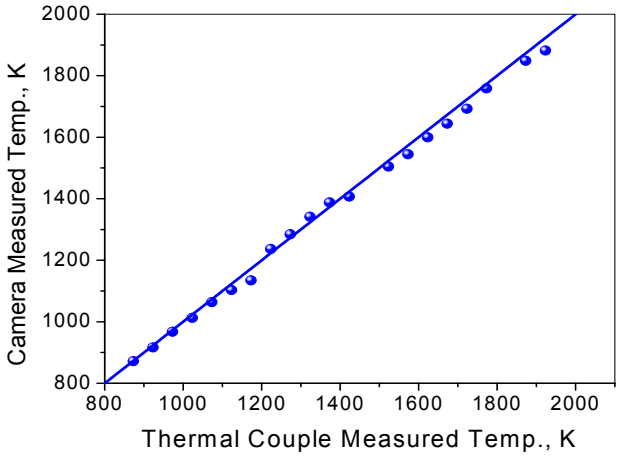

Figure 47 Black body temperature measured by the calibrated CCD camera

4.3.4. Particle Temperature Measurements Correction for Reflection Effects in Furnace

If the particle is heated in a furnace and the furnace wall temperature differs from the particle surface temperature, the measurement has to be corrected by taking surface reflection effects into account.

To simplify the correction, the following assumptions were made:

- The wall temperature and surface properties are uniform;
- All energy is emitted and reflected diffusely;
- Both the particle and the wall surfaces are gray;
- The particle surface is convex;
- The incident and hence reflected energy flux is uniform over the surface area;
- The reactor is considered as an enclosure and the particle is located in the center of the reactor.

Based on the above assumptions, a heat transfer diagram between the particle and the wall surface appears in Figure 48. The surface areas are A_1, A_2, and A_v for particle,

reactor, and the view port hole, respectively. Particle surface temperature is T_1 and T_2 designates the reactor wall. It is also assumed that the surface areas of the particle and the view port are much less than that of the reactor wall: $A_1 << A_2$ and $A_V << A_2$.

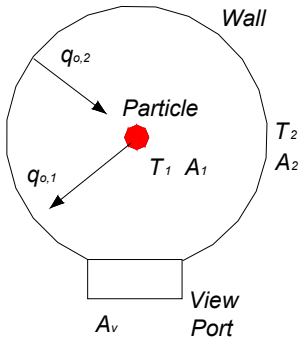

Figure 48 Radiant heat interchange between particle and reactor wall

Geometric configuration factors (Siegel and Howell, 2002) of the particle surface and the reactor surface are $F_{1-1}, F_{1-2}, F_{2-1}, \text{and } F_{2-2}$. By analyzing the radiant energy interchange between the particle surface and the reactor wall, the radiant energy flux leaving the particle surface $q_{o,1}$ and that leaving the reactor wall surface $q_{o,2}$ were developed, as shown in Equations (13) and (14).

$$q_{o,1} = \varepsilon_1 \sigma T_1^4 + (1-\varepsilon_1)(F_{1-1} q_{o,1} + F_{1-2} q_{o,2}) \tag{13}$$

$$q_{o,2} = \varepsilon_2 \sigma T_2^4 + (1-\varepsilon_2)(F_{2-1} q_{o,1} + F_{2-2} q_{o,2}) \tag{14}$$

Substituting Equation (14) into Equation (13) results in Equation (15).

$$q_{o,1} = \frac{[1-(1-\varepsilon_2)F_{2-2}]\varepsilon_1 \sigma T_1^4 + (1-\varepsilon_1)\varepsilon_2 \sigma T_2^4}{[1-(1-\varepsilon_2)F_{2-2}] + [(1-\varepsilon_1)(1-\varepsilon_2)F_{2-1}]} \tag{15}$$

The above equation can be simplified for this system. The assumption of convex particle surface leads to $F_{1-1}=0$ and $F_{1-2}=1$ since $F_{1-1}+F_{1-2}=1$. According to the reciprocity relation between any two radiant elements, $F_{1-2}\cdot A_1 = F_{2-1}\cdot A_2$, the radiant energy leaving the reactor wall that arrives the particle surface is $F_{2-1}=A_1/A_2$. Similarly, it is straightforward to get $F_{2-2}=1-A_1/A_2$. So, $F_{2-1}=0$ and $F_{2-2}=1$ since $A_1 << A_2$. Equation (15) then simplifies to Equation (16). Equation (15) also simplifies to Equation (16) if the emissivity of the reactor wall is 1.0.

$$q_{o,1}=\varepsilon_1\sigma T_1^4+(1-\varepsilon_1)\sigma T_2^4 \tag{16}$$

Similarly, the spectral radiant energy flux leaving the particle surface may be obtained as Equation (17).

$$q_{o,1,\lambda}=\varepsilon_1\frac{C_1\cdot\lambda^{-5}}{e^{C_2/\lambda\cdot T_1}-1}+(1-\varepsilon_1)\frac{C_1\cdot\lambda^{-5}}{e^{C_2/\lambda\cdot T_2}-1} \tag{17}$$

For color-band pyrometry with Equation (8), the corrected equation results from replacing the Plank's radiant energy with Equation (17). The result appears in Equation (18).

$$\frac{DN_{Blue}}{DN_{Red}}=\frac{\int_{\lambda_1}^{\lambda_2}S_{\lambda,Blue}\cdot\left(\varepsilon_1\frac{C_1\cdot\lambda^{-5}}{e^{C_2/\lambda\cdot T_1}-1}+(1-\varepsilon_1)\frac{C_1\cdot\lambda^{-5}}{e^{C_2/\lambda\cdot T_2}-1}\right)d\lambda}{\int_{\lambda_1}^{\lambda_2}S_{\lambda,Red}\cdot\left(\varepsilon_1\frac{C_1\cdot\lambda^{-5}}{e^{C_2/\lambda\cdot T_1}-1}+(1-\varepsilon_1)\frac{C_1\cdot\lambda^{-5}}{e^{C_2/\lambda\cdot T_2}-1}\right)d\lambda} \tag{18}$$

Similar equation can be established for any other two channel combination: blue/green or green/red, and both particle emissivity and particle surface temperature can be obtained simultaneously.

4.4. 3-D Particle Shape Reconstruction

Biomass particles usually present irregular shapes and larger size (~ 6+ mm) compared with pulverized coal. The surface-area-to-volume ratio of such a particle plays an important role in its combustion behavior since its combustion process is mainly heat- and mass-transfer controlled instead of kinetically controlled. A 3-dimensional (3D) particle shape reconstruction algorithm, developed in this project and applied for the first time to particle combustion, addresses experimental measurement and calculation of particle surface-area-to-volume ratios.

Substantial studies have been done for object 3-D shape reconstruction. For human face shape reconstruction, with some featured points on the 2-D images, a curved surface model (Komatsu, 1991) applies, which can reconstruct facial shape fairly well. Based on a projective grid space, multi-image projective reconstruction was developed from a large number of images (Saito and Kanade, 1999). Space carving (Kutulakos and Seitz, 2000) is another widely used shape reconstruction technique with multiple photographs taken at known but arbitrarily-distributed viewpoints. All the above techniques or algorithms present nearly insurmountable challenges for particles burning in a reactor: only limited optical access can be provided and no detailed features can be found on the image except the edge contour of the particle. A more practical and simple algorithm developed in this project appears below.

4.4.1. Image Acquisition and Processing

The algorithm developed in this project uses three images of a particle or object taken from three orthogonal directions with known orientation, as illustrated in Figure 49. The direction of the z coordinate in this system is opposite from a regular coordinate

(This is a left-hand rather than a right-hand xyz diagram) for operation convenience, but this is immaterial to this method and the mathematical reconstruction. If any camera is set with the specific viewpoint and orientation shown in Figure 49, the image taken with the camera can be rotated or flipped to meet the orientation requirements.

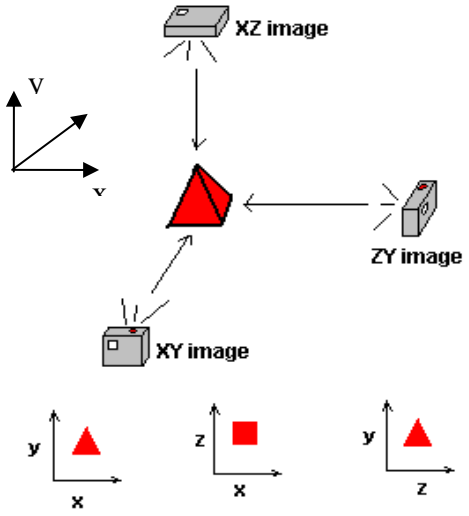

Figure 49 Camera setup orientation for imaging acquisition from three orthogonal direction

Three images taken for a popcorn ash (1-3 mm-sized fly ash) particle are named XY, XZ, and ZY, respectively, as shown in Figure 50. First, the edge contour in each image of the particle is detected using a color threshold which identifies those pixels that lie in the boundary between the background and the particle image, illustrated in Figure 50 by red traces. If the three images have different scales due to camera setup difference, they must be rescaled based on one known image.

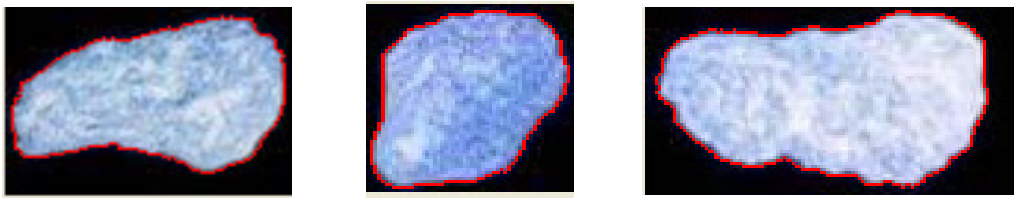

(a) XY image (b) XZ image (c) ZY image

Figure 50 Three images of a popcorn ash particle taken from three orthogonal directions

4.4.2. Image Contour Alignment

On the edge contour trace in each 2-D image, four extreme points exist that have either minimal or maximum horizontal/vertical coordinates. A simple example is used to illustrate the image alignment using six common points. As shown in Figure 51, the four extreme points in the XZ image are marked as MinX, MaxX, MinZ, and MaxZ. A total of twelve extreme points appear in these three image contours. As a result, the space coordinates of six common points can be determined for a particle. Strictly speaking, these points will only be common in the limit of infinite focal lengths, but in this application focal lengths are long compared to particle size and this is a minor issue.

For example, for the MinXy point in the XY image, its first two coordinates X and Y can be determined from the XY image. Assuming a convex particle surface, this point must correspond to the MinXz in image XZ. The third coordinate of this point must correspond to the point MinXz in the XZ image. Similarly, complete coordinates of another five points can be determined. With these six points, an approximate skeleton of the object is obtained, as shown in the right upper corner in Figure 51. Only two coordinates (XY, or XZ, or ZY) for those points on the lines between any two adjacent extreme points are known, so the cubic spline interpolation algorithm approximates the

third coordinate. A skeleton for the popcorn ash particle including eight surface segments (octants) results, as illustrated below.

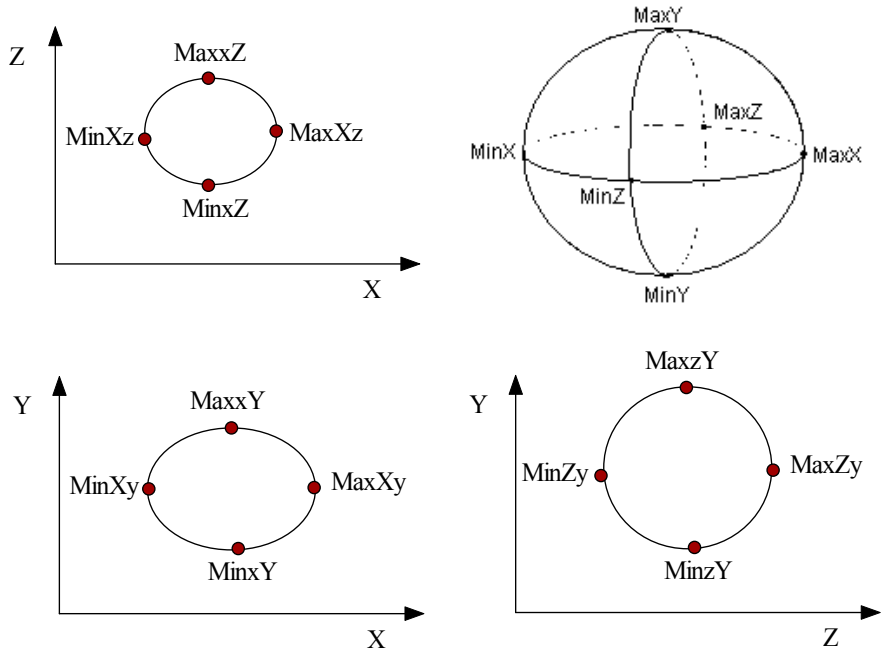

Figure 51 Image alignment illustration

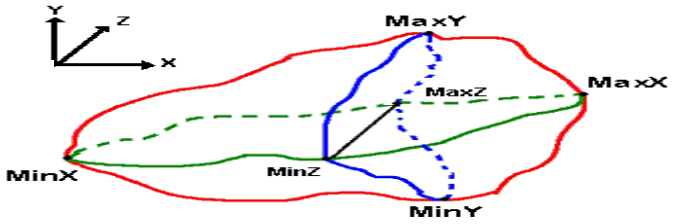

Figure 52 Popcorn ash particle skeleton after image contour alignment

4.4.3. Surface Generation

The exact locations of the points on the remaining particle surface lie between known bounds but cannot be precisely determined from this algorithm. In no case can the algorithm detect 3D concave features such as pits. However, the fixed or known points along the skeleton provide a means for estimating the remaining particle surface. An interpolation method called inverse distance weighting (IDW) generates surface point coordinates. IDW can be used both for curve fitting and surface fitting. A simple IDW weighting factor is $\omega(d) = 1/d^p$, where $\omega(d)$ is the weighting factor applied to a known value, d is the distance from the known value to the unknown value, and p is a user-selected power factor. Here weight decreases as distance increases from the known points. Greater values of p assign greater influence to values closest to the interpolated point. The most common value of p is 2.

A general form of interpolating a value using IDW is given in equation (19).

$$Z = \frac{\sum_i Z_i d_i^{-p}}{\sum_i d_i^{-p}},$$

where Z is the value of the interpolated point, Z_i is a known value, $d_i = \sqrt{x_i^2 + y_i^2}$ is the distance from the known point i to the unknown point. (19)

The alignment of the three traces divides the soon-to-be surface into eight areas, called octants. The inverse distance weighting (IDW) interpolation method applies to each octant separately, using the trace points that define the octant boundaries. The algorithm produces the same results along any boundary or at any fixed point

independent of the direction from which it is approached, ensuring smooth transitions from one octant to the next. The interpolation only determines the z value for a surface point in the XY plane, and the XY image is used as an outline that is filled with a 2-D grid of points. These points are assigned a Z value in the IDW interpolation. This makes the XY image a backbone in the algorithm in that it has more influence in the final shape of the object 3-D model than the other two images. This is not inherent in the algorithm. In principle, similar interpolations could be applied to each of the other planar images generating additional surface points. However, this has thus far proven both unnecessary and too time consuming in this project.

Two variables are used to adjust the reconstructed shape. In addition to the power factor, p, in the original IDW method, the XY influence coefficient provides some flexibility. This variable is not in the original IDW algorithm, but the effect of increasing this value is that the XY image's trace will have a greater influence of the Z value of interpolated points. It was discovered that the IDW interpolation algorithm worked well at generating a spherical shape, but not so well with a cubic shape. By manipulating the power factor p and XY influence coefficient, a cube-like shape reconstruction can be improved.

A reconstructed 3-D shape of the popcorn ash particle appears in Figure 53, with surface points interpolated by the modified IDW method. This image is more readily appreciated on a computer screen where it can be rotated and examined from various angles than in this projection.

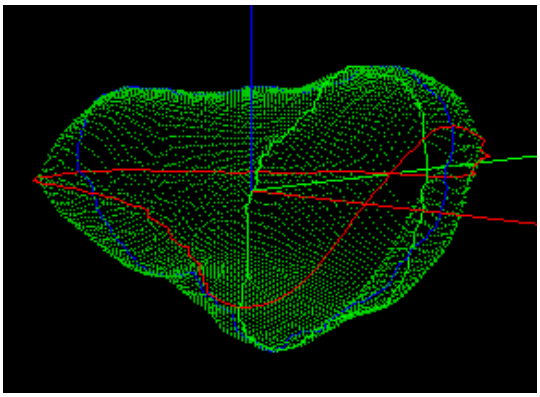

Figure 53 Reconstructed 3-D shape of a popcorn ash particle

Once the particle surface is generated, its surface area and volume can be calculated using the coordinates of all points on the surface. The calculated particle surface area of this popcorn ash particle is 1.59×10^{-4} m^2 and particle volume is 1.09×10^{-7} m^3.

For a reacting particle in a reactor, if its surface temperature distributions in all three 2-D images are calculated by the color-band method developed in this project, they can be mapped to the computer generated 3-D particle model surface.

The limitations of this particle shape reconstruction algorithm as well as its accuracy are discussed in Appendix C.

Both the particle shape reconstruction algorithm and temperature calculation algorithm are coded in the C++ computer language.

4.5. Summary

In this chapter, the experimental methods involved in investigating biomass particle or droplet combustion appear in reasonable detail. A sample preparation procedure to separate particles by shape and size is introduced. An entrained-flow reactor was designed and built to conduct sawdust particle combustion experiments; the structure and

specifications of the entrained-flow reactor are explained. The operation procedure of a single-particle reactor for poplar dowel particle combustion experiments is presented.

A color-band imaging pyrometry has been developed to measure particle surface temperature with CCD or CMOS digital cameras. In addition, a particle shape reconstruction algorithm was developed to calculate particle volume and surface area with three images taken from three orthogonal directions simultaneously.

5. Single Particle Combustion Model

The development of a single biomass particle combustion model is described in detail in this chapter, followed by the explaination of solution procedures for the partial differential equations of the model.

As a biomass particle travels through the entrained-flow reactor or hovers in the single-particle reactor with air as carrier gas, it exchanges energy by both radiation and convection and potentially provides an energy source or sink through reactions. The biomass particle undergoes the following processes at different residence times: drying, devolatilization, volatiles combustion, and gasification and oxidation of char, as show in Figure 54. These processes may occur individually or simultaneously depending on particle properties and reactor conditions: particle type, density, size, shape, reactor temperature, heating rate, and etc.

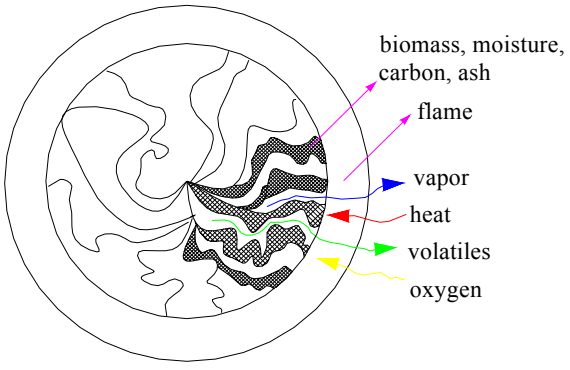

Figure 54 Particle combustion physical model with drying, devolatilization, char oxidation, gasification, and flame combustion

5.1. Mechanisms of Drying, Devolatilization, and Char Gasification and Oxidation

Moisture in biomass occurs in two forms: free water and bound water (Forest Products Laboratory United States Department of Agriculture Forest Service, 1999). Moisture content above the fiber saturation point (FSP) is free water, that is, exists in liquid form in pores and cells. Below the FSP moisture is bound water, that is, exists as moisture physically or chemically bound to surface sites or as hydrated species. The average FSP is 30% according to (Forest Products Laboratory United States Department of Agriculture Forest Service, 1999), which is the weight of water in the wood as a percentage of the weight of oven-dry wood (essentially water content on a dry basis). Traditionally, the forest products industries express moisture on this basis, so that 100% moisture means essentially half of the mass is water. Nuclear Magnetic Resonance (NMR) can determine free water and bound water contents (Guzenda and Olek, 2000). Free moisture vaporizes from both the internal and external surface at a rate determined by the surface saturated vapor pressure, the partial pressure of vapor in the gas phase, and the specific surface area of the particle. Bound water does not vaporize in a manner similar to free moisture but rather is released as a result of chemical reactions releasing bound hydrates and similar processes. Four basic methods, including a thermal model, equilibrium model, and chemical reaction model, describe wood drying under combustion heat fluxes (Bryden and Hagge, 2003). In this model, a mass transfer expression, with the difference between equilibrium vapor pressure and vapor partial pressure as the driving force, is used to describe both the evaporation of free water and recondensation of vapor. The evaporation rate of bound water is presented by a chemical reaction rate express (Chan et al., 1985). Figure 55 illustrates the drying scheme of moisture. The biomass particles used in the entrained-flow reactor experiments were

dried prior to use to maximize the particle size that can react in this residence-time-limited reactor. Drying of this nature removes all of the free moisture and bound water. Poplar particles used in the single-particle reactor usually have 6% moisture content, which is categorized as bound water. Samples with higher moisture content, up to 50%, were also prepared and used to collect free-water drying process data and validate the drying model.

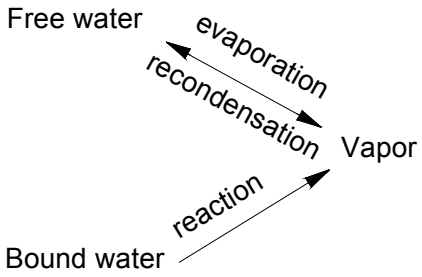

Figure 55 Moisture drying scheme

Devolatilization or pyrolysis involves heating of raw biomass components or organic materials in the absence of oxidizer, thermal degradation of the biomass components, mass transport of the devolatilization products by advection and diffusion, and escape of products at the surface of the particle. A few authors distinguish between pyrolysis and devolatilization, with the former occurring in a neutral or reducing environment and the latter in an oxidizing environment. Most particles thermally decompose within a volatile cloud (reducing environment) even when the overall environment is oxidizing, making this distinction somewhat ambiguous. The two terms are used interchangeably in this document, consistent with most of the literature. The two-stage wood pyrolysis kinetics model, shown in Figure 8, is chosen for this particle model since it is capable of

predicting the product yields and distribution variations with temperature and heating rate which are significantly influenced by particle shape and size.

The volatile yield from pyrolysis includes a complex mixture and more than one hundred hydrocarbons were found (Demyirbas, 2003; Evans and Milne, 1987a; Evans and Milne, 1987b). It is well known that pyrolysis product distribution depends strongly on reactor geometry, temperature, heating rate, residence time, and mass transfer velocity and pressure (Demyirbas, 2003). This complex mixture mainly consists of CO, CO_2, H_2O, H_2, light hydrocarbons and heavy hydrocarbons. The first five components are classified as light gas, and the last one as tar. For the light gas composition, results from Thunman et. al (Thunman et al., 2001) are used here to predict wood pyrolysis volatile components, with the mass fraction of each species listed in Table 10. To simplify the combustion behaviors of volatiles, the light hydrocarbon and heavy hydrocarbon are lumped together as hydrocarbons in the current investigation, and the lumped hydrocarbon molecule is $C_6H_{6.2}O_{0.2}$, consistent with published results (Thunman et al., 2001). In this model, hydrocarbon combustion in the gas phase occurs through a one-step global reaction according to the approximate composition of hydrocarbon, even though the combustion chemistry of a simple gas could be a complex phenomena (Warnatz, 2000). The reaction mechanism and kinetic parameters for the hydrocarbon combustion is based on the recommendations of Smoot and Smith (Smoot and Smith, 1985).

Table 10 Light gas composition produced during devolatilization

Components	H2	CO	CO2	H2O	Light hydrocarbon
Mass fraction	0.109	0.396	0.209	0.249	0.127

Char gasification and oxidation include five classic heterogeneous and homogeneous reactions, indicated as reactions 8 to 12 in Table 11. In coal char combustion, Reaction 8 is described by both first- and half-order expressions (Brewster et al., 1993; Smith et al., 1994). Biomass char reactivity literature is less substantial than for coal char, but it is believed that biomass char has slightly higher reactivity than that of coal (Blackham et al., 1994; Di Blasi et al., 1999; Evans and Emmons, 1977; Wornat et al., 1999). The oxidation rate of biomass char varies between a half- and first-order, as demonstrated by Janse et.al (Janse et al., 1998). According to Bryden's (Bryden, 1998) analysis, lignite's kinetic parameters are used for wood char oxidation since wood char more closely resembles lignite than other coal types. The oxidation kinetic mechanisms make this model more robust, but in practice oxidation occurs mostly under diffusion-controlled conditions, in which case the details of the kinetics are immaterial.

Chemical reactions and phase changes, together with their corresponding rate expressions during drying, devolatilization, and char oxidation processes, appear in Table 11.

Table 11 Chemical reactions, phase change and rate expressions

Reaction index	Reaction description	Rate expression	Reference
1	Biomass → light gas	$r_1 = \frac{\partial \rho_B}{\partial t} = k_1 \rho_B$	
2	Biomass → tar	$r_2 = \frac{\partial \rho_B}{\partial t} = k_2 \rho_B$	
3	Biomass → char	$r_3 = \frac{\partial \rho_B}{\partial t} = k_3 \rho_B$	
4	Tar → light gas	$r_4 = \frac{\partial \rho_G}{\partial t} = \varepsilon k_4 \rho_g Y_T$	

(Table 11 continued)

5	Tar → char	$r_5 = \frac{\partial \rho_C}{\partial t} = \varepsilon k_5 \rho_g Y_T$	
6	H_2O (l, free) ↔ H_2O (g)	$r_6 = \frac{\partial \rho_{fw}}{\partial t} = s_a \frac{\rho_{fw}}{\rho_{fw}^0} h_{m,pore}(\rho_v^{sat} - Y_V \rho_g)$	
7	H_2O (l, bound) → H_2O (g)	$r_7 = \frac{\partial \rho_{bw}}{\partial t} = k_7 \rho_{bw}$	(Chan et al., 1985)
8	C + 1/2 O_2 → CO	$r_8 = \frac{\partial C_{O_2}}{\partial t} = s_{a,char} \frac{\rho_C}{\rho_C + \rho_B + \rho_A} k_8 \varepsilon C_{O2}$	(Evans and Emmons, 1977)
9	C + CO_2 → 2CO	$r_9 = \frac{\partial C_{CO_2}}{\partial t} = s_{a,char} \frac{\rho_C}{\rho_C + \rho_B + \rho_A} k_9 \varepsilon C_{CO_2}$	(Brewster et al., 1993)
10	C + H_2O → CO + H_2	$r_{10} = \frac{\partial C_{H_2O}}{\partial t} = s_{a,char} \frac{\rho_C}{\rho_C + \rho_B + \rho_A} k_{10} \varepsilon C_{H_2O}$	(Brewster et al., 1993)
11	1/2 O_2 + CO → CO_2	$r_{11} = \frac{\partial C_{CO}}{\partial t} = k_{11} C_{CO} C_{O_2}^{0.25} C_{H_2O}^{0.5}$	(Hautman et al., 1981)
12	H_2 + 1/2 O_2 → H_2O	$r_{12} = \frac{\partial C_{H_2}}{\partial t} = k_{12} C_{H_2} C_{O_2}^{1.42}$	(Hautman et al., 1981)
13	$C_6H_{6.2}O_{0.2}$ + 2.9O_2 → 6CO + 3.1H_2	$r_{13} = \frac{\partial C_{HC}}{\partial t} = k_{13} C_{HC}^{0.5} C_{O_2}$	(Smoot and Smith, 1985)

Arrhenius expressions describe the temperature dependence of the kinetic rate coefficients for reactions 1-5 and 7-13, as indicated in Equations (20) and (21).

In reactions 1-5, 7, and 11-13,

$$k_i = A_i \exp\left(-\frac{E_i}{RT}\right); \tag{20}$$

and in Reactions 8 – 10,

$$k_i = A_i T \exp\left(-\frac{E_i}{RT}\right). \tag{21}$$

The literature-based kinetic parameters for wood pyrolysis vary widely. They are usually measured at low to moderate temperature (usually < 900 K). No high-temperature kinetic data for the two-stage scheme have been reported. Font et al. (Font et al., 1990) presented kinetic data for the three primary reactions that are found to be comparable to what Nunn et al. (Nunn et al., 1985) reported for the single reaction kinetic data for hardwood in the high-temperature range (573 ~ 1373 K). Font et al.'s results are used in this model for sawdust samples and Wagenaar's (Wagenaar et al., 1993) pine wood pyrolysis kinetics data are applied for poplar samples. The pre-exponential factors, activation energy, and standard heats of reaction for all the reactions used in this model appear in Table 12.

Table 12 Kinetic data and heats of reaction *

Reaction index	A (1/s)	E (KJ/mol)	Reference	Temperature range (K)	ΔH (KJ/kg)	Reference
1 (hardwood sawdust)	1.52×10^{7}	139.2	(Font et al., 1990)	733-878	-418	(Chan et al., 1985)
1 (poplar)	1.11×10^{11}	177	(Wagenaar et al., 1993)	573-873		
2 (hardwood sawdust)	5.85×10^{6}	119	(Font et al., 1990)	733-878	-418	(Chan et al., 1985)
2 (poplar)	9.28×10^{9}	149	(Wagenaar et al., 1993)	573-873		
3 (hardwood sawdust)	2.98×10^{3}	73.1	(Font et al., 1990)	733-878	-418	(Chan et al., 1985)
3 (poplar)	3.05×10^{7}	125	(Wagenaar et al., 1993)	573-873		
4	4.28×10^{6}	107.5	(Liden et al., 1988)	-	42	(Koufopanos et al., 1991)
5	1.0×10^{5}	107.5	(Di Blasi, 1993)	-	42	(Koufopanos et al., 1991)
6	5.13×10^{10}	88	(Bryden and Hagge, 2003)	-	-2,440	(Bryden and Hagge, 2003)

(Table 12 continued)

8	0.658 (m/s.K)	74.8	(Evans and Emmons, 1977)	-	9,212	(Bryden and Hagge, 2003)
9	3.42 (m/s.K)	130	(Brewster et al., 1993)	-	14,370	(Turns, 2000)
10	3.42 (m/s.K)	130	(Brewster et al., 1993)	-	10,940	(Turns, 2000)
11	**$10^{12.35}$**	**167**	**(Hautman et al., 1981)**	**-**	**10,110**	**(Turns, 2000)**
12	$10^{12.71}$	171.3	(Hautman et al., 1981)	-	120,900	(Turns, 2000)
13	$10^{4.32}\times T\times P^{0.3}$	80.2	(Smoot and Smith, 1985)	-	41,600	(Bryden, 1998)

*: These are all 1-step kinetics for pyrolysis.

5.2. Heat, Mass, and Momentum Transfer

The following assumptions allow tractable mathematical combustion model development:

- all properties are assumed to be transient and one dimensional in space;
- local thermal equilibrium exists between the solid and gas phase in the particle, so internal temperatures and their gradients are the same for the solid and gas;
- gases behave as ideal gases, including both relationships between pressure, temperature, and specific volume and dependence of heat capacity on temperature only;
- particle aspect ratios and shapes do not change during devolatilization, though size does change dynamically. The shape and aspect ratio is a simplifying assumption for this case but not required by the model in general;

- heat and mass transfer at particle boundaries increase relative to that of a sphere by the ratio of the particle surface to that of a volume-equivalent sphere – a close approximation to results from more detailed analyses for similarly sized particles.

In the particle model, the particle shapes are represented by a parameter n. A spherical particle is described by $n = 2$, cylinder particles by $n = 1$, and flat plate particles $n = 0$. Before the biomass particle enters the reactor, it is assumed that it is filled by inert gas or air. So in total twelve species appear in the model: biomass, char, free water, bound water, ash, CO, CO_2, H_2O, H_2, O_2, lumped hydrocarbon (tar), and inert gas. The mass conservation of each species, the momentum, and the total energy equations, as well as the initial and boundary conditions appear as Equations (22) - (59)

The biomass temporal mass balance contains three consumption terms, one each for the reactions to light gas, tar, and char, where all terms in this expression and most terms in subsequent expressions depend on both time and position.

$$\frac{\partial \rho_B}{\partial t} = S_B$$
$$where, S_B = -(r_1 + r_2 + r_3) \tag{22}$$

Similarly, the char temporal mass balance contains five source terms, one from the conversion of biomass to char and one for the char yield from the secondary reactions of tar, as well as the gasification and oxidation reactions.

$$\frac{\partial \rho_C}{\partial t} = S_C$$
$$where, S_C = r_3 + r_5 - r_8 \frac{2M_C}{M_{O_2}} - r_9 \frac{M_C}{M_{CO_2}} - r_{10} \frac{M_C}{M_{H_2O}} \tag{23}$$

The temporal free-water mass balance contains a loss associated with conversion to vapor and a source term associated with water vapor readsorption into the particle, as determined by r_6 in Table 11. The free water also migrates due to the pressure gradient in the liquid phase (De Paiva Souza and Nebra, 2000; Ouelhazi et al., 1992). The migration flux is based on Darcy's law for this porous media, which is proportional to the total liquid pressure gradient. The total liquid pressure is equal to the pressure of the gas phase minus the capillary pressure of the gas-liquid interface. An effective free water diffusivity $D_{eff,fw}$ is derived to describe the migration with Fick's law applied based on the Darcy's law results (De Paiva Souza and Nebra, 2000). Equation (24) gives the mass balance for free water. The mass transfer coefficient of vapor in the pore $h_{m,pore}$, which appears in the evaporation rate r_6, is determined by Equation (25) (Incropera and Dewitt, 1996).

$$\frac{\partial \rho_{fw}}{\partial t} = \frac{1}{r^n}\frac{\partial}{\partial r}\left(r^n D_{eff,fw}\frac{\partial \rho_{fw}}{\partial r}\right) + S_{fw}, \quad (24)$$
$$where, S_{fw} = -r_6,$$

$$h_{m,pore} = 3.66 \cdot \frac{D_{eff,H_2O}}{d_{pore\_hydraulic}} \quad (25)$$

Bound water has similar migration in the radial direction but it is driven by a chemical potential gradient, and the phase change rate is described by the chemical reaction r_7, shown in Equation (26).

$$\frac{\partial \rho_{bw}}{\partial t} = \frac{1}{r^n}\frac{\partial}{\partial r}\left(r^n D_{eff,bw}\frac{\partial \rho_{bw}}{\partial r}\right) + S_{bw} \quad (26)$$
$$where, S_{bw} = -r_7,$$

Several different correlations describe diffusivities of free water and bound water (De Paiva Souza and Nebra, 2000; Olek et al., 2005; Ouelhazi et al., 1992), and Olek et.

al.'s method is applied in this investigation. It is also believed that the diffusivities of both free water and bound water are direction dependent, and the diffusivity in the axial direction is larger than that in the tangential direction. Details can be found at the end of this section in the physical property list.

The ash in the particle is assumed to be inert, so that the ash density is constant,

$$\frac{\partial \rho_A}{\partial t} = 0 . \tag{27}$$

The conservation equations for all gas-phase components (CO, CO_2, H_2O, O_2, H_2, HC, and inert gas) include temporal and spatial gradients, convection, and source terms and can be written as follows:

$$\frac{\partial}{\partial t}\varepsilon\rho_g Y_i + \frac{1}{r^n}\frac{\partial}{\partial r}(r^n \varepsilon \rho_g Y_i u) = \frac{1}{r^n}\frac{\partial}{\partial r}(r^n \varepsilon D_{eff,i}\rho_g \frac{\partial Y_i}{\partial r}) + S_i . \tag{28}$$

Source terms for each gas-phase species appear below:

$$\begin{aligned}
S_{CO_2} &= r_{11}\frac{M_{CO_2}}{M_{CO}} - r_9 + (r_1 + r_4)\alpha_{CO_2} \\
S_{CO} &= r_8\frac{2M_{C0}}{M_{O_2}} + r_9\frac{2M_{CO}}{M_{CO_2}} + r_{10}\frac{M_{CO}}{M_{H_2O}} + r_{13}\frac{6M_{CO}}{M_{HC}} - r_{11} + (r_1 + r_4)\alpha_{CO} \\
S_{O_2} &= -r_8 - r_{11}\frac{M_{O_2}}{2M_{CO}} - r_{12}\frac{M_{O_2}}{2M_{H_2}} - r_{13}\frac{2.9M_{O_2}}{M_{HC}} \\
S_{H_2} &= (r_1 + r_4)\alpha_{H_2} + r_{10}\frac{M_{H_2}}{M_{H_2O}} - r_{12} + r_{13}\frac{3.1M_{H_2}}{M_{HC}} \\
S_{H_2O} &= (r_1 + r_4)\alpha_{H_2O} + r_6 + r_7 - r_{10} + r_{12}\frac{M_{H_2O}}{M_{H_2}} \\
S_{HC} &= r_2 + (r_1 + r_4)\alpha_{HC} - r_4 - r_5 - r_{13} \\
S_I &= 0
\end{aligned} \tag{29}$$

The overall gas-phase continuity equation results from the sum of these species and has the form

$$\frac{\partial}{\partial t}\varepsilon\rho_g + \frac{1}{r^n}\frac{\partial}{\partial r}(r^n \varepsilon\rho_g u) = S_g,$$
$$where, S_g = r_1 + r_2 - r_5 + r_6 + r_7 + r_8\frac{2M_C}{M_{O_2}} + r_9\frac{M_C}{M_{CO_2}} + r_9\frac{M_C}{M_{H_2O}}. \quad (30)$$

The gas-phase velocity in the particle obeys a Darcy-law-type expression

$$u = -\frac{\eta}{\mu}\frac{\partial p}{\partial r},$$
$$where, p = \frac{\rho_g R_g T}{M_W}. \quad (31)$$

The gas mixture is treated as ideal gas, and the average molecular weight is

$$M_W = \sum_j X_j \cdot M_j , \quad (32)$$

where the mole fraction of each gas species, X_j, is equal to

$$X_j = \frac{\left(\frac{Y_j}{M_j}\right)}{\left(\sum_i \frac{Y_i}{M_i}\right)}. \quad (33)$$

The permeability, η, is expressed as a mass-weighted function of the individual solid-phase permeabilities:

$$\eta = \frac{\rho_B}{\rho_{B,0}}\eta_B + \left(1 - \frac{\rho_B}{\rho_{B,0}}\right)\eta_C \quad (34)$$

The energy conservation equation includes the following terms:

$$\frac{\partial}{\partial t}\left[\sum_i \rho_i \hat{H}_i + \sum_k \rho_k \hat{H}_k + \varepsilon \rho_g \sum_j Y_j \hat{H}_j\right] + \frac{1}{r^n}\frac{\partial}{\partial r}\left[r^n \varepsilon \rho_g u \sum_j Y_j \hat{H}_j\right]$$
$$= \frac{1}{r^n}\frac{\partial}{\partial r}(r^n K_{eff}\frac{\partial T}{\partial r}) + \frac{1}{r^n}\frac{\partial}{\partial r}\left[r^n\left(\rho_g \varepsilon \sum_j D_{eff,j}\frac{\partial Y_j}{\partial r}\hat{H}_j + D_{eff,k}\frac{\partial \rho_k}{\partial r}\hat{H}_k\right)\right], \quad (35)$$

where,

$\hat{H}_l = \hat{H}^0_{l,f} + \int_{T_0}^{T} C_{p,l}(T)dT$, l is any species involved,

i = any species or component in the solid phase,

j = any species or component in the gas phase,

k = free water and bound water.

This form of the energy equation relates to standard theoretical analyses (Bird et al., 2002) for multi-components systems. In Equation (35), the first term represents the energy accumulation; the second term represents energy convection; the third term (first term after the equals sign) accounts for conduction heat transfer, and the last term accounts for energy associated with diffusion of species in the gas phase and the liquid phase. The last term generally contributes only negligibly to the overall equations and is commonly justifiably ignored. No heats of reaction appear in the expression since the energy balances total enthalpy (both phases) and is not written in terms of temperature or separate particle and gas phases. Heats of reaction only become apparent when separately modeling the particle and gas phases or using temperature instead of enthalpy. Radiation between the gas and solid phase in the particle is incorporated into the effective conductivity, as explained below.

The effective diffusivity of gas species in the particle can be calculated by the parallel pore (Wheeler) model, as shown in Equation (36).

$$D_{eff} = D\varepsilon/\tau$$
$$\text{where, } 1/D = 1/D_{AB} + 1/D_K \tag{36}$$

An identical diffusivity for each species and Fickian diffusion assumptions, as implied here, avoid the complexity of more formal multi-component diffusion calculations.

The effective particle thermal conductivity includes radiative and conductive components with some theoretical basis (Robinson et al., 2001a; Robinson et al., 2001b) and with empirical verification for wood (Janse et al., 2000).

$$K_{eff} = K_{cond} + K_{rad}, \tag{37}$$

where the particle structure is assumed to be close to the upper limit for thermal conductivity, that is, it is assumed to have high connectivity in the direction of conduction,

$$K_{cond} = \varepsilon K_{gas} + (1-\varepsilon)\left[\frac{\rho_B}{\rho_{B,0}}K_B + \left(1-\frac{\rho_B}{\rho_{B,0}}\right)K_C\right],$$
$$K_{gas} = \sum_j Y_j K_j \tag{38}$$

and where radiation contributes approximately to the third power of the temperature

$$K_{rad} = \frac{\varepsilon\sigma T^3 d_{pore}}{\omega}. \tag{39}$$

The emissivity of the particle is the mass-weighted result of each solid component: biomass, ash, and char. A volume-weighted emissivity might be more appropriate, but

it's not available in this case: all components are assumed to occupy the same total volume.

$$\omega = \frac{\rho_A}{\sum \rho_i}\omega_A + \frac{\rho_B}{\sum \rho_i}\omega_B + \frac{\rho_C}{\sum \rho_i}\omega_C \tag{40}$$

The thermal conductivity of wet biomass particle is based on Ouelhazi's (Ouelhazi et al., 1992) empirical correlation which states that the effective thermal conductivity is a function of temperature and moisture contents. Thermal conductivity in the axial direction is assumed to be 2.5 times that in the tangential direction. An average value of both the axial and tangential directions is adopted in this paper. Details of the thermal conductivity of the wet biomass particle appear at the end of this section.

Initial conditions are assumed from experimental conditions for a non-reacting particle. That is, at $t = 0$,

$$\begin{aligned} &p(t=0,r) = p_{atm} \\ &T(t=0,r) = 300K\,(typically) \\ &u(t=0,r) = 0 \\ &Y_l(t=0,r) = 1 \\ &Y_{i(j,k)}(t=0,r) = 0 \end{aligned} \quad . \tag{41}$$

Boundary conditions at the particle center are determined by symmetry, i.e., at $r = 0$,

$$\begin{aligned} &\left.\frac{\partial p}{\partial r}\right|_{t,r=0} = 0, \\ &u\big|_{t,r=0} = 0, \\ &\left.\frac{\partial T}{\partial r}\right|_{t,r=0} = 0, \\ &\left.\frac{\partial Y_{i(j,k)}}{\partial r}\right|_{t,r=0} = 0. \end{aligned} \tag{42}$$

During biomass particle combustion, the flame surrounding the particle may affect particle surface temperature by heat generated in the flame that feeds back to the surface and further heats the particle. The model is capable of modeling both the particle domain and the boundary layer domain, which is assumed to include the flame during combustion. The boundary layer flame simulation, as with many other model features, can be turned on or off during simulation.

If the boundary layer domain is off, boundary conditions at the particle outer surface are defined by external conditions of pressure and heat and mass flux:

$$\begin{aligned} &p(t, r = r_p) = p_{atm}, \\ &\left.\frac{\partial Y_{i(j,k)}}{\partial r}\right|_{r=r_p} = \theta_m h_m R_{SA}\left(Y_{i(j,k),\infty} - Y_{i(j,k),S}\right) \\ &\left.k_{eff}\frac{\partial T}{\partial r}\right|_{r=r_p} = \theta_T h_T R_{SA}\left(T_f - T\right) + R_{SA}\omega\sigma\left(T_w{}^4 - T^4\right) \end{aligned} \quad , \tag{43}$$

where θ_m and θ_T represent the blowing factors (Bird et al., 2002) for mass transfer and heat transfer, respectively. R_{SA} represents the exterior surface area ratio, which is the surface area of the particle divided by the characteristic surface area as follows:

$$\begin{aligned} &R_{SA} = SA/(4\pi R_P{}^2)\ , \\ &R_{SA} = SA/(4\pi R_P{}^2 AR), \\ &R_{SA} = SA/(4R_P{}^2 AR^2), \end{aligned} \tag{44}$$

for spheres, cylinders, and flat plates, respectively.

Each shape employs heat transfer coefficients developed for that particular shape. Correlations suitable for random particle orientation during flight appear in the literature for some particles (Masliyah and Epstein, 1972). Where such a model is not available, the

characteristic length of the particle is calculated using the average length of the particle. For near-spherical particles, Masliyah's prolate spheroid model (Masliyah and Epstein, 1972) provides a suitable correlation, as indicated in Equation (45).

$$Nu = 1.05 + 0.6\,\mathrm{Re}^{0.65}\,\mathrm{Pr}^{0.33} \tag{45}$$

Cylinders at low Reynolds numbers adopt the correlation of Kurdyumov (Kurdyumov and Fernandez, 1998) (Equation (46)).

$$Nu = W_0(\mathrm{Re})\mathrm{Pr}^{0.33} + W_1(\mathrm{Re}), \tag{46}$$

where,

$$W_0 = \begin{cases} 0.46271\exp\left(1.01633\left(\log_{10}(\mathrm{Re})\right) + 0.05121\left(\log_{10}(\mathrm{Re})\right)^2\right), & 10^{-2} \le \mathrm{Re} \le 3.14, \\ 0.597\left(\mathrm{Re}/\ln\left(1/\mathrm{Re}\right)\right)^{1/3}, & \mathrm{Re} < 10^{-2}, \end{cases}$$

$$W_1 = \begin{cases} 0.10666\exp\begin{pmatrix} 0.41285\left(\log_{10}\mathrm{Re}\right) + 0.43847\left(\log_{10}\mathrm{Re}\right)^2 + 0.1915\left(\log_{10}\mathrm{Re}\right)^3 \\ +0.01802\left(\log_{10}\mathrm{Re}\right)^4 - 0.005225\left(\log_{10}\mathrm{Re}\right)^5 \end{pmatrix} \\ 0.0917, \quad \mathrm{Re} < 10^{-2}. \end{cases}$$

The heat transfer coefficient for a flat plate appears in Equation (47).

$$Nu = 0.644\,\mathrm{Re}^{0.5}\,\mathrm{Pr}^{0.343} \tag{47}$$

Mass transfer coefficient calculations are analogous to heat transfer correlations respectively for each specific particle shape.

If the boundary layer domain is turned on, the boundary conditions assume those in the bulk flow (indicated by infinity subscripts), as shown in Equation (48).

$$p\big|_{r>=r_p} = p_{atm},$$
$$Y_{i(j,k)}\big|_{r=r_p+BLT_m} = Y_{i(j,k),\infty}, \tag{48}$$
$$T\big|_{r=r_p+BLT_T} = T_\infty$$

where, BLT_m and BLT_T are boundary layer thickness of mass transfer and heat transfer, respectively. The determination of these two types of boundary layer thicknesses is straightforward if the particle stays in inert carrier gas (nitrogen). Two methods can be adopted to calculate the thickness: linear and exponential. Figure 56 illustrates each assumption, where only mass-transfer-boundary-layer thickness is indicated. The heat-transfer-boundary-layer thickness has a similar form.

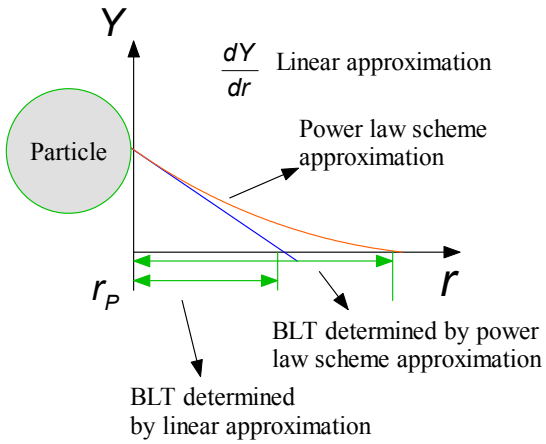

Figure 56 Boundary layer thickness determination

The linear approximation assumes that the gradient at the particle surface can be approximated by an algebraic difference:

$$\frac{dY}{dr} \approx \frac{\Delta Y}{\Delta r} = \frac{Y_\infty - Y_S}{BLT_m}. \tag{49}$$

The mass transfer at the particle surface is also correlated with the empirical mass transfer correlation:

$$D_{AB}\frac{dY}{dr} = h_m \theta_m \left(Y_\infty - Y_s\right), \tag{50}$$

where, the mass transfer coefficient can be calculated by

$$Sh = \frac{d_P h_m}{D_{AB}}. \tag{51}$$

So, substituting Equations (50) and (51) into Equation (49) leads to the boundary layer thickness for mass transfer:

$$BLT_m = \frac{d_P}{Sh \cdot \theta_m}. \tag{52}$$

Similarly, the boundary layer thickness of heat transfer based on the linear approximation is

$$BLT_T = \frac{d_P}{Nu \cdot \theta_T}. \tag{53}$$

The exponential scheme (Roberts, 2005) for boundary layer thickness calculation is based on a more exact solution for a convection-diffusion partial differential equation explained by Patankar (Patankar, 1980). The exact solution better approximates the distribution in the boundary layer for any variable compared to the linear approximation, as shown in Figure 56. The exact solution of a steady one-dimensional convection and diffusion problem in Cartesian coordinates is

$$\frac{\phi-\phi_0}{\phi_L-\phi_0}=\frac{\exp(Px/L)-1}{\exp(P)-1}$$
$$\text{Peclet n umber } P=\frac{\rho uL}{\Gamma}, \tag{54}$$

where *0-L* defines the boundary layer domain with *0* as the particle surface and *L* the infinity boundary. The derivative of φ at the particle surface with respect to x according to the above equation will be

$$\left.\frac{d\phi}{dx}\right|_{x=0}=\frac{(\phi_L-\phi_0)}{\exp(P)-1}\cdot\frac{P}{L}=\frac{(\phi_L-\phi_0)}{\exp(P)-1}\cdot\frac{\rho u}{\Gamma}. \tag{55}$$

Substituting the mass transfer correlation, Equation (50), into the above equation results in the boundary layer thickness

$$BLT_m=\frac{\Gamma}{\rho u}\ln\left(\frac{\rho u}{h_m\theta_m}+1\right). \tag{56}$$

For any coordinate system, if both the strengths of convection and diffusion ($\rho u r^n$ and $\rho D_{AB} r^n$) are assumed be to constant, the boundary layer thickness for mass transfer appears in Equation (57).

$$BLT_m=\frac{\rho D_{AB} r^n}{\rho u r^n}\ln\left(\frac{\rho u r^n}{\rho D_{AB} r^n h_m\theta_m}D_{AB,x=0}+1\right) \tag{57}$$

Similarly, the heat-transfer-boundary-layer thickness has the same formula as the mass-transfer-related parameters in Equation (57) replaced by heat-transfer-relevant parameters:

$$BLT_T=\frac{kr^n}{\rho Cpur^n}\ln\left(\frac{\rho Cpur^n}{kr^n h_T\theta_T}k_{x=0}+1\right). \tag{58}$$

When the particle is surrounded by air instead nitrogen, a flame forms in the boundary layer. The resulting temperature and species concentration distributions in the boundary layer may influence the boundary layer thickness, making it different from that calculated based on the heat and mass transfer correlations illustrated above. The determination of the exact boundary layer thickness for such a burning particle with surrounding flame could be complicated due to bulk flow convection (slip velocity) in the reactor axial direction and the offgases from the particle. A two-dimensional model might be needed to predict the exact boundary layer thickness. In this investigation, Equations (57) and (58) are applied to determine the thickness of the boundary layer, where flame is formed during combustion. Model predictions agree with experimental data well.

To simplify momentum conservation, constant boundary-layer pressure is assumed, equal to the atmospheric pressure. The secondary cracking reactions of tar and soot formation in the boundary layer are neglected, although combustion reactions are included. A radiation energy flux has to be added to the energy equation for the node on the particle physical surface due to the radiation between the particle surface and reactor wall.

Particle shrinking or swelling during drying, pyrolysis, and char gasification and oxidation is described and modeled using the following empirical correlation:

$$\frac{v}{v^0} = 1 + x_M(\beta_M - 1.0) + x_B(\beta_B - 1.0) + x_C(\beta_C - 1.0), \qquad (59)$$

which can be used to describe both shrinking and swelling behaviors of a burning solid particle or droplet. In Equation , v = current control volume of each cell, v^0 = initial control volume of each cell; x_m, x_B, x_C =conversion of moisture, biomass, and char;

β_M =swelling/shrinking factor of moisture drying, 3.65 for black liquor swelling and 0.9 for wood particle drying shrinking; β_B =swelling/shrinking factor of biomass devolatilization, 30.0 for black liquor swelling and 0.9 for wood particle shrinking; β_C =shrinking factor of char burning, 0.0 for constant char density shrinking (conceptually consistent with the typically external diffusion controlled oxidation rates).

The physical properties of the biomass particles significantly affect the heat and mass transfer rates (Di Blasi, 1997; Raveendran et al., 1995). In this work, temperature-dependent heat capacity correlations are used for all species. The heat capacity of biomass and char adopt the model suggested by Merrick (Merrick, 1983). Gronli et al. (Gronli and Melaaen, 2000) suggested a correlation for tar heat capacity, which is based on some typical pyrolysis tar components (closely related to benzene). All physical properties appear in Table 13.

Table 13 Physical properties of biomass particles

Property	Value	Reference
Wood density ρ_B	650 kg/m^3 (sawdust) 580 kg/m^3 (poplar particle)	
Porosity ε	0.4	
Emissivity ω	ω_A=0.7 ω_B=0.85 ω_C=0.95	
Permeability η (Darcy)	η_B = 1 η_C = 100	(Gronli and Melaaen, 2000)

(Table 13 continued)

Thermal conductivity K (W/m.K)	k_j, gas species thermal conductivity is calculated based on DIPPR correlations	(DIPPR)
	$K_A = 1.2$	
	Wet biomass in tangential direction: if $C_w > 0.4$: $k_B = \left(9.32\times10^{-2} + 6.5\times10^{-3}C_w\right)$ $\left(1+3.65\times10^{-3}\left(T-273.15\right)\right)\left(0.986+2.695C_w\right)$ if $C_w \le 0.4$: $k_B = \left(0.129 - 4.9\times10^{-2}C_w\right)$ $\left(1+(2.05+4C_w)\times10^{-3}\left(T-273.15\right)\right)\left(0.986+2.695C_w\right)$ Thermal conductivity in axial direction is 2.5 times of the tangential one.	(Ouelhazi et al., 1992)
	$K_C = 0.071$	(Lee et al., 1976)
Biomass particle specific surface area S_a, (m^2/m^3)	9.04×10^4	BET
Char particle specific surface area $S_{a,char}$, (m^2/m^3)	1.0×10^6	BET
Pore size $d_{pore,\,(m)}$	3.2×10^{-6}	BET
Hydraulic pore diameter, $d_{pore,hydraulic}$	$d_{pore,hydraulic} = \dfrac{4.0\varepsilon}{S_a\left(1.0-\varepsilon\right)}$	
Molecular weight M *(kg/kmol)*	$M_T = 145$	(Janse et al., 2000)
Viscosity μ, (Pa.s)	$\mu_{gas} = 3\times10^{-5}$ for all gas species	(Kansa et al., 1977)
Diffusivity D_{AB} (m^2/s)	$D_{AB} = 3.0\times10^{-5}$ for all gas species	(Janse et al., 2000)

(Table 13 continued)

	$D_{eff,bw} = D_0 \exp(\frac{-E_b}{R \cdot T})$ $E_b = a_1 - a_2 \cdot C_{bw}$ where, C_{bw} is bound water content, $D_0 = 5 \times 10^{-5} m/s$ $a_1 = 31030 J/mol$ $a_2 = 10000 J/mol$	(Olek et al., 2005)
	$D_{eff,fw} = 6.1 \times 10^{3} \left(\frac{k_{fw}}{\eta_{fw}}\right) \varepsilon^{0.61} \left(\frac{\rho_s C_{fw}}{\rho_{fw}}\right)$ *where*, $k_{fw} = \begin{cases} 0, \text{if } \left(\frac{\rho_s C_{fw}}{\varepsilon \rho_{fw}}\right) \le S_{ir} \\ k_{fw}^{\Phi} \left(1 - \cos \frac{\pi}{2} \left(\frac{(\rho_s C_{fw} / \varepsilon \rho_{fw}) - S_{ir}}{1 - S_{ir}}\right)\right) \\ \text{if } \left(\frac{\rho_s C_{fw}}{\varepsilon \rho_{fw}}\right) > S_{ir} \end{cases}$ $S_{ir} = 0.1, \text{irreducibl e saturation}$ $k_{fw}^{\Phi} = 3.0 \times 10^{-15} m^2$	(De Paiva Souza and Nebra, 2000)
Heat capacity C_p (J/kg.K)	$C_{p,B} = \left(\frac{1000 R_g}{7.72}\right)\left[g\left(\frac{380}{T}\right) + 2g\left(\frac{1800}{T}\right)\right]$	(Merrick, 1983)
	$C_{p,C} = \left(\frac{1000 R_g}{11.3}\right)\left[g\left(\frac{380}{T}\right) + 2g\left(\frac{1800}{T}\right)\right]$	(Merrick, 1983)
	Where, $g(x) = \frac{x^2 e^x}{(e^x - 1)^2}$	
	$C_{p,T} = -100 + 4.4 \times T - 0.00157 \times T^2$	(Gronli and Melaaen, 2000)
	$C_{p,j}$ of all gas species except hydrocarbon is based on DIPPR database correlations	(DIPPR)

5.3. Particle Differential Equations Solution Procedure

This one-dimensional complete mathematical model for the combustion of a single biomass particle includes a set of partial differential equations (PDEs) to describe the mass, heat, and momentum transfer in the particle domain and the flame layer domain. A control volume method (Patankar, 1980) reformulates these differential equations into a set of algebraic equations amenable to computer simulation. A fully implicit scheme is applied for the transient term in the energy conservation equation, each species conservation equation, and momentum equation; the convection and diffusion/conduction terms are solved by the power law scheme; control volume faces occur midway between the grid points; a staggered grid is used for velocity component; the SIMPLE algorithm is applied for the momentum transfer to calculate the flow field.

5.3.1. Standard Solution for the General Differential Equation

This set of partial differential equations for heat, mass, and momentum transfer can all be presented by a standard general equation. If the dependent variable is denoted by φ, the general partial differential equation is

$$\frac{\partial}{\partial t}\left(\varepsilon\rho\Phi\right) + div\left(\varepsilon\rho u\Phi\right) = div\left(\Gamma grad\Phi\right) + S\,, \tag{60}$$

where, $S = S_c + S_p\Phi$.

The calculation domain, including the particle and the boundary layer, is divided into a number of non-overlapping control volumes such that there is one control volume surrounding each grid point, as shown in Figure 57. The differential equation is integrated over each control volume. Piecewise profiles expressing the variation of φ

between the grid points are used to evaluate the required integrals. The result is the discretization equation containing the values of φ for a group of grid points.

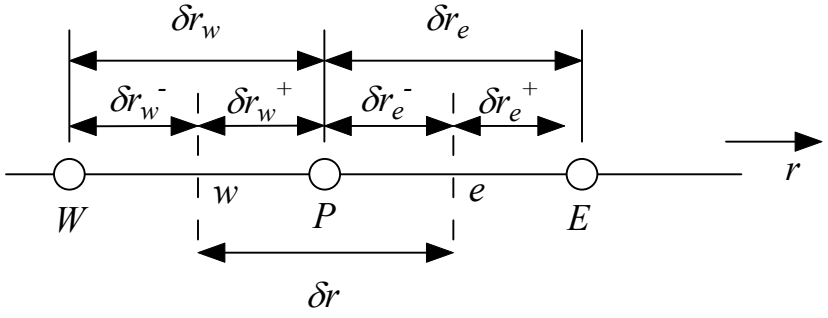

Figure 57 Grid-point cluster for one-dimensional problem

In Figure 57, point *P* is the current grid, and points *W* and *E* are the west neighbor point and the east neighbor point respectively for this one-dimensional problem. Faces *w* and *e* define the control volume surrounding the current grid point *P*. The integration form of the general equation with respect of time and the control volume is

$$\int_{dv}\int_{dt}\frac{\partial}{\partial t}(\varepsilon\rho\Phi)dtdv+\int_{dv}\int_{dt}div(\varepsilon\rho u\Phi)dtdv=\int_{dv}\int_{dt}div(\Gamma grad\Phi)dtdv+\int_{dv}\int_{dt}Sdtdv\,. \tag{61}$$

The general discretization equation is now derived through the integration for the one-dimensional problem with shrinking/swelling included:

$$a_P\Phi_P=a_W\Phi_W+a_E\Phi_E+b\,, \tag{62}$$

$$a_E=D_eA(|P_e|)+\max(-F_e,0), \tag{63}$$

$$a_W=D_wA(|P_w|)+\max(F_w,0), \tag{64}$$

where,

$$A(|P|) = \max\left(0, (1 - 0.1|P|)^5\right), \tag{65}$$

$$b = a_P^0 \Phi_P^0 + \Delta v S_C, \tag{66}$$

$$a_P = a_P^1 + a_W + a_E - \Delta v S_P + (F_e - F_w). \tag{67}$$

This general discretization equation is similar to that described in Patankar's (Patankar, 1980) analysis, with two differences: in this case, (1) the control volume shrinks/swells during combustion; (2) the continuity equation has a non-zero source term which is caused by mass change between different phases due to moisture evaporation/vapor recondensation, biomass pyrolysis/tar cracking, and char surface heterogeneous reactions.

With the general discretization equation established for each grid point in the calculation domain, a set of linear algebraic equations results. The solution of the discretization equations for this one-dimensional situation can be obtained by the standard Gaussian-elimination method, although in this case the matrix representation is tridiagonal, allowing the much more efficient TriDiagonal-Matrix Algorithm (TDMA) or Thomas algorithm. The detail process of the TDMA solution procedure is explained in (Patankar, 1980).

Specific definitions of F_e, F_w, D_e, D_w, , P_e, P_w, a_P^0, a_P^1, S_C, *and* S_P are variable dependent, i.e., they are different for each species mass conservation and energy conservation equations, and the details are illustrated in the following sections.

5.3.2. Solution of Solid Species Conservation Equations

Solid species, including biomass, char, and ash, don't have convection and diffusion in the radial direction, so that

$$F_e = F_w = D_e = D_w = a_W = a_E = 0, \tag{68}$$

$$a_P^0 = \frac{\Delta v^0}{\Delta t}, \qquad a_P^1 = \frac{\Delta v}{\Delta t}, \tag{69}$$

$$\Delta v^0 = \frac{{r_e^0}^{n+1} - {r_w^0}^{n+1}}{n+1}, \qquad \Delta v = \frac{{r_e}^{n+1} - {r_w}^{n+1}}{n+1}. \tag{70}$$

The source term of each solid species component is linearized as

Biomass:

$$S_C = 0,\ \mathrm{S_P} = -\left(k_1 + k_2 + k_3\right);$$

Char:

$$S_C = k_3\rho_B + k_5\varepsilon\rho_g Y_{HC},$$
$$\mathrm{S_P} = \frac{-s_{a,char}}{\rho_C^{*} + \rho_B + \rho_A}\left(k_8\varepsilon\rho_g Y_{O_2}\frac{2M_C}{M_{O_2}} + k_9\varepsilon\rho_g Y_{CO_2}\frac{M_C}{M_{CO_2}} + k_{10}\varepsilon\rho_g Y_V\frac{M_C}{M_V}\right); \tag{71}$$

Ash:

$$S_C = 0,\ \mathrm{S_P} = 0.$$

The density of biomass, char, and ash can be solved explicitly and TDMA is not needed.

5.3.3. Solution of Liquid Species Conservation Equations

The liquid species includes free water and bound water, which are assumed to migrate only through diffusion in the radial direction. Coefficients of the discretization equation are

$$F_e = F_w = P_e = P_w = 0, \tag{72}$$

$$a_P^0 = \frac{\Delta v^0}{\Delta t}, \qquad a_P^1 = \frac{\Delta v}{\Delta t}, \tag{73}$$

Free water ρ_{fw}:

$$\begin{aligned} D_e &= r_e^n \frac{D_{eff,fw,e}}{\delta r_e}, \qquad D_w = r_w^n \frac{D_{eff,fw,w}}{\delta r_w}; \\ S_C &= s_a \frac{\rho_{fw}^*}{\rho_{fw}^0} h_{m,pore} Y_V \rho_g \\ S_P &= -s_a \frac{1}{\rho_{fw}^0} h_{m,pore} \rho_v^{sat} \end{aligned} \tag{74}$$

Bound water ρ_{bw}:

$$\begin{aligned} D_e &= r_e^n \frac{D_{eff,bw,e}}{\delta r_e}, \qquad D_w = r_w^n \frac{D_{eff,bw,w}}{\delta r_w}. \\ S_C &= 0, \qquad S_P = -k_7 \end{aligned}$$

The resulted discretization equations are solved with the TDMA explained above.

5.3.4. Solution of Gas Species Conservation Equations

Both convection and diffusion contribute the mass transfer of each individual gas species. Coefficients for the discretization equation of each gas species are listed in detail as follows.

For any gas species *j*:

$$D_e = r_e^n \frac{\varepsilon \rho_{g,e} D_{eff,j,e}}{\delta r_e}, \qquad D_w = r_w^n \frac{\varepsilon \rho_{g,w} D_{eff,j,w}}{\delta r_w}, \tag{75}$$

$$F_e = r_e^n \varepsilon \rho_{g,e} u_e, \qquad F_w = r_w^n \varepsilon \rho_{g,w} u_w, \tag{76}$$

$$P_e = \frac{F_e}{D_e}, \qquad P_w = \frac{F_w}{D_w}, \tag{77}$$

$$a_P^0 = \frac{\varepsilon \rho_g^0 \Delta v^0}{\Delta t}, \qquad a_P^1 = \frac{\varepsilon \rho_g \Delta v}{\Delta t}. \tag{78}$$

Linearization of the source terms of each gas species:

Oxygen Y_{O2}:

$$\begin{aligned} S_C &= 0, \\ S_P &= -s_{a,char} \frac{\rho_C}{\rho_C + \rho_B + \rho_A} k_8 \varepsilon \rho_g \\ &- 0.5 M_{w,O_2} \varepsilon k_{11} 10^3 \left(\frac{\rho_g Y_{CO}}{10^3 M_{CO}} \right) \left(\frac{\rho_g}{10^3 M_{O_2}} \right)^{0.25} \left(\frac{\rho_g Y_V}{10^3 M_V} \right)^{0.5} Y_{O_2}^{*\,-0.75} \\ &- 0.5 M_{w,O_2} \varepsilon k_{12} 10^3 \left(\frac{\rho_g Y_{H_2}}{10^3 M_{w,H_2}} \right) \left(\frac{\rho_g}{10^3 M_{O_2}} \right)^{1.42} Y_{O_2}^{*\,0.42} \\ &- 2.9 \varepsilon k_{13} 10^3 M_{W,O_2} \left(\frac{\rho_g Y_T}{10^3 M_T} \right)^{0.5} \left(\frac{\rho_g}{10^3 M_{O_2}} \right) \end{aligned} \tag{79}$$

Carbon monoxide Y_{CO}:

$$\begin{aligned} S_C &= s_{a,char} \frac{\rho_C}{\rho_C + \rho_B + \rho_A} \left(k_8 \varepsilon \rho_g Y_{O_2} \frac{2M_{CO}}{M_{O_2}} + k_9 \varepsilon \rho_g Y_{CO_2} \frac{2M_{CO}}{M_{CO_2}} + k_8 \varepsilon \rho_g Y_V \frac{M_{CO}}{M_V} \right) \\ &+ \left(k_1 \rho_B + \varepsilon k_4 \rho_g Y_T \right) \alpha_{CO} + 6 \varepsilon k_{13} 10^3 M_{CO} \left(\frac{\rho_g Y_T}{10^3 M_T} \right)^{0.5} \left(\frac{\rho_g}{10^3 M_{O_2}} \right), \\ S_P &= -M_{CO} \varepsilon k_{11} 10^3 \left(\frac{\rho_g}{10^3 M_{CO}} \right) \left(\frac{\rho_g Y_{O_2}}{10^3 M_{O_2}} \right)^{0.25} \left(\frac{\rho_g Y_V}{10^3 M_V} \right)^{0.5} \end{aligned} \tag{80}$$

Carbon dioxide Y_{CO2}:

$$S_C = \left(k_1\rho_B + \varepsilon k_4 \rho_g Y_T\right)\alpha_{CO_2} + M_{CO_2}\varepsilon k_{11} 10^3 \left(\frac{\rho_g Y_{CO}}{10^3 M_{CO}}\right)\left(\frac{\rho_g Y_{O_2}}{10^3 M_{O_2}}\right)^{0.25}\left(\frac{\rho_g Y_V}{10^3 M_V}\right)^{0.5},$$
$$S_P = -s_{a,char}\frac{\rho_C}{\rho_C + \rho_B + \rho_A} k_9 \varepsilon \rho_g \tag{81}$$

Hydrogen Y_{H2}:

$$S_C = \left(k_1\rho_B + \varepsilon k_4 \rho_g Y_T\right)\alpha_{H_2} + s_{a,char}\frac{M_{H_2}}{M_V}\frac{\rho_C}{\rho_C + \rho_B + \rho_A} k_{10}\varepsilon\rho_g Y_V$$
$$+ 3.1\varepsilon k_{13} 10^3 M_{H_2}\left(\frac{\rho_g Y_T}{10^3 M_T}\right)\left(\frac{\rho_g Y_{O_2}}{10^3 M_{O_2}}\right)^{0.5}, \tag{82}$$
$$S_P = -\varepsilon k_{12} 10^3 M_{H_2}\left(\frac{\rho_g}{10^3 M_{H_2}}\right)\left(\frac{\rho_g Y_{O_2}}{10^3 M_{O_2}}\right)^{1.42}$$

Vapor Y_{H2O}:

$$S_C = \left(k_1\rho_B + \varepsilon k_4 \rho_g Y_T\right)\alpha_V + s_a\frac{\rho_{fw}}{\rho_{fw}^0} h_{m,pore}\rho_v^{sat} + k_7\rho_{bw}$$
$$+ M_{H_2O}\varepsilon k_{12} 10^3 \left(\frac{\rho_g Y_{H_2}}{10^3 M_{H_2}}\right)\left(\frac{\rho_g Y_{O_2}}{10^3 M_{O_2}}\right)^{1.42}, \tag{83}$$
$$S_P = -s_{a,char}\frac{\rho_C}{\rho_C + \rho_B + \rho_A} k_{10}\varepsilon\rho_g - s_a\frac{\rho_{fw}}{\rho_{fw}^0} h_{m,pore}\rho_g$$

Carbon dioxide Y_{HC}:

$$S_C = k_1\rho_B\alpha_{HC} + k_2\rho_B,$$
$$S_P = -\varepsilon k_4\rho_g\left(1-\alpha_{HC}\right) - \varepsilon k_5\rho_g - \varepsilon k_{13} 10^3 M_T\left(\frac{\rho_g}{10^3 M_T}\right)^{0.5}\left(\frac{\rho_{O_2}}{10^3 M_{O_2}}\right)Y_T^{*-0.5} \tag{84}$$

Inert gas Y_I:

$$S_C = 0, \qquad S_P = 0 \tag{85}$$

5.3.5. Solution of Energy Conservation Equation

The energy conservation equation contains both enthalpy and temperature as the dependent variables. In the solid domain, the total enthalpy includes enthalpy of solid species, liquid species, and gas species, but only gas species enthalpy appears in the convection term. In addition, solid species enthalpy does not appear in the diffusion term. So temperature is chosen as the dependent variable for the energy conservation equation.

The original energy conservation equation is transformed so that it can be discretized by the control-volume method and solved by the standard TDMA.

Substituting the enthalpy expression of each species or component into Equation (35) results in Equation (86).

$$
\begin{aligned}
&\sum_i \hat{H}^0_{i,f}\frac{\partial \rho_i}{\partial t}+\sum_k \hat{H}^0_{k,f}\frac{\partial \rho_k}{\partial t}+\sum_j \hat{H}^0_{j,f}\frac{\partial}{\partial t}\left(\rho_g \varepsilon Y_j\right)\\
&+\frac{\partial}{\partial t}\left(\sum_i \rho_i\int_{T_0}^{T} C_{p,i}dT+\sum_k \rho_k\int_{T_0}^{T} C_{p,k}dT+\rho_g\varepsilon\sum_j Y_j\int_{T_0}^{T} C_{p,j}dT\right)\\
&+\sum_j \hat{H}^0_{j,f}\frac{1}{r^n}\frac{\partial}{\partial r}\left[r^n\varepsilon\rho_g u Y_j\right]+\frac{1}{r^n}\frac{\partial}{\partial r}\left[r^n\varepsilon\rho_g u\sum_j Y_j\int_{T_0}^{T} C_{p,j}dT\right]=\frac{1}{r^n}\frac{\partial}{\partial r}\left(r^n K_{eff}\frac{\partial T}{\partial r}\right)\\
&+\sum_j \hat{H}^0_{j,f}\frac{1}{r^n}\frac{\partial}{\partial r}\left(r^n\rho_g\varepsilon\sum_j D_{eff,j}\frac{\partial Y_j}{\partial r}\right)+\sum_k \hat{H}^0_{k,f}\frac{1}{r^n}\frac{\partial}{\partial r}\left(r^n\sum_k D_{eff,k}\frac{\partial \rho_k}{\partial r}\right)\\
&+\frac{1}{r^n}\frac{\partial}{\partial r}\left[r^n\left(\rho_g\varepsilon\sum_j D_{eff,j}\frac{\partial Y_j}{\partial r}\int_{T_0}^{T} C_{p,j}dT+\sum_k D_{eff,k}\frac{\partial \rho_k}{\partial r}\int_{T_0}^{T} C_{p,k}dT\right)\right]
\end{aligned}
\qquad (86)
$$

The heat of formation of each species at standard state is independent of temperature and any other variable. Multiplying the heat of formation at standard state by both the left and right side of each of the species conservation Equations (22) ~ (28) respectively, and substituting them back into Equation (86), results in the following:

$$\sum_i \hat{H}^0_{i,f} S_i + \sum_k \hat{H}^0_{k,f} S_k + \sum_j \hat{H}^0_{j,f} S_j$$
$$+\frac{\partial}{\partial t}\left(\sum_i \rho_i \int_{T_0}^{T} C_{p,i} dT + \sum_k \rho_k \int_{T_0}^{T} C_{p,k} dT + \rho_g \varepsilon \sum_j Y_j \int_{T_0}^{T} C_{p,j} dT \right)$$
$$+\frac{1}{r^n}\frac{\partial}{\partial r}\left[r^n \varepsilon \rho_g u \sum_j Y_j \int_{T_0}^{T} C_{p,j} dT \right] = \frac{1}{r^n}\frac{\partial}{\partial r}\left(r^n K_{eff} \frac{\partial T}{\partial r}\right) \qquad (87)$$
$$+\frac{1}{r^n}\frac{\partial}{\partial r}\left[r^n \left(\rho_g \varepsilon \sum_j D_{eff,j} \frac{\partial Y_j}{\partial r} \int_{T_0}^{T} C_{p,j} dT + \sum_k D_{eff,k} \frac{\partial \rho_k}{\partial r} \int_{T_0}^{T} C_{p,k} dT \right) \right]$$

The source term S of each species are explained earlier in this section. Substituting these source terms into the first three terms in Equation (87), the sum of the first three terms is obtained in Equation (88).

$$\sum_i \hat{H}^0_{i,f} S_i + \sum_k \hat{H}^0_{k,f} S_k + \sum_j \hat{H}^0_{j,f} S_j = -\sum_m r_m \Delta H^0_m$$
$$\text{where, } m \text{ is reaction index} = 1, ..., 13 \qquad (88)$$
$$\Delta H^0_m \text{ is the heat of reaction at standard state, which is the enthalpy of reactants substracts that of products}$$

So, Equation (87) becomes to Equation (89).

$$\frac{\partial}{\partial t}\left(\sum_i \rho_i \int_{T_0}^{T} C_{p,i} dT + \sum_k \rho_k \int_{T_0}^{T} C_{p,k} dT + \rho_g \varepsilon \sum_j Y_j \int_{T_0}^{T} C_{p,j} dT \right)$$
$$+\frac{1}{r^n}\frac{\partial}{\partial r}\left[r^n \varepsilon \rho_g u \sum_j Y_j \int_{T_0}^{T} C_{p,j} dT \right] = \frac{1}{r^n}\frac{\partial}{\partial r}\left(r^n K_{eff} \frac{\partial T}{\partial r}\right) + \sum_m r_m \Delta H^0_m \qquad (89)$$
$$+\frac{1}{r^n}\frac{\partial}{\partial r}\left[r^n \left(\rho_g \varepsilon \sum_j D_{eff,j} \frac{\partial Y_j}{\partial r} \int_{T_0}^{T} C_{p,j} dT + \sum_k D_{eff,k} \frac{\partial \rho_k}{\partial r} \int_{T_0}^{T} C_{p,k} dT \right) \right]$$

Now, the above equation needs to be transformed to a generalized form so that it can be solved using a control-volume method with respect to temperature. With the transformation described in Equation (90), the first two terms in Equation (89) can be expressed as Equation (91), and the third term as Equation (92).

$$\frac{\partial}{\partial t}\left(\rho_i \int_{T_0}^{T} C_{p,i} dT\right) = \rho_i \frac{\partial}{\partial t}\left(\int_{T_0}^{T} C_{p,i} dT\right) + \int_{T_0}^{T} C_{p,i} dT \frac{\partial \rho_i}{\partial t}$$
$$\frac{\partial}{\partial t}\left(\int_{T_0}^{T} C_{p,i} dT\right) = C_{p,i} \frac{\partial T}{\partial t}$$
$$\frac{\partial}{\partial t}\left(\rho_i C_{p,i} T\right) = \rho_i C_{p,i} \frac{\partial T}{\partial t} + T C_{p,i} \frac{\partial \rho_i}{\partial t} + T \rho_i \frac{\partial C_{p,i}}{\partial t} \tag{90}$$
$$\frac{\partial}{\partial t}\left(\rho_i \int_{T_0}^{T} C_{p,i} dT\right) = \rho_i C_{p,i} \frac{\partial T}{\partial t} + \int_{T_0}^{T} C_{p,i} dT \frac{\partial \rho_i}{\partial t}$$

$$\frac{\partial}{\partial t}\left(\rho_i \int_{T_0}^{T} C_{p,i} dT\right) = \frac{\partial}{\partial t}\left(\rho_i C_{p,i} T\right) + \left(\int_{T_0}^{T} C_{p,i} dT - T C_{p,i}\right) \frac{\partial \rho_i}{\partial t} - T \rho_i \frac{\partial C_{p,i}}{\partial t} \tag{91}$$

$$\frac{\partial}{\partial t}\left(\varepsilon \rho_j Y_j \int_{T_0}^{T} C_{p,j} dT\right) = \frac{\partial}{\partial t}\left(\varepsilon \rho_j Y_j C_{p,j} T\right) + \left(\int_{T_0}^{T} C_{p,j} dT - T C_{p,j}\right) \frac{\partial \varepsilon \rho_j Y_j}{\partial t} - T \varepsilon \rho_j Y_j \frac{\partial C_{p,j}}{\partial t} \tag{92}$$

Similarly, the convection term and the diffusion term in Equation (89) can be replaced by Equations (93), (94), and (95).

$$\frac{1}{r^n}\frac{\partial}{\partial r}\left[r^n \varepsilon \rho_g u Y_j \int_{T_0}^{T} C_{p,j} dT\right] = \frac{1}{r^n}\frac{\partial}{\partial r}\left(r^n \varepsilon \rho_g u Y_j C_{p,j} T\right)$$
$$+\left(\int_{T_0}^{T} C_{p,j} dT - T C_{p,j}\right)\frac{1}{r^n}\frac{\partial}{\partial r}\left[r^n \varepsilon \rho_g u Y_j\right] - \frac{1}{r^n}\left(r^n \varepsilon \rho_g u Y_j T\right)\frac{\partial C_{p,j}}{\partial r} \tag{93}$$

$$\frac{1}{r^n}\frac{\partial}{\partial r}\left(r^n \rho_g \varepsilon D_{eff,j} \frac{\partial Y_j}{\partial r} \int_{T_0}^{T} C_{p,j} dT\right) = \frac{1}{r^n}\frac{\partial}{\partial r}\left[r^n \rho_g \varepsilon D_{eff,j} \frac{\partial Y_j}{\partial r} C_{p,j} T\right]$$
$$\left(\int_{T_0}^{T} C_{p,j} dT - T C_{p,j}\right)\frac{1}{r^n}\frac{\partial}{\partial r}\left[r^n \rho_g \varepsilon D_{eff,j} \frac{\partial Y_j}{\partial r}\right] - \frac{1}{r^n}\left(r^n \rho_g \varepsilon D_{eff,j} \frac{\partial Y_j}{\partial r} T\right)\frac{\partial C_{p,j}}{\partial r} \tag{94}$$

$$\frac{1}{r^n}\frac{\partial}{\partial r}\left(r^n D_{eff,k} \frac{\partial \rho_k}{\partial r} \int_{T_0}^{T} C_{p,k} dT\right) = \frac{1}{r^n}\frac{\partial}{\partial r}\left[r^n D_{eff,k} \frac{\partial \rho_k}{\partial r} C_{p,k} T\right]$$
$$\left(\int_{T_0}^{T} C_{p,k} dT - T C_{p,k}\right)\frac{1}{r^n}\frac{\partial}{\partial r}\left[r^n D_{eff,k} \frac{\partial \rho_k}{\partial r}\right] - \frac{1}{r^n}\left(r^n D_{eff,k} \frac{\partial \rho_k}{\partial r} T\right)\frac{\partial C_{p,k}}{\partial r} \tag{95}$$

The heat capacity of each species is usually just a function of temperature, and is not related to time and position. In the current physical model, the temperature is a function of both time and position, so the heat capacity would change with time and position. The following transformations are made, as illustrated in Equations (96) and (97).

$$\frac{\partial C_p}{\partial t} = \frac{\partial C_p}{\partial T}\frac{\partial T}{\partial t} \tag{96}$$

$$\frac{\partial C_p}{\partial r} = \frac{\partial C_p}{\partial T}\frac{\partial T}{\partial r} \tag{97}$$

Substituting Equations (90) ~ (95) back into Equation (89), and simplifying the resulted equation with Equations (22) ~ (28) and (96) ~ (97), Equation (89) becomes Equation (98).

$$\begin{aligned}
&\frac{\partial}{\partial t}\left[\left(\sum_i \rho_i C_{p,i} + \sum_k \rho_k C_{p,k} + \rho_g \varepsilon \sum_j Y_j C_{p,j}\right)T\right] \\
&+\frac{1}{r^n}\frac{\partial}{\partial r}\left\{\left[r^n \varepsilon \rho_g \left(u\sum_j Y_j C_{p,j} - \sum_j D_{eff,j}\frac{\partial Y_j}{\partial r}C_{p,j}\right) - r^n \sum_k D_{eff,k}\frac{\partial \rho_k}{\partial r}C_{p,k}\right]T\right\} \\
&= \frac{1}{r^n}\frac{\partial}{\partial r}(r^n K_{eff}\frac{\partial T}{\partial r}) + \sum_m r_m \Delta H_m^0 + \sum_l \left(C_{p,l}T - \int_{T_0}^{T} C_{p,l}dT\right)S_l \\
&+\left(\sum_i \rho_i \frac{\partial C_{p,i}}{\partial T} + \sum_k \rho_k \frac{\partial C_{p,k}}{\partial T} + \varepsilon\rho_g \sum_j Y_j \frac{\partial C_{p,j}}{\partial T}\right)T\frac{\partial T}{\partial t} \\
&+\left[\left(\sum_j Y_j \frac{\partial C_{p,j}}{\partial T}u - \sum_j D_{eff,j}\frac{\partial Y_j}{\partial r}\frac{\partial C_{p,j}}{\partial T}\right)\varepsilon\rho_g - \sum_k D_{eff,k}\frac{\partial \rho_k}{\partial r}\frac{\partial C_{p,k}}{\partial T}\right]T\frac{\partial T}{\partial r}
\end{aligned} \tag{98}$$

Substituting source terms of each species into the third term on the right side of Equation (98), the following equation is obtained.

$$\sum_l \left(C_{p,l} T - \int_{T_0}^{T} C_{p,l} dT \right) S_l = \sum_m r_m \left(\sum_{reac} \Psi_{reac} \int_{T_0}^{T} C_{p,reac} dT - \sum_{prod} \Psi_{prod} \int_{T_0}^{T} C_{p,prod} dT \right)$$
$$+ \sum_m r_m \left(\sum_{prod} \Psi_{prod} C_{p,prod} - \sum_{reac} \Psi_{reac} C_{p,reac} \right) T \quad , \qquad (99)$$

where, Ψ is the stoichiometric factor of each species in a specific reaction *m*.

So, a final general form of the energy equation, which can be solved by control volume method, is obtained in Equation (100).

$$\begin{aligned}
&\frac{\partial}{\partial t}\left[\left(\sum_i \rho_l C_{p,i} + \sum_k \rho_k C_{p,k} + \rho_g \varepsilon \sum_j Y_j C_{p,j} \right) T \right] \\
&+ \frac{1}{r^n} \frac{\partial}{\partial r} \left\{ \left[r^n \varepsilon \rho_g \left(u \sum_j Y_j C_{p,j} - \sum_j D_{eff,j} \frac{\partial Y_j}{\partial r} C_{p,j} \right) - r^n \sum_k D_{eff,k} \frac{\partial \rho_k}{\partial r} C_{p,k} \right] T \right\} \\
&= \frac{1}{r^n} \frac{\partial}{\partial r} (r^n K_{eff} \frac{\partial T}{\partial r}) + \sum_m r_m \left(\sum_{reac} \Psi_{reac} \int_{T_0}^{T} C_{p,reac} dT - \sum_{prod} \Psi_{prod} \int_{T_0}^{T} C_{p,prod} dT \right) \\
&+ \sum_m r_m \left(\sum_{prod} \Psi_{prod} C_{p,prod} - \sum_{reac} \Psi_{reac} C_{p,reac} \right) T + \sum_m r_m \Delta H_m^0 \\
&+ \left(\sum_i \rho_i \frac{\partial C_{p,i}}{\partial T} + \sum_k \rho_k \frac{\partial C_{p,k}}{\partial T} + \varepsilon \rho_g \sum_j Y_j \frac{\partial C_{p,j}}{\partial T} \right) T \frac{\partial T}{\partial t} \\
&+ \left[\left(\sum_j Y_j \frac{\partial C_{p,j}}{\partial T} u - \sum_j D_{eff,j} \frac{\partial Y_j}{\partial r} \frac{\partial C_{p,j}}{\partial T} \right) \varepsilon \rho_g - \sum_k D_{eff,k} \frac{\partial \rho_k}{\partial r} \frac{\partial C_{p,k}}{\partial T} \right] T \frac{\partial T}{\partial r}
\end{aligned} \qquad (100)$$

The coefficients of the discretization equation for Equation (100) are quite complex compared with those of species conservation equations.

$$D_e = r_e^n \frac{K_{eff,e}}{\delta r_e}, \qquad D_w = r_w^n \frac{K_{eff,w}}{\delta r_w} \qquad (101)$$

$$\begin{aligned}
F_e &= r_e^n \varepsilon \rho_{g,e} \sum_j C_{p,j,e} \left(Y_{j,e} u_e - D_{eff,j,e} \frac{Y_{j,E} - Y_{j,P}}{\delta r_e} \right) - r_e^n \sum_k D_{eff,k,e} \frac{\rho_{k,E} - \rho_{k,P}}{\delta r_e} C_{p,k,e}, \\
F_w &= r_w^n \varepsilon \rho_{g,w} \sum_j C_{p,j,w} \left(Y_{j,w} u_w - D_{eff,j,w} \frac{Y_{j,P} - Y_{j,W}}{\delta r_w} \right) - r_w^n \sum_k D_{eff,k,w} \frac{\rho_{k,P} - \rho_{k,W}}{\delta r_w} C_{p,k,w}
\end{aligned} \qquad (102)$$

$$P_e = \frac{F_e}{D_e}, \qquad P_w = \frac{F_w}{D_w} \tag{103}$$

$$\begin{aligned} a_P^0 &= \frac{\Delta v^0}{\Delta t}\left(\sum_i \rho_i^0 C_{p,i}^0 + \varepsilon \rho_g^0 \sum_j Y_j^0 C_{p,j}^0 + \sum_k \rho_k^0 C_{p,k}^0 \right), \\ a_P^1 &= \frac{\Delta v}{\Delta t}\left(\sum_i \rho_i C_{p,i} + \varepsilon \rho_g \sum_j Y_j C_{p,j} + \sum_k \rho_k C_{p,k} \right) \end{aligned} \tag{104}$$

The last five terms in Equation (100) are lumped as the source term of the energy equation. The source term is linearized so that it obeys Rule 3 (negative-slope linearization) of control volume method described in (Patankar, 1980).

5.3.6. Calculation of the Flow Field

The momentum conservation of the gas phase is simply described by Darcy's law for the porous solid particle domain, shown in Equation (31). Discretization procedure of the momentum equation in the staggered control volume follows Patankar's method (Patankar, 1980). The gas-phase overall continuity equation, which includes a non-zero source term, is turned into a pressure-correction equation by integrating it over the control volume and the time interval, as illustrated below.

First, the discretization equation for the overall gas phase continuity equation is obtained after integration;

$$\frac{\Delta v \rho_g - \Delta v^0 \rho_g^0}{\Delta t} + \left(r_e^n \rho_{g,e} u_e - r_w^n \rho_{g,w} u_w \right) = \frac{\Delta v}{\varepsilon} S_g \,. \tag{105}$$

Substituting the corresponding velocities at both the east and the west interfaces into Equation (105) and rearranging the resulted equation will lead a discretization equation for the pressure correction term p'.

$$a_P p_P^{'} = a_W p_W^{'} + a_E p_E^{'} + b\,, \tag{106}$$

where,

$$a_W = r_w^n \rho_{g,w} d_w\,, \tag{107}$$

$$d_w = \frac{\eta_w}{\mu_w \delta r_w}\,, \tag{108}$$

$$a_E = r_e^n \rho_{g,e} d_e\,, \tag{109}$$

$$a_P = a_W + a_E\,, \tag{110}$$

$$b = \frac{\Delta v}{\varepsilon} S_g - \left[\left(\frac{\Delta v \rho_g - \Delta v^0 \rho_g^0}{\Delta t} \right) + \left(r_e^n \rho_{g,e} u_e^* - r_w^n \rho_{g,w} u_w^* \right) \right]. \tag{111}$$

The discretization equation for pressure correction is solved with the standard TDMA.

5.3.7. Solution for the Particle Shrinking / Swelling

To solve the particle/droplet shrinking/swelling model, Equation is rearranged with the solid species mass conversion replaced by

$$x_i = 1 - \frac{\rho_i v}{\rho_i^0 v^0}\,, \tag{112}$$

where i = moisture, biomass, and char, and we obtain

$$\frac{v}{v_0} = 1 + \sum_i \left(1 - \frac{\rho_i v}{\rho_i^0 v^0} \right) \left(\beta_i - 1.0 \right). \tag{113}$$

It can be further simplified to Equation (114).

$$\frac{v}{v_0} = \frac{1 + \sum_i \left(\beta_i - 1 \right)}{1 + \sum \frac{\rho_i}{\rho_i^0} \left(\beta_i - 1 \right)} \tag{114}$$

The derivative of volume with respect of time results in

$$\frac{1}{v}\frac{dv}{dt} = -\frac{\sum_i \frac{(\beta_i - 1)}{\rho_i^0}\frac{\partial \rho_i}{\partial t}}{1 + \sum_i \frac{\rho_i}{\rho_i^0}(\beta_i - 1)}. \tag{115}$$

For each species in the solid phase in each control volume, the total mass is

$$m_i = \rho_i v. \tag{116}$$

The derivative of the above equation with respect of time is

$$\frac{\partial m_i}{\partial t} = \frac{\partial \rho_i v}{\partial t} = \rho_i \frac{\partial v}{\partial t} + v\frac{\partial \rho_i}{\partial t}, \tag{117}$$

which further results in Equation (118).

$$\frac{\partial \rho_i}{\partial t} = \frac{1}{v}\frac{\partial v \rho_i}{\partial t} - \frac{\rho_i}{v}\frac{\partial v}{\partial t} \tag{118}$$

In Equation (118), the first term at the right side is the mass loss rate per unit volume, which is the source term S_i for this species in the solid phase, then Equation (118) becomes Equation (119).

$$\frac{\partial \rho_i}{\partial t} = S_i - \frac{\rho_i}{v}\frac{\partial v}{\partial t} \tag{119}$$

Substituting Equation (115) into Equation (119), and rearranging the equation leads to Equation (120).

$$\frac{\partial \rho_i}{\partial t} = S_i + \rho_i \sum_j \left(\frac{\beta_j - 1}{\rho_j^0}\right) \cdot S_j, \tag{120}$$

where, j = *char, ash, and biomass.* Equation (120) shows that if the shrinking factor $\beta_j = 1.0$, which is the constant volume case, the density change rate of each species will be

$$\frac{\partial \rho_i}{\partial t} = S_i \quad . \tag{121}$$

The density change rate will slow down if the shrinking factor $0.0 < \beta_j < 1.0$ due to the volume shrinking; similarly, the density change rate will speed up if the shrinking factor $\beta_j > 1.0$ due to the volume swelling. A final case is constant-density shrinking, where $\beta_j = 0.0$. For the case, $\rho_j = \rho_j^{\,0}$ will be the only possible solution for Equation (120) since $\beta_j = 0.0$.

Now, substituting Equation (120) back into Equation (115), Equation (115) can be simplified to Equation (122).

$$\frac{1}{v}\frac{\partial v}{\partial t} = -\sum_i \left(\frac{\beta_i - 1}{\rho_i^{\,0}} \right) \cdot S_i \ , \tag{122}$$

which can be similarly solved by the fully implicit algorithm described in (Patankar, 1980).

With all partial differential equations for species mass fractions, temperature, and pressure being discretized to linear algebraic equations and solved by the TDMA method, the SIMPLE algorithm is chosen to calculate the flow field and ensure the convergence of all variables.

The solution of the mathematical model is coded in C/C++, and the computer time for a single biomass particle combustion simulation depends on particle size, usually 20 minutes for a 5 mm particle.

5.4. Summary

In this chapter, a one-dimensional, single-particle combustion model describing drying, devolatilization, and char oxidation and gasification has been developed. The

mechanisms for each process have been analyzed in detail. The mathematical model was solved with control volume method.

The model is capable of simulating combustion of solid particle or droplet of any shape and size. It can predict the particle temperature distribution, species concentration distribution, and particle/droplet shrinking/swelling behaviors as function of residence time. Its predictions are compared with data derived from the experimental techniques described in the previous chapter to complete the analysis of biomass shape and size impacts on combustion.

6. Results and Discussions

In this project, biomass particle pyrolysis experiments were conducted in two entrained-flow reactors and a single-particle reactor. Mass loss data of sawdust particle during pyrolysis was collected in a short entrained-flow reactor, which doesn't provide optical access and was operated at 1600 K. Biomass particle surface temperatures during pyrolysis and combustion were measured with the imaging pyrometry in a longer entrained-flow reactor, which provides optical accesses. With the single-particle reactor, poplar dowel particle data, including particle surface temperature, inner temperature, and particle mass loss during drying, devolatilization, and combustion, have been collected with type B or K thermocouples, the imaging pyrometry, and the balance.

All data are compared with the theoretical analysis results predicted by the single-particle combustion model previously described.

In this chapter, the single particle combustion model is first validated with mass loss data and particle temperature data collected on the single-particle reactor. Then a series of model predictions with different levels of complexity illustrate the necessity of such a sophisticated structure model for biomass particle combustion modeling. Finally, more model studies and experimental data are presented and discussed.

The differences between measured and predicted data in most cases would be reduced if particle properties (pore sizes, densities, thermal conductivities, etc.) were

altered within the range of their uncertainties. The presentation here includes no such optimization of results. The intention is to illustrate the level of agreement expected with a single set of properties based on independent measurements or literature values – the agreement expected in application of this approach in a predictive rather than a diagnostic mode.

6.1. Single Particle Combustion Model Validation

To validate the single particle combustion model, combustion experiments have been conducted in the single-particle reactor with poplar particles. Particle surface temperature, internal temperature, and mass loss during drying, devolatilization, and char oxidation are measured and compared with model predictions.

The single-particle reactor wall temperature is not uniform in the axial direction due to reactor configurations, so an average wall temperature determined at the location of the particle is used in the model as the reactor wall temperature. Both a type K thermocouple and the imaging pyrometer measure this temperature. The thermocouple readying was 1303 K and the average pyrometer measurement was 1276 K. The imaging pyrometer data are taken as the wall temperature here. A type K thermocouple monitors the center gas temperature. The actual gas temperature was corrected for radiative and other losses from the thermocouple bead based on the wall temperature, bulk gas velocity, and the thermocouple bead size. This resulted in a gas temperature of 1050 K.

6.1.1. Particle Devolatilization

Data for a near-spherical particle (d_p = 11mm) with aspect ratio of 1.0 and a moisture content of 6.0 % (wt), including mass loss, center and surface temperature during pyrolysis appear with model predictions in Figure 58 and Figure 59. The nominal

conditions of this experiment include a reactor wall temperature of 1273 K and gas temperature of 1050 K. All the following validation experiments were conducted at the same conditions.

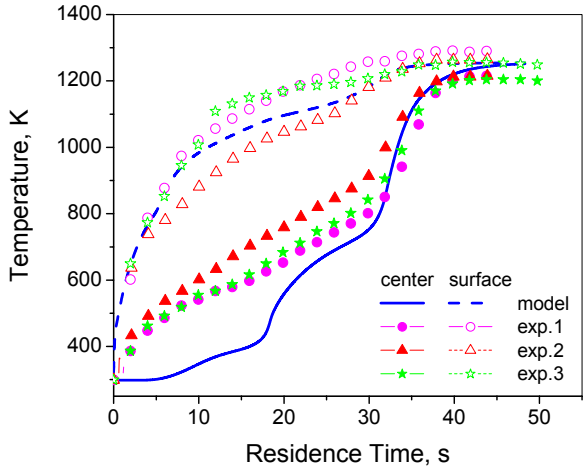

Figure 58 Temperature of near-spherical particle during pyrolysis in nitrogen
d_p = 9.5 mm, AR = 1.0, MC = 6 %(wt), T_w = 1276 K, T_g = 1050 K

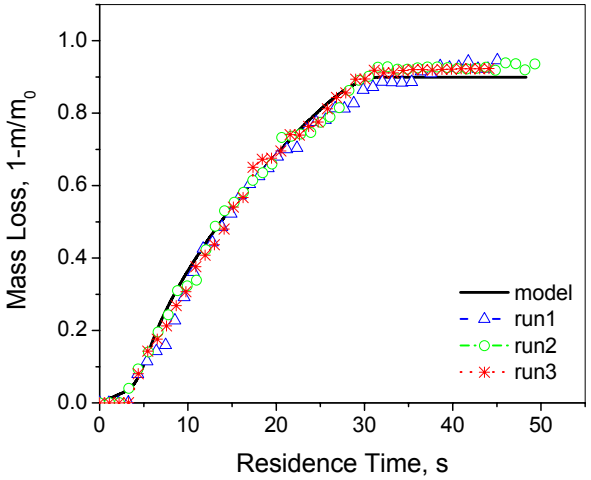

Figure 59 Mass loss of near-spherical particle during pyrolysis in nitrogen
d_p = 9.5 mm, AR = 1.0, MC = 6 %(wt), T_w = 1276 K, T_g = 1050 K

The particle mass loss and particle surface temperature predictions generally agree with experimental data except that the measured particle center temperature increases

faster than the model predictions at the beginning. This might be caused by the thermal conduction effects through the wire while measuring the particle center temperature. In principle, the measured particle surface temperature and center temperature should reach the same value at the end of pyrolysis, but a small discrepancy exists due to reactor temperature non-uniformity and differences in thermocouple bead size and shape. A more detailed discussion of the features of these data appears after discussing the potential cause of the discrepancy in the center temperature data.

To determine the thermocouple lead wire impact on the measured center temperature, a second experiment at the same conditions used a cylindrical particle of the same diameter but with aspect ratio of 4.0. Two thermocouples monitored the center temperature, one passing axially and a second passing radially through the particle. The axial thermocouple should be less impacted by heat conduction through the leads since the particle provides some insulation from the radiation and bulk-flow convection. In Figure 60, lines 1 and 2 are particle center temperatures measured in the radial direction; lines 3 and 4 are results measured in axial direction. As indicated, the center temperature measured in the radial direction increases much faster than that measured in axial direction at the beginning, indicating that the thermocouple wire conduction influences initial center temperature measurements. The model prediction for the center temperature generally agrees with the average of the axial direction.

Mass loss data collected in several runs for the cylindrical particle are compared with model predictions in Figure 61.

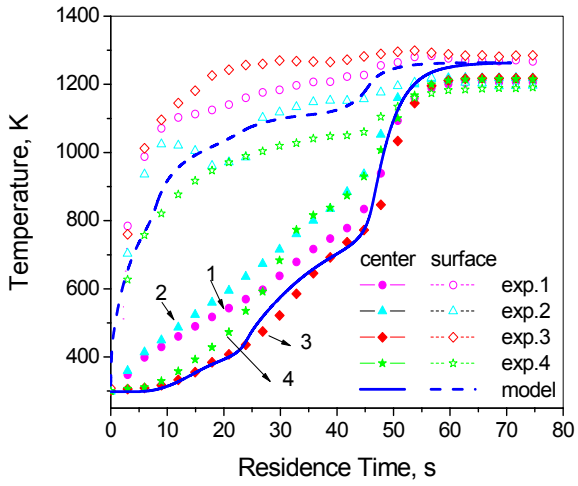

Figure 60 Temperature comparison of a cylindrical particle during pyrolysis in nitrogen
d_p = 9.5 mm, AR = 4.0, MC = 6 %(wt), T_w = 1276 K, T_g = 1050 K

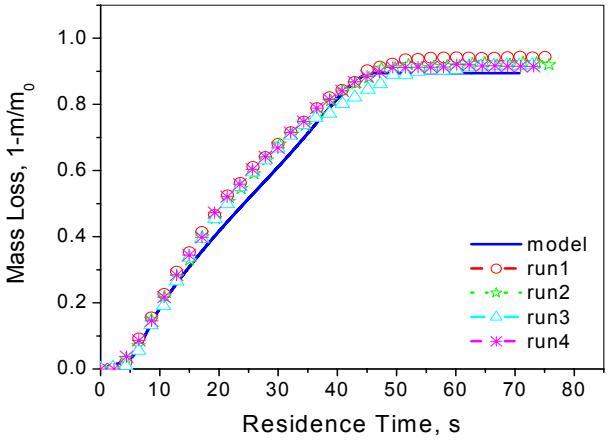

Figure 61 Mass loss comparison of a cylindrical particle during pyrolysis in nitrogen
d_p = 9.5 mm, AR = 4.0, MC = 6 %(wt), T_w = 1276 K, T_g = 1050 K

The shapes of the temperature histories illustrate the complexity of this large-particle pyrolysis process even in the absence of complications arising from surface oxidation and surrounding flames. The initial low center temperature is associated with vaporization, which occurs at subboiling temperatures under nearly all conditions. Experiments with more moist particles reported later illustrate more clearly the impacts of vaporization.

After vaporization, particles heat up relatively slowly, mainly because of devolatilization reactions in outer layers of the particle generate significant gas velocities in the pores (commonly reaching 0.2 m/s), thereby impeding internal heat transfer. After devolatilization, the rate of particle heating increases rapidly, mainly because the particle mass is greatly reduced relative to the early data by virtue of volatile losses but significantly because the internal heat transfer impediment from rapid outgassing also subsides. By contrast, the surface particle temperature increases rapidly and is less susceptible to slow heat transfer rates or even significant impacts from the blowing factor, in this case because radiation is the dominant heating mechanism. If convection were the primary heating mechanism, surface temperature heating rates would decrease by factors of up to 10 during rapid mass loss. These processes result in temperature differences between the surface and the center of many hundreds of Kelvins during particle heatup.

6.1.2. Particle Drying and Devolatilization

The drying model was further tested using wet particles with higher moisture content. Particle surface temperature and center temperature were measured with type K thermocouples in a cylinder particle with 40 % (wt) moisture (based on total wet particle mass) during drying and devolatilization. Similar to the previous experiments, particle center temperature was measured in both axial and radial directions. Results appear in Figure 62, which illustrates model predictions compared to data. Lines 1 and 2 indicate the center temperature measured in the radial direction and lines 3 and 4 indicate the axial measurement. Both the model prediction and experimental data showed that the particle temperature first rises to a constant value near but below the boiling point, with

evaporation mainly occurring in this stage. Following drying, the particle temperature again increases until biomass devolatilization slows the particle heating rate due to endothermic decomposition of biomass materials (minor impact) and the effect of rapid mass loss on the heat transfer coefficient – often called the blowing parameter (major impact). Once all biomass material converts to char, light gas, and tar, the residual char undergoes a rapid temperature rise due to its lower mass (major impact), lower heat capacity (minor effect) and return of the blowing factor to near 1 (major effect). During most of the particle history, the predicted surface temperature is approximately 200 K below the average measured surface temperature. The predicted surface temperature depends primarily on radiative heating, convective heating, the impact of the blowing factor on heat transfer, and the rate and thermodynamics of water vaporization. As discussed later, the blowing factor in this radiation-dominated environment has little impact on the predictions. The thermodynamics of water vaporization are in little doubt, although the thermodynamics of the chemically adsorbed water losses are relatively uncertain. It is also possible that the reactions of the particle with its attendant changes in size and composition compromise the thermal contact between the surface thermocouple and the particle. There is no clear indication of whether the discrepancy arises from experimental artifacts or from uncertainties in emissivity and transport coefficients or other factors.

Figure 63 compares the predicted and measured mass loss data. The model does not predict the measured trend within its uncertainty though the predictions and measurements are in qualitative agreement. The disagreement is likely related to the temperature issues discussed above, including the non-uniformity of reactor temperature

distribution. For a cylindrical particle horizontally oriented in the center of the reactor, its ends were exposed to higher temperature environment but the model applied an average bulk gas center temperature.

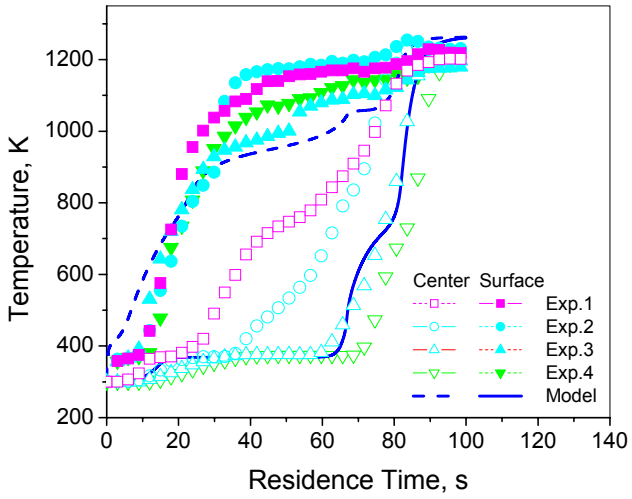

Figure 62 Temperature comparisons of a cylindrical particle during drying and pyrolysis in nitrogen
d_p = 9.5 mm, AR = 4.0, MC = 40 %(wt), T_w = 1276 K, T_g = 1050 K

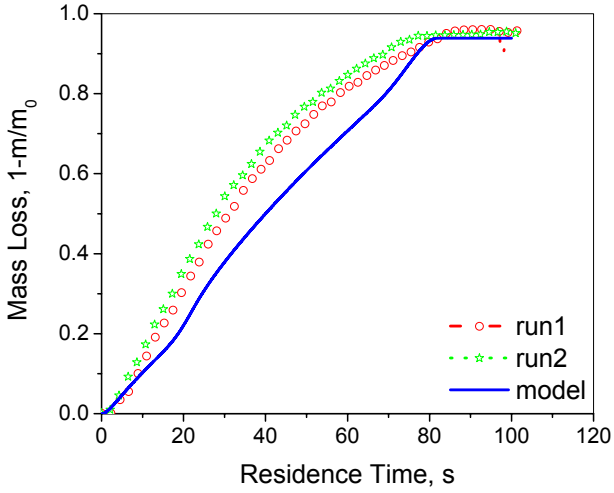

Figure 63 Mass loss of a cylindrical particle during drying and pyrolysis in nitrogen
d_p = 9.5 mm, AR = 4.0, MC = 40 %(wt), T_w = 1276 K, T_g = 1050 K

The model was also validated with wet near-spherical particle drying and devolatilization data, as illustrated in Figure 64 and Figure 65. Results show that the predicted mass loss curve agrees with experimental data well. Both the surface temperature and center temperature profiles are similar to those for the wet cylinder particle illustrated above. The surface temperature data show that the particle surface temperature rises to the water subboiling point and, presumably after the surface dries, rises rapidly. The center temperature data show qualitative behavior similar to that of the cylinder except that the impacts of heat conduction in the thermocouple leads remain in all of the data.

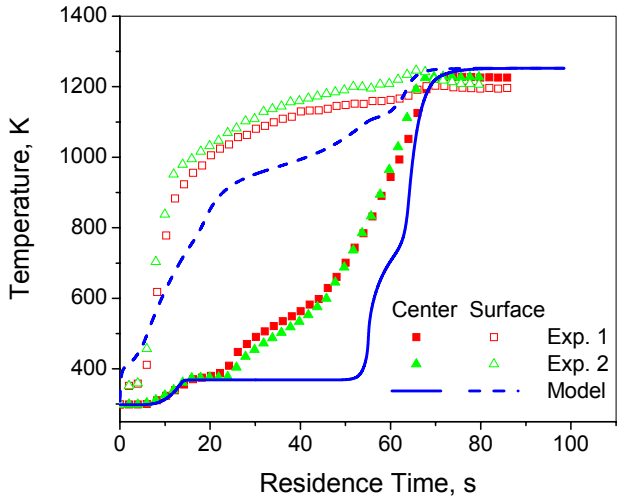

Figure 64 Temperature data of a wet near-spherical poplar particle during drying and pyrolysis in nitrogen
d_p = 9.5 mm, AR = 1.0, MC = 40 %(wt), T_w = 1276 K, T_g = 1050 K

Figure 64 indicates measured surface and center temperatures increase more rapidly than the predicted values. The surface temperature discrepancy among the experimental data and model result can be explained by the experimental setup. When the wet particle

was inserted into the reactor, the particle surface started to dry up. The thermocouple could not measure exactly the surface temperature since it was buried right next to the surface, which stayed near the boiling point as shown in the data. After the particle dried to some extent, the particle started to shrink and/or crack, compromising the contact efficiency of the thermocouple. On the other hand, for the center temperature measurement discrepancy, the heat conducted from the hot environment to the thermocouple bead through the thermocouple wire may still be the major influence in the temperature measurements when the particle is small as illustrated above for the dry cylinder particle.

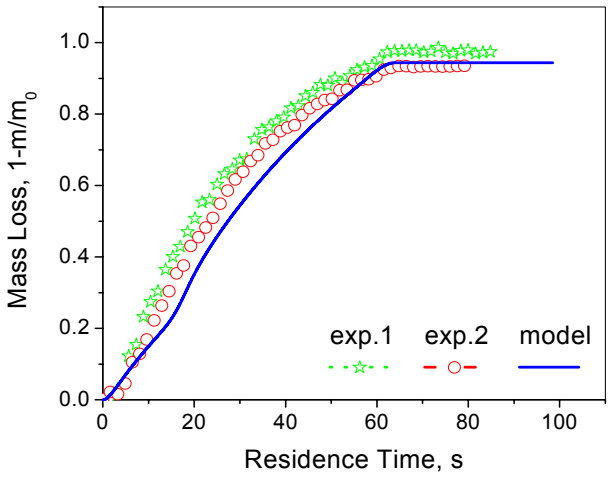

Figure 65 Mass loss of a wet near-spherical poplar particle during drying and pyrolysis in nitrogen
d_p = 9.5 mm, AR = 1.0, MC = 40 %(wt), T_w = 1276 K, T_g = 1050 K

6.1.3. Particle Combustion

Figure 66 shows the temperature profiles of a wet, near-spherical particle with 40% (wt) moisture content (based on the total wet particle mass) and aspect ratio of 1.0 during combustion process.

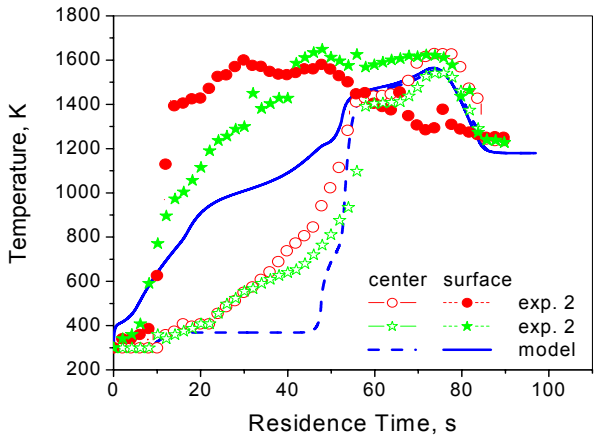

Figure 66 Temperature profiles of a near-spherical wet particle during combustion in air
d_p = 9.5 mm, AR = 1.0, MC = 40 %(wt), T_w = 1276 K, T_g = 1050 K

A Type-B thermocouple provides temperature data for combustion experiments since the peak temperatures exceed the reliable range of Type-K thermocouples. The measured particle surface temperatures are not consistent with model prediction due to experimental artifacts associated with a shrinking particle. The surface contact is lost as the particle shrinks and the bead becomes exposed to the surrounding flame. The measured particle center temperatures appear to disagree with model predictions, though the disagreement arises primarily from thermocouple wire conduction. Both experimental data and model predictions show that during the char burning stage the particle temperature increases to a peak value and then declines dramatically. This supports theoretical descriptions of large-particle combustion mechanisms. Oxidizer diffusion rates primarily control combustion rates in char consumption, which proceeds largely with constant density and shrinking particle diameter. The char particle oxidation front will finally reach the center of the particle as particle size gets smaller with ash built up in the outer layer of the particle. The pseudo-steady-state combustion rate/temperature of

the particle first increases then decreases with size due to changes in the relative importance of radiation losses, convection, and diffusion. Once the char is completely consumed the particle (ash) cools rapidly to near the convective gas temperature, depending on the radiative environment. The mass loss curves as functions of time are shown in Figure 67.

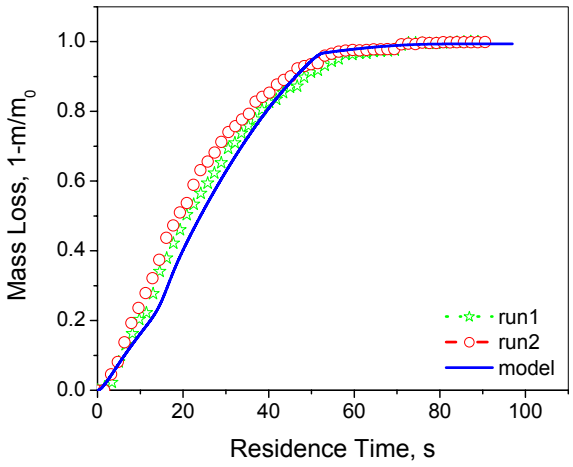

Figure 67 Mass loss of a near-spherical wet particle during combustion in air
d_p = 9.5 mm, AR = 1.0, MC = 40 %(wt), T_w = 1276 K, T_g = 1050 K

For a low moisture content (6 %(wt)), near-spherical particle (d_p = 9.5 mm, AR = 1.0), the flame temperatures are measured with both thermocouple and the camera pyrometry. A type B thermocouple mounted near the particle surface provides some measurements of the flame temperature surrounding the particle. The upper limit of a type B thermocouple is about 2100 K, and the thermocouple data above this value is not accurate, as shown in Figure 68. The flame temperature was also interpreted by the imaging pyrometer with gray-body emission assumption, where the results are combinations of flame and particle surface radiations. Both thermocouple and pyrometry

data are compared with model predictions in Figure 68, where the flame receded away from the thermocouple after devolatilization. The thermocouple measurements fluctuate due to the turbulence and two-dimensional effects caused by the bulk gas convection, which is not captured in this one-dimensional model. In the camera pyrometry measurements, soot was assumed as gray body emitter. The camera pyrometry measurements can be improved if spectral-dependent emissivity is applied in the calculation. The model prediction of the flame indicates the transition of combustion from devolatilization stage to char burning stage, appearing in Figure 68. Results show that model predictions generally agree with both the camera-measured data and thermocouple data, and the difference is within measurements uncertainty.

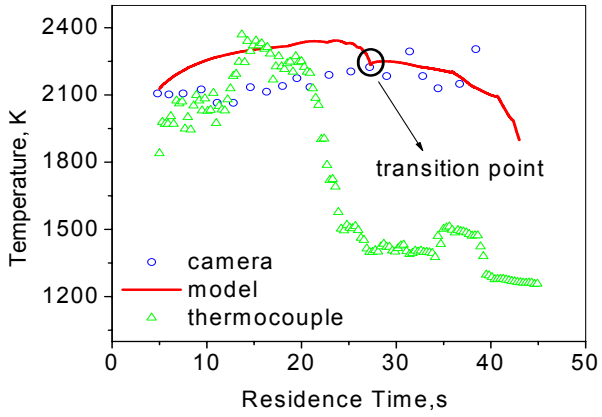

Figure 68 Flame temperature comparison during a near-spherical particle combustion in air
d_p = 9.5 mm, AR = 1.0, MC = 6 % (wt), T_w = 1273 K, T_g = 1050 K

So far, the particle combustion model has been validated with each sub-process, including drying, devolatilization, and oxidation. It is ready to further investigate biomass particle combustion.

6.2. Effects of Various Factors on Biomass Particle Combustion

With the validated particle model, a series of predictions of different levels of complexity are compared with some sets of experimental data collected in both the entrained-flow reactor and the single-particle reactor, starting with an isothermal, spherical particle model, which is appropriate to pulverized coal particle.

6.2.1. Non-isothermal Effects

Both experimental data and model predictions showed that large temperature gradients exist in large biomass particles during combustion. An isothermal particle assumption incorrectly predicts both temperature and mass loss for large particles, as illustrated in Figure 69, where pyrolysis experimental data of a 9.5 mm dry, near-spherical particle are compared with model predictions with isothermal and non-isothermal assumptions. The model with isothermal assumption predicts overall conversion rates approximately three times faster than the non-isothermal model, the latter being in good agreement with experimental data. In the isothermal prediction, the surface temperature, which controls the rate of convective and radiative heat transfer, is the same as the average particle temperature. The prediction with the temperature gradient indicates the surface temperature increases much faster than the average temperature, decreasing the average driving force for heat transfer and prolonging the reaction time of the particle. The difference between isothermal predictions and predictions with temperature gradients decreases with decreasing particle size, but the predicted conversion times do not become comparable (within 10 %) until the size is less than 100 micron – which is much smaller than the average particle size used in commercial operation.

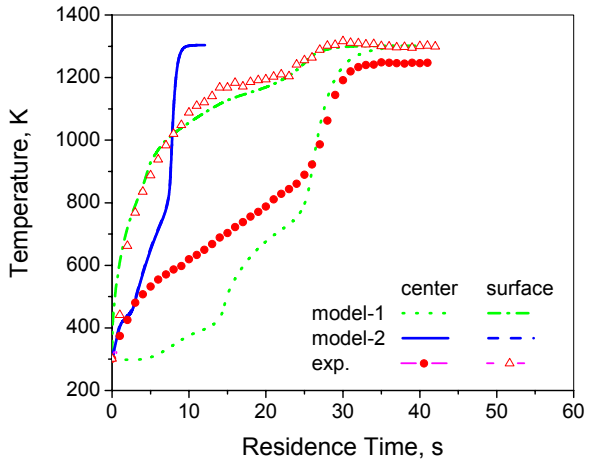

Figure 69 Effects of temperature gradients on particle pyrolysis in nitrogen
Non-isothermal assumption for model-1 and isothermal assumption for model-2
d_p = 9.5 mm, AR = 1.0, MC = 6 % (wt), T_w = 1273 K, T_g = 1050 K

6.2.2. Effects of Particle Shape and Size

Mass loss data of particles of varied shapes and sizes were collected in both the entrained-flow reactor and the single-particle reactor and modeled with different shape assumptions. Small size sawdust samples (Set I, see Table 2) were pyrolyzed in the entrained-flow reactor and large size poplar wood samples (Set I, see Table 4 and Set II, see Table 5) were used in the single-particle reactor.

The wall and gas temperatures of the short entrained-flow reactor measured by type B thermocouples during sawdust pyrolysis experiments appear in Figure 70.

To collect char samples at different residence times, the collection probe was fixed at the bottom of the reactor tube and the residence time was adjusted through moving the feed probe. Based on these average temperature profiles of reactor walls and gas, the mathematical model simulates devolatilization of the sawdust particle sample set I with the specific shapes described in the sample preparation section. Figure 71 illustrates the

mass loss history of the three samples. Both the experimental data and model predictions show that the near-spherical particle releases mass more slowly compared with the other two shapes, while the flake-like particle devolatilizes slightly faster than cylinder-like particle. The model prediction indicates slightly more rapid mass release than the experimental data in each case. There are at least two possible explanations for this discrepancy. First, a slightly non-uniform size and/or shape distribution of the samples almost certainly exists, despite the relatively careful sample preparation procedures. These variations in shape and size tend to broaden the observed curve of mass loss vs. time as the small particles react faster than the larger particles. Secondly, actual devolatilization rates are much more complicated and involve reactions with a broader range of rates than are captured by the relatively simple model used here. Such simple models commonly capture the essence of the mass release but not the details at either the initial or final stages, as reflected by our data compared to the model predictions. Despite these slight inconsistencies, the model and data generally agree, though not within the uncertainties of the data.

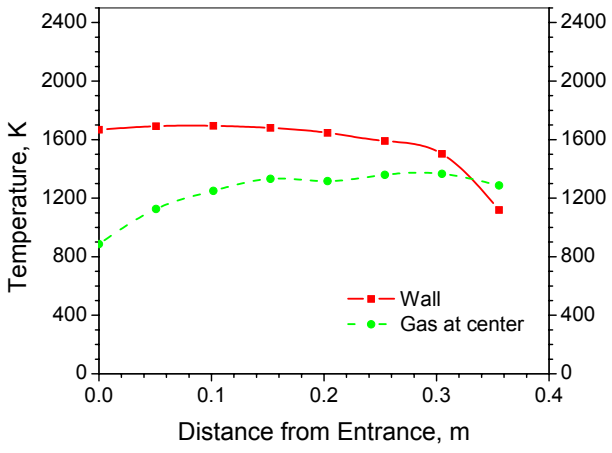

Figure 70 Entrained-flow reactor wall temperature and gas temperature along reactor

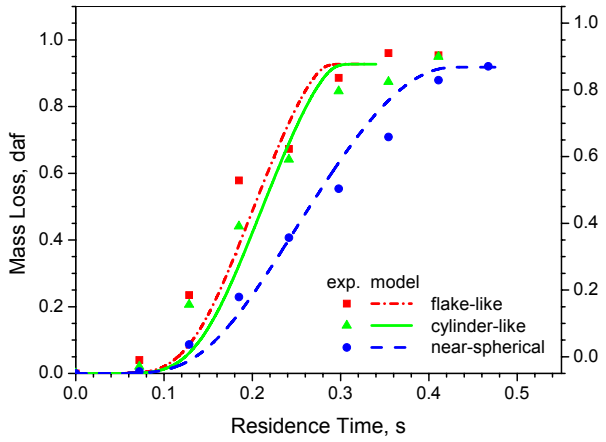

Figure 71 Mass loss histories of sawdust particles with different shapes but the same total mass/volume during pyrolysis in nitrogen in entrained-flow reactor $d_{p,eq.}$ = 0.32 mm; reactor wall temperature and gas temperature see Figure 70

The flake-like and cylinder-like particles have larger surface areas and smaller thicknesses, which result in a higher heating rate and faster heat and mass transfer to the particle. The predicted surface and center temperatures for the three samples are illustrated in Figure 72. As expected, the near-spherical particle temperature rises more slowly than that of the other two shapes due to its lower surface-area-to-volume ratio.

The effect of particle shape on conversion time and product distribution should be more apparent for large particles than small particles. Large particles that sustain substantial internal temperature and composition gradients transfer heat and mass at rates that scale with surface area. Spheres have the lowest surface-area-to-volume ratio of all shapes and should therefore transfer heat and mass at slower rates than aspherical particles of the same volume/mass. By contrast, particles with little or no internal temperature and compositions gradients transfer mass and heat at rates proportional to total particle volume. These typically small particles are less sensitive to shape than are

larger particles of the same material in the same environment. These data and the analyses quantify these theoretical trends and indicate that particles as small as 0.3 mm equivalent diameter experience significant differences in conversion rate based on shape. This renders spheres poor choices for many if not most biomass fuels. This concept is similar to but not identical with using a Biot number to determine when internal temperature (and composition) gradients are significant. The Biot number determines when internal temperature (and composition) gradients can be ignored (Bi < 0.1) but does not in itself help determine how to treat the impacts of shape on such gradients when they shouldn't be ignored.

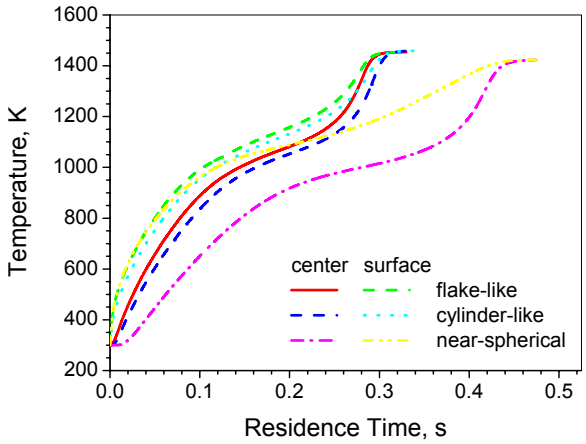

Figure 72 Particle temperature history comparison for sawdust particles with different shapes but the same total mass/volume during pyrolysis in nitrogen $d_{p,eq.}$ = 0.32 mm; reactor wall and gas temperature see Figure 70

These figures include available data from the entrained flow reactor, but the data do not range over sufficient size to provide convincing experimental verification of the model predictions (because of reactor limitations). Investigations in the other facilities resolve this data gap. Specifically, the effects of particle shape on conversion time for

large size particles will be shown and discussed (experimentally and theoretically) next with data collected in the single-particle reactor.

The mass loss rate difference between the near-spherical and aspherical particles increases with increasing size. As illustrated in Figure 73, particles with an equivalent diameter of 9.5 mm and different shapes, the near-spherical particle pyrolyze slowly compared with the two aspherical particles, consistent with model predictions.

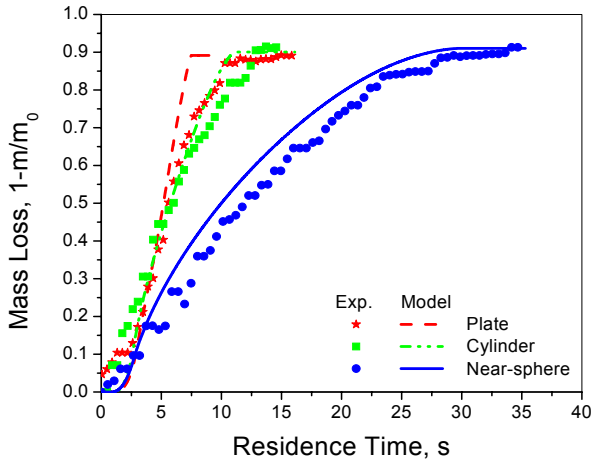

Figure 73 Mass loss profiles of large poplar particles with different shape and same mass during pyrolysis in nitrogen
$d_{p,eq.}$ = 11 mm, $AR_{cylinder}$ = 8.0, AR_{plate} = 8.0, $AR_{near\text{-}sphere}$ = 1.0, MC = 6 % (wt), T_w = 1273 K, T_g = 1050 K

Relative to the objective of this investigation, the data and the model agree quantitatively and definitively that near-spherical particles react more slowly than do less symmetrical particles of the same mass. The mass losses differ by as much as a factor of two during most of the particle histories based on both the predictions and the measurements. Small size sawdust pyrolysis data indicate that at these sizes, which are small relative to commercial uses of biomass, asphericity plays a significant role in

overall conversion. The effects of asphericity should increase with increasing size and increasing aspect ratio, appearing below.

In general, compared with aspherical particles with aspect ratios of 5.0, the conversion time of near-spherical particles can be twice that of aspherical particles for particle sizes larger than 10 mm, (Figure 74); the ratio becomes greater, up to 2.5 when the aspect ratio of aspherical particles increases to 8.0, as illustrated in Figure 75. Commercially significant biomass particles commonly have aspect ratios as large as 12. Less difference exists between the two aspherical shapes since they have about the same surface area to volume ratio.

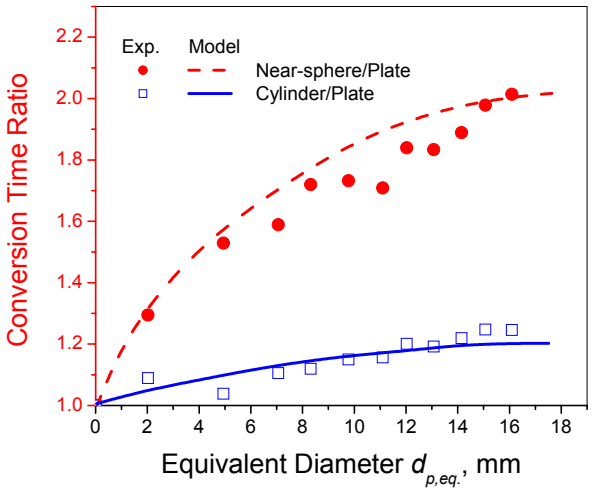

Figure 74 Effects of particle shape and size on conversion time during pyrolysis in nitrogen (non-spherical particle AR=5.0)
MC = 6 % (wt), T_w = 1273 K, T_g = 1050 K

The above illustrations show that particle asphericity and sizes play important role in particle conversion process. A spherical particle would lead to substantial error in predicting combustion behaviors of biomass particles of commercial size and shape.

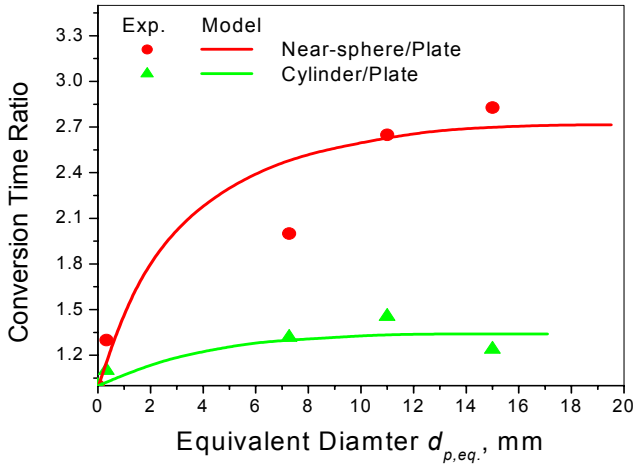

Figure 75 Effects of particle shape and size on conversion time during pyrolysis in nitrogen (non-spherical particle AR=8.0)
MC = 6 % (wt), T_w = 1273 K, T_g = 1050 K

6.2.3. Effects of Surrounding Flame during Particle Combustion

The current single particle combustion model simulates the boundary layer and the flame formed around the particle surface in the boundary layer, as well as predicting the boundary layer thickness.

Figure 76 illustrates the effects of the boundary layer simulation and surrounding flame on the particle temperature profiles during combustion. Simulations both including and neglecting the surrounding flame appear in this graph. As expected, essentially no difference exists between the two simulations early in devolatilization (flame not yet ignited). Slight differences in the surface temperature start to appear during the late devolatilization stage and early oxidation stage of combustion, but the flame actually decreases the predicted surface temperature in this case. This counterintuitive decrease is associated with the flame consuming oxygen in the boundary layer that otherwise would have reacted with the particle. The relatively minor thermal feedback from the flame to

the particle impacts the particle surface temperature less than the reduction in surface reaction associated with the decreased oxygen concentration. During the bulk of oxidation, the flame increases the predicted surface temperature by about 100 K. The modeled particle final temperatures differ from each other by about 20 K. This is caused by the method applied to determine the boundary layer thickness. In the model including flame layer the boundary layer thickness was calculated based on the linear heat and mass transfer correlations which were used in the model without flame layer. In the boundary layer, temperature distribution is not linear for a spherical coordinate and the tangent (slope) on the surface gets greater than linear distribution. This increased the convection heat transfer in the boundary and hence decreased the particle surface temperature.

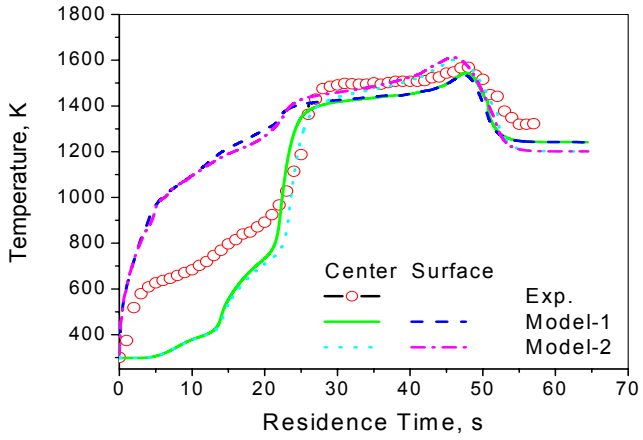

Figure 76 Effects of flame on near-spherical particle temperature during combustion in air
Model-1 stands for results without flame included, model-2 for those with flame include; d_p = 9.5 mm, AR=1.0, MC = 6 % (wt), T_w = 1273 K, T_g = 1050 K

Model results also indicate that particle temperature becomes dramatically more uniform during char burning, although the flame feedback maintains a surface temperature greater than the center temperature, unlike theoretical predictions for

particles with oxygen penetration but no flame feedback. These relatively subtle effects on flame temperatures are too small for accurate measurements by our techniques.

The comparisons between experimental data and model predictions with different levels of complexity demonstrate that, for biomass particle combustion a model with such a sophisticated structure is necessary, which takes particle temperature and concentration gradients, particle shape effects, and flame effects into account.

6.3. Particle Temperature Measurements and Comparison with Model Predictions

Particle surface temperature data were collected for both sawdust particles in the long entrained-flow reactor and poplar particles in the single-particle reactor during pyrolysis and combustion.

6.3.1. Sawdust Particle Surface Temperature in the Entrained-flow Reactor

Combustion experiments (air as carrier gas) for the sawdust particle sample set II were conducted on the long entrained-flow reactor with the imaging system. The reactor wall temperature distribution along the reactor appears in Figure 77.

The particle surface temperatures were measured with the camera pyrometry installed around the entrained-flow reactor through optical accesses. Particle traveling speed in the reactor was determined with the imaging system. Figure 78 illustrates the sawdust particle surface temperature distribution when the particle was heated up in the reactor before a flame was formed around. A relatively poor image was obtained since the particle traveled at an average speed of about 3.0 m/s and the particle surface temperature was not high enough to use a very short exposure time. The average particle surface temperature was 1173 K, as indicated in the temperature map.

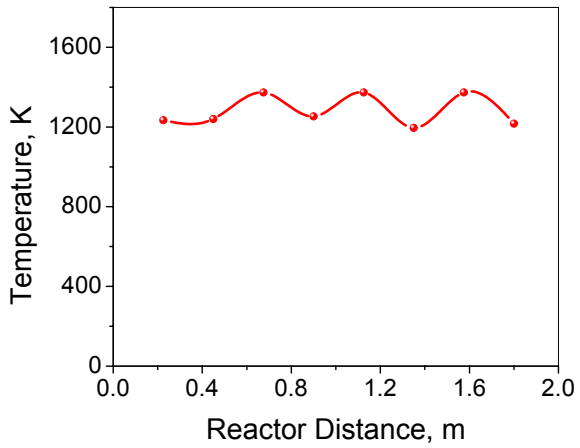

Figure 77 Reactor wall temperature distribution of the long entrained-flow reactor

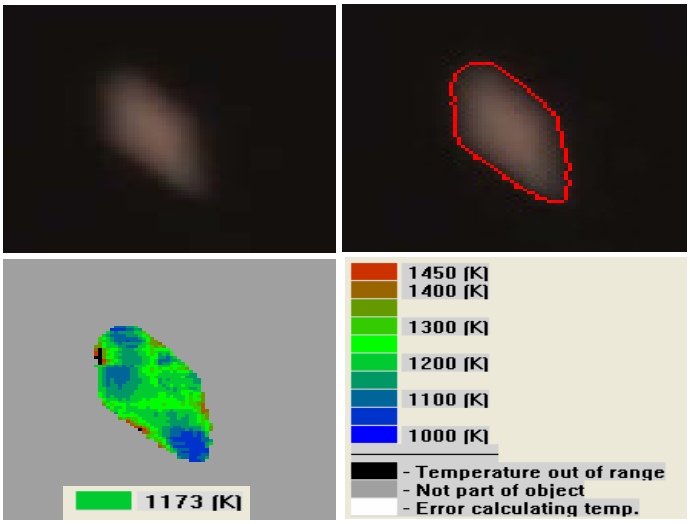

Figure 78 Particle surface temperature distribution during pyrolysis in nitrogen in entrained-flow reactor
$d_{p,eq.}$ = 0.3 mm, MC = 6 % (wt), T_w = 1312 K, T_g = 1124 K

Once the particle starts to burn in the reactor, the particle itself will be surrounded by a flame. The flame may not completely block the radiation from the char particle surface, so both the flame and the particle surface contribute the signal received by the pyrometer sensor. The measured temperature will be a value between the char surface temperature and the flame/soot temperature. The measurement accuracy depends on the relative

distance between soot cloud and the particle surface (which one is closer to the focus point of the imaging pyrometer), char surface temperature, flame temperature, soot absorption, etc. The temperature distributions of two burning particles in the entrained flow reactor are shown below.

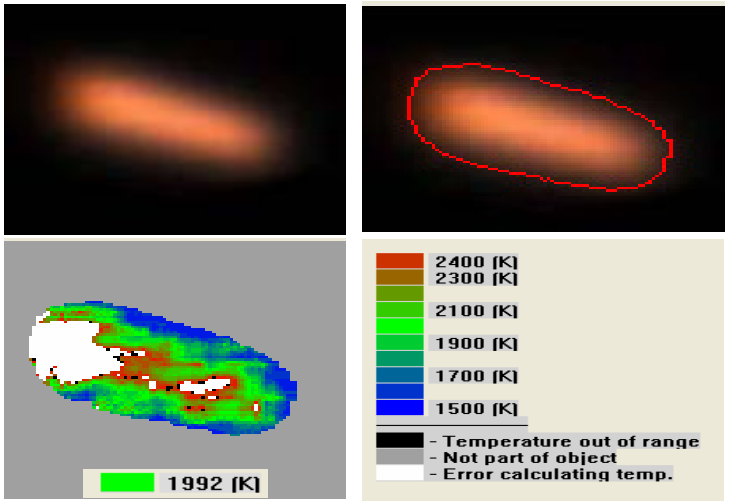

(a) Particle 1

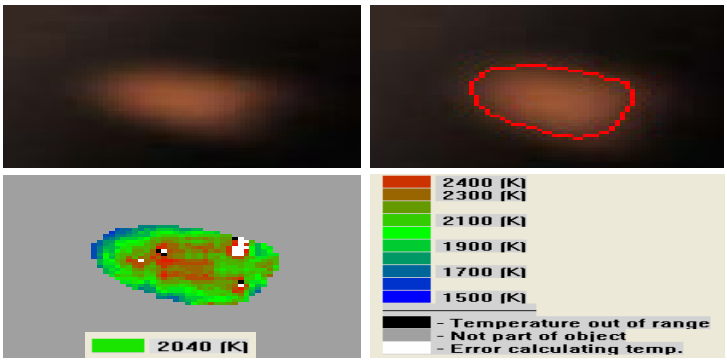

(b) Particle 2

Figure 79 Temperature map of sawdust particle in air in entrained-flow reactor $d_{p,eq.}$ = 0.3 mm, MC = 6 % (wt), T_w = 1312 K, T_g = 1124 K

As illustrated in Figure 79, the temperatures in all the maps range from 1500 K to 2500 K, with an average temperature of about 2000 K, which is reasonably close to the adiabatic flame temperature of most dry hydrocarbon fuels. Some areas in the maps are marked as errors, which can be caused by two situations: the pixel is saturated or the pixel intensity is too low to obtain reliable temperature data.

6.3.2. Poplar Particle Surface and Flame Temperature in Single-particle Reactor

The imaging pyrometers measure particle surface temperature and flame temperature during devolatilization and char burning through the optical accesses ports in the single-particle reactor wall. Thermocouples provide additional measurements of some of these data in many experiments.

When the wood particle is first inserted into the reactor, the particle surface immediately rises, but the reflection from the reactor wall dominates the particle surface radiance as explained in the imaging pyrometry development section. With the reflection effect accounted in the calculation of particle surface temperature, the pixel intensity ratio of any two channels differs from measurements without reflection, as illustrated in Figure 80, where the wall temperature is assumed to be 1300 K and the particle has an emissivity of 0.85. As shown in Figure 80, both the ratio of blue channel to the red channel and that of the green channel to the red channel first increase and then decrease with increasing temperature. As indicated, the temperature is uniquely defined by the pixel intensity ratio only when it exceeds the wall temperature. At low temperatures (< about 800 K in this case), the measurement is insensitive to temperature. Between these low-temperature and furnace-wall temperature limits, a given ratio of signals generally corresponds to two temperatures. At the lower of these two temperatures, surface

reflections of wall radiation contribute to the measured signal more than particle surface emission, with the opposite being the case at the higher temperature. Determining which of the two temperatures is correct generally depends on additional information. The assumption that the surface temperature monotonically increases can often provide enough information to make such distinctions.

The specific results illustrated in this figure depend on temperatures and emissivities of walls and surfaces, but the general trends are characteristic of the analysis.

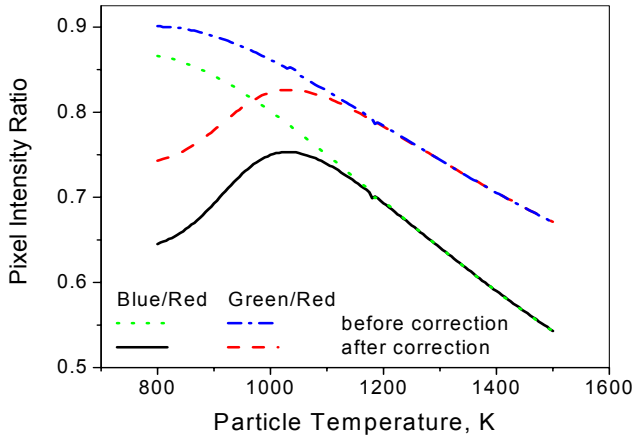

Figure 80 Pixel intensity ratios of a particle in furnace before and after reflection effects corrected
ε_w=1.0, ε_p=0.85, T_w = 1300 K

Based on the reflection correction analysis, time-resolved particle pyrolysis videos from three orthogonal cameras provide surface temperature of near-spherical poplar particles. The camera-measured particle surface temperatures as functions of time appear in Figure 81 and Figure 82 together with thermocouple measured results and model predictions.

For the pyrolysis of poplar particle, the particle surface emissivity was also calculated with the algorithm based on reactor wall reflection correction. An average of 0.99 was obtained, which is different from the typical wood emissivity of 0.85. This might be related with the reacting surface properties (charring). In cases where wall radiation is a not a factor, the pyrometry has to be calibrated with respect to working distance to measure particle surface emissivity, which is not done in this project.

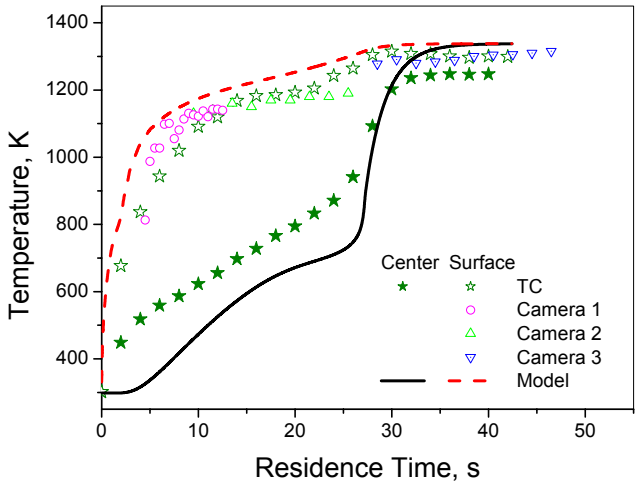

Figure 81 Particle surface temperature comparisons during pyrolysis in nitrogen – run 1
d_p = 9.5 mm, AR = 1.0, MC = 6 % (wt), T_w = 1373 K, T_g = 1050 K

The spatially and temporally resolved imaging pyrometer results indicate that combustion proceeds with non-uniform particle surface temperature. Specifically, the particle surfaces exposed to the most intense radiation (bottom) and, during oxidation, those at the leading edge in the induced convective flow (also the bottom) generally heat faster and to higher temperatures than the remaining particle surfaces.

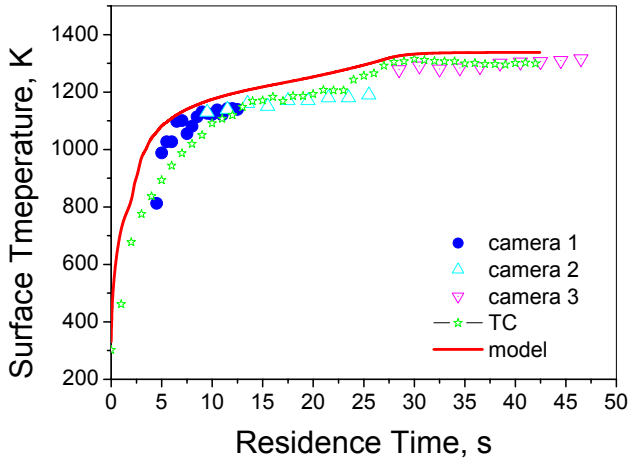

Figure 82 Particle surface temperature comparisons during pyrolysis in nitrogen – run 2
d_p = 9.5 mm, AR = 1.0, MC = 6 % (wt), T_w = 1373 K, T_g = 1050 K

Three-dimensional rendering of these surface temperatures provides uniquely detailed data regarding combustion processes. To generate such renderings, the particle surface temperature distribution is mapped onto two-dimensional images, as illustrated in Figure 83. This figure illustrates data from a single residence time and for a near-spherical poplar particle suspended in the single-particle reactor with an average particle surface temperature of 1312 K, approaching the end of particle devolatilization.

Particle surface and flame temperature distributions have also been measured and mapped to 2-D images for burning char particles, illustrated in Figure 84 to Figure 86.

Figure 84 shows the flame temperature distribution when volatiles burn next to the particle during devolatilization. The average temperature of the flame is about 2200 K. In Figure 85, both the images of the char particle and the flame next to the particle appear in one frame, and the flame temperature and particle surface temperature are calculated and mapped simultaneously. Obviously, the average temperature of the flame zone is much

higher than that in the particle surface zone, i.e., during devolatilization the particle surface remains at a lower temperature than the surrounding flame. A char particle surface temperature map for a burning char particle appears in Figure 86.

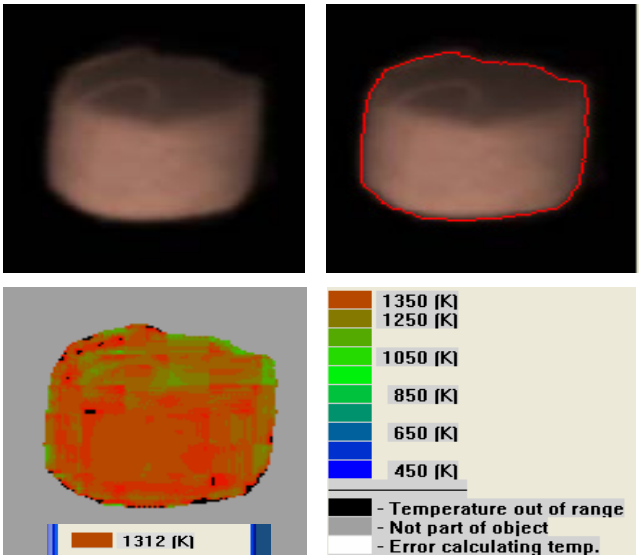

Figure 83 Poplar particle surface temperature during pyrolysis in nitrogen in a single-particle reactor
d_p = 9.5 mm, AR = 1.0, MC = 6 % (wt), T_w = 1373 K, T_g = 1050 K

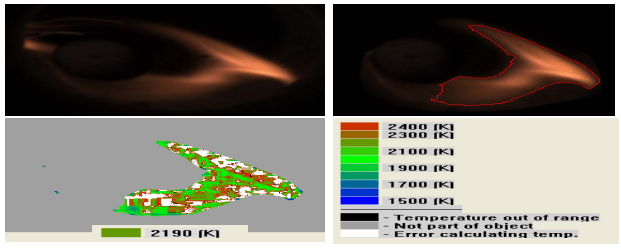

Figure 84 Flame temperature map during volatile combustion
d_p = 9.5 mm, AR = 1.0, MC = 6 % (wt), T_w = 1273 K, T_g = 1050 K

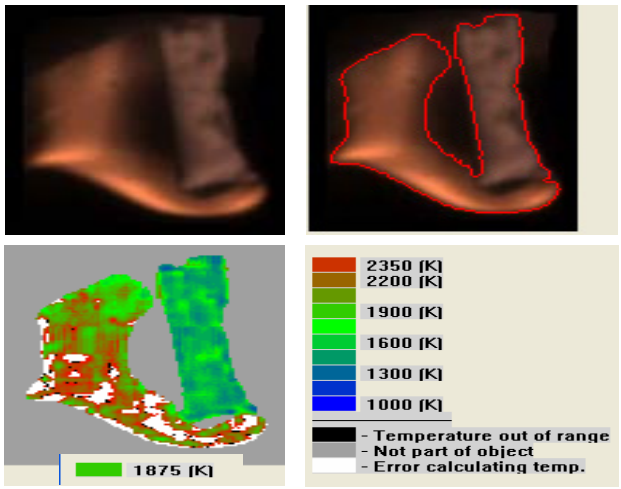

Figure 85 Char particle surface temperature and flame temperature map during particle devolatilization process
d_p = 9.5 mm, AR = 4.0, MC = 6 % (wt), T_w = 1273 K, T_g = 1050 K

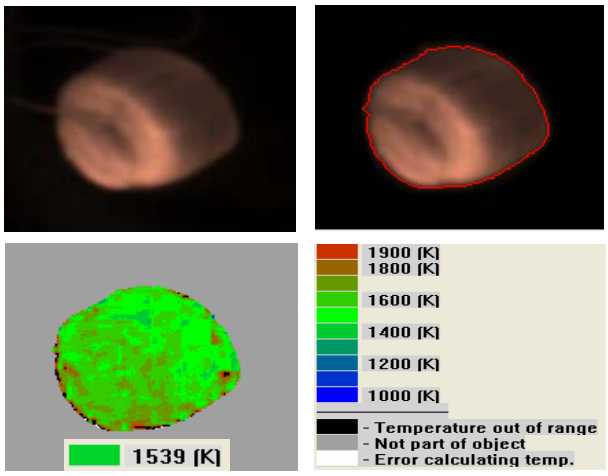

Figure 86 Char particle surface temperature map during char burning in air
d_p = 9.5 mm, AR = 1.0, MC = 6 % (wt), T_w = 1273 K, T_g = 1050 K

Char particle surface temperature was also measured as a function of time during the char burning process with the multi-color band camera pyrometer and compared with thermocouple measured data and model predictions in Figure 87. The camera-measured temperatures exceed the measured center temperatures and the predicted and measured

surface temperatures by about 100-200 K. The oxidizing and receding char surface precludes reliable surface temperature data from thermocouples. There are several complications in these temperature measurements. The optical measurements are potentially impacted by soot emission from the surrounding flame while the thermocouple data are potentially impacted from conduction along the wire during devolatilization. The camera-measured data could be also scattered due to the non-uniformity of temperature distribution on the particle surface. However, no definitive method of separating flame interference from particle surface temperature data appears to exist. Nevertheless, the data, although potentially biased, still provide some insight into the particle combustion behavior.

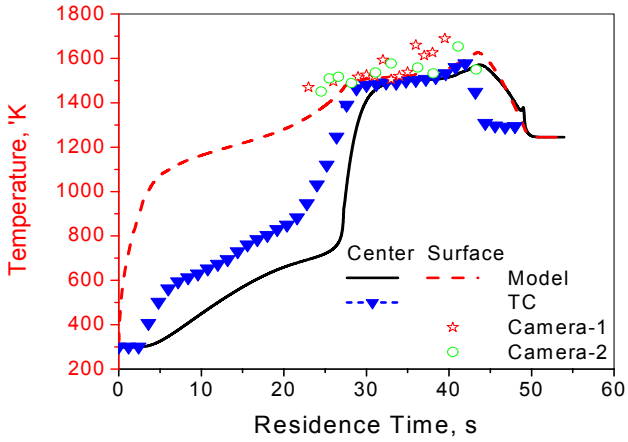

Figure 87 Char particle surface temperature as function of time during combustion in air
d_p = 9.5 mm, AR = 1.0, T_w = 1273 K, T_g = 1050 K

With the three camera pyrometers installed around the reactor, three images of a burning char particle were taken simultaneously from three orthogonal directions. The

particle surface temperature from each angle was calculated individually for each image. The 3-D particle shape, reconstructed with the three images as previously described, combines with the particle surface temperature distribution data to provide spatially and temporally resolved 3-D particle data, as shown in Figure 88.

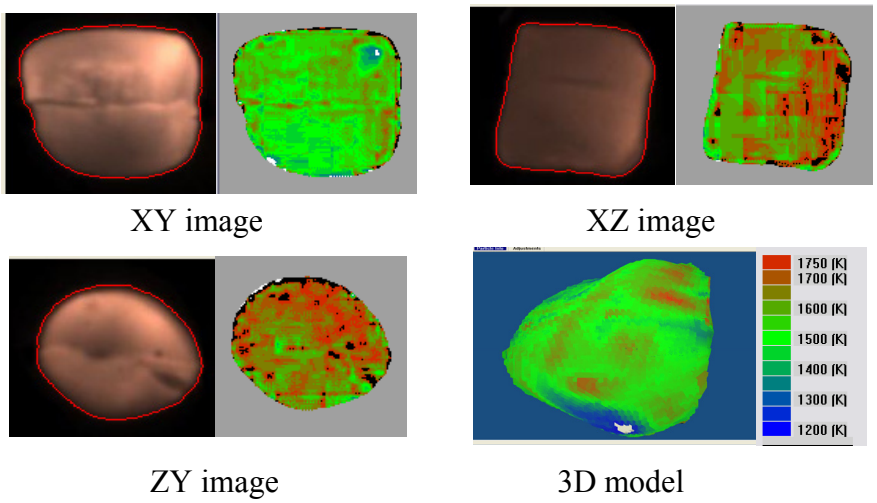

Figure 88 3-D particle surface temperature map of a burning char particle
d_p = 9.5 mm, AR = 1.0, MC = 6 % (wt), T_w = 1273 K, T_g = 1050 K

The above time-resolved model predictions, thermocouple-measured and camera-measured temperature data, and the 3-D particle surface temperature distribution data indicate that the 1-D particle combustion model captures the major behavior of a particle during combustion, but a 2-D or 3-D particle model can potentially improve the predictions for large particles with irregular shapes.

6.4. Modeling Studies

Pyrolysis and combustion of small sawdust particles and large poplar particles are further investigated with the single particle combustion model.

6.4.1. Composition Gradients and Effects of Particle Shape and Size on Volatile Yields

The composition gradients inside the near-spherical particle are predicted using the model, as shown in Figure 89. Both the biomass density and the char density changes are illustrated at the particle center and surface boundary.

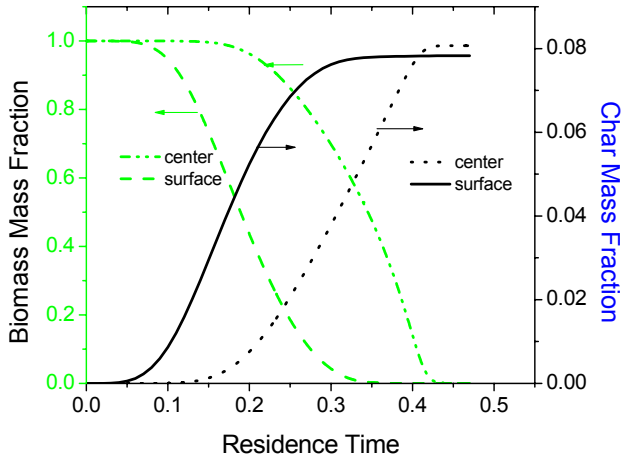

Figure 89 Predicted composition of the near-spherical particle as functions of time $d_{p,eq.}$ = 0.32 mm, AR = 1.6, reactor wall temperature and gas temperature see Figure 70

The effects of particle shapes and sizes on volatile yields are investigated using the model. As shown in Figure 90, the volatile yield of near-spherical particles decreases with increasing particle size. Both the experimental data and model predictions show that the near-spherical particles yield slightly lower volatiles relative to the other shapes. This is caused by a combination of different particle temperature histories due to the particle shape and longer average path lengths for tars to travel in spherical particles compared to their aspherical counterparts. Both flake-like and cylinder-like particles behavior similarly. However, the difference between the near-spherical and other shapes increases with increasing size.

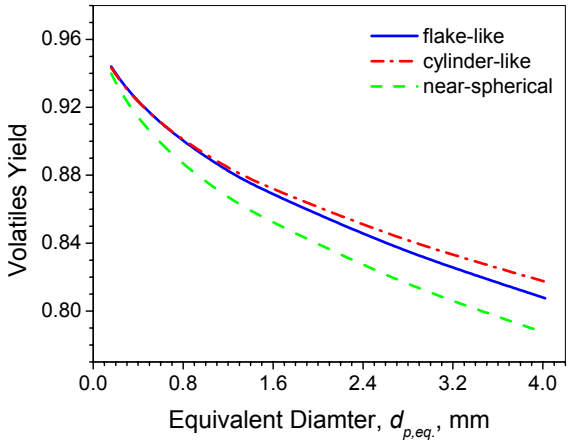

Figure 90 Predicted volatile yields comparison of various particle shape and size Reactor wall temperature and gas temperature see Figure 70

6.4.2. Effects of Blowing on Particle Temperature

During pyrolysis, the blowing factor of the 9.5 mm particle becomes as low as 0.1, as shown in Figure 91. This pronounced impact on heat transfer is not observed when radiation dominates particle, as illustrated by the predicted temperature profiles of a biomass particle in the single-particle reactor with and without blowing factor correction in Figure 92, where the particle heating history were nearly not influenced by the blowing effects correction. However, for environments dominated by convective heating, the blowing factor has a major impact on overall heat transfer rates, and the blowing factor slows down the particle pyrolysis process by about 20 %, as indicated in Figure 93.

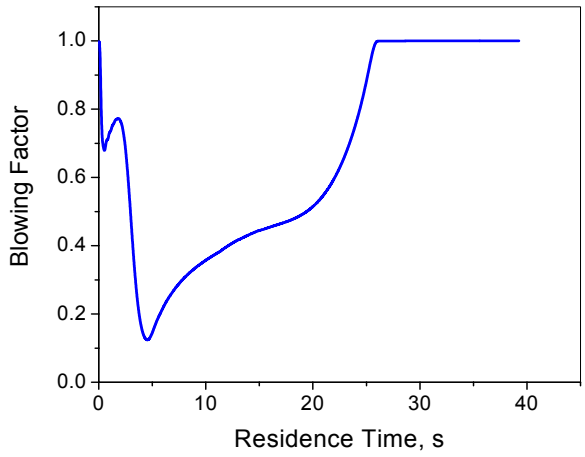

Figure 91 Blowing factor during particle pyrolysis process in nitrogen
d_p = 9.5 mm, AR = 1.0, MC = 6 % (wt), T_w = 1273 K, T_g = 1050 K

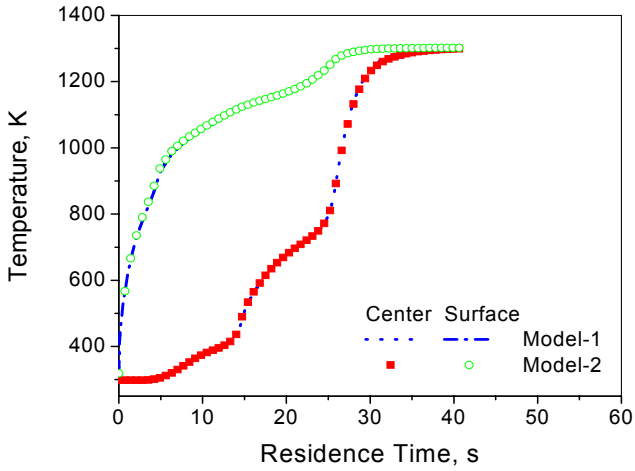

Figure 92 Particle temperature profile during particle pyrolysis in nitrogen with and without blowing factor correction
Model-1 with blowing factor correction and model-2 without blow factor correction; d_p = 9.5 mm, AR = 1.0, MC = 6 % (wt), T_w = 1303 K, T_g = 1050 K

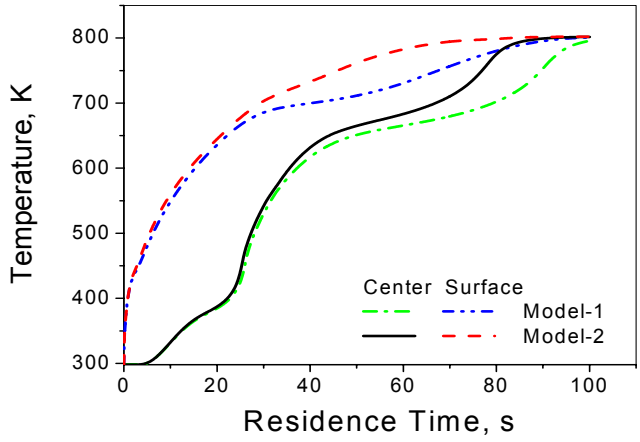

Figure 93 Effects of blowing factor on particle temperature during pyrolysis in nitrogen when convection dominates
Model-1 with blowing factor correction and model-2 without blow factor correction; d_p = 9.5 mm, AR = 1.0, MC = 6 % (wt), T_w = 298 K, T_g = 1400 K

6.4.3. Temperature, Pressure, and Species Concentration Profiles

The complete combustion of poplar particles has been further comprehensively investigated using the single particle combustion model. An 9.5 mm near-spherical poplar particle forms the basis for illustrating the predictions. Experimental verification for most of the information illustrated in this section is beyond the scope of this project, though some of it in principle could be accomplished with the facilities developed and described earlier.

Combustion modeling results for a particle with 6 %(wt) of moisture content show that after the particle enters hot gas and wall radiation, moisture starts to evaporate immediately, shown in Figure 94. Biomass begins to pyrolyze after about 3 seconds and the char mass ratio (with respect to the original particle mass) increases with increasing pyrolysis. The char mass ratio peaks slightly prior to the end of pyrolysis, with the latter occurring at about 20 seconds. Usually for this poplar particle, its char yield can be as

high as 10 % (wt) (with respect to the original wet particle mass) in inert gas, but here it shows the maximum char yield is only about 7 %(wt). This is caused by the overlap of the three processes; drying, pyrolysis, and char burning occurs simultaneously for this large size particle.

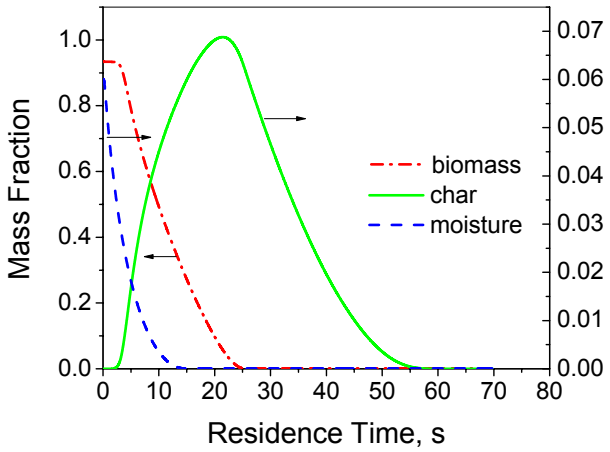

Figure 94 Predicted mass fraction of each species as functions of time
d_p = 9.5 mm, AR=1.0, MC = 6 % (wt), T_w = 1273 K, T_g = 1050 K

Particle and gas temperature profiles for a particle with higher (40%) moisture content appear in Figure 95 and Figure 96, where the abscissa indicates the relative distance from the center of the particle to the infinity boundary. The sizes of both the particle and boundary layer zone change during combustion. Figure 95 indicates that most of the particle remains at subboiling temperatures when volatiles ignite and form a flame surrounding the particle in the boundary layer. Strong temperature gradients exist between the drying and devolatilization zones in the particle. The maximum flame temperature can reach about 2400 K in this simulation (furnace wall temperatures 1276 K). During char burning, the flame shifts close to the particle surface as the blowing

effect decreases. The temperature gradient in the particle also flattens during char oxidation, as shown in Figure 96.

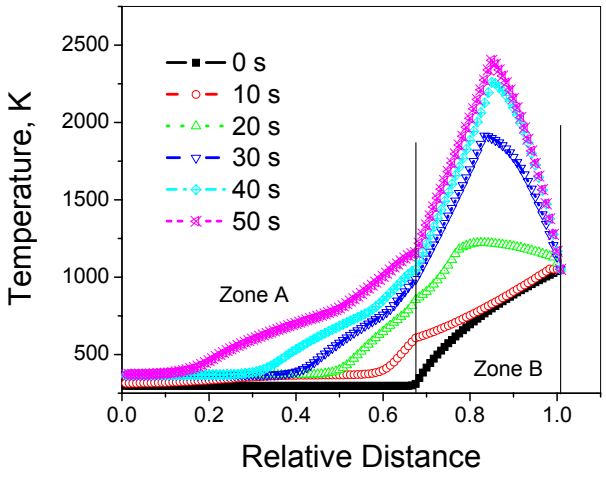

Figure 95 Temperature distributions during drying and pyrolysis in air
Zone A is particle solid domain and Zone B is the flame zone; d_p = 9.5 mm, *AR*=1.0, *MC* = 6 % (wt), T_w = 1273 K, T_g = 1050 K

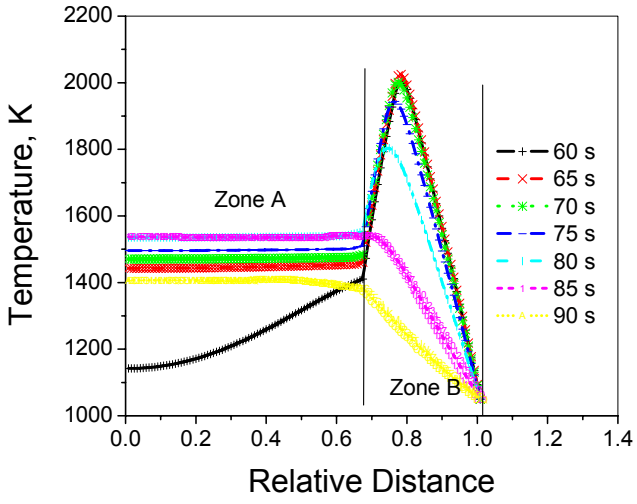

Figure 96 Temperature distributions during char burning in air
Zone A is particle solid domain and Zone B is the flame zone; d_p = 9.5 mm, *AR*=1.0, *MC* = 6 % (wt), T_w = 1273 K, T_g = 1050 K

The modeled particle radius, boundary layer thickness, and off-gas velocity as functions of residence time during the drying, devolatilization, and char burning processes appear in Figure 97.

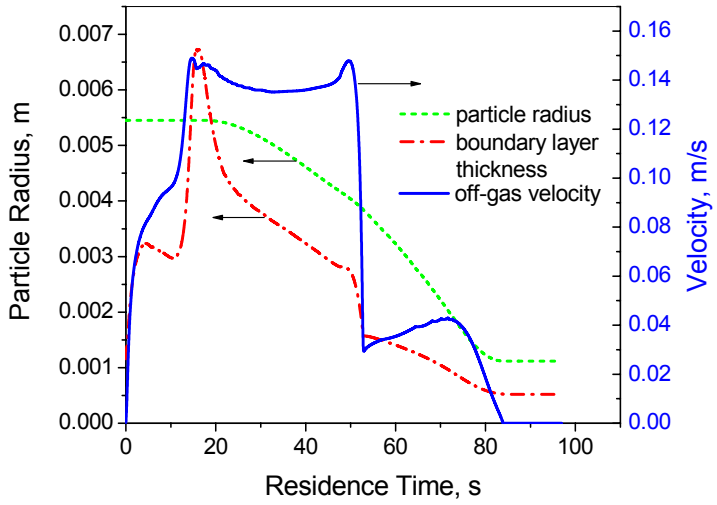

Figure 97 Particle radius, boundary layer thickness, and off-gas velocity during a wet particle combustion process in air
d_p = 9.5 mm, AR=1.0, MC = 6 % (wt), T_w = 1273 K, T_g = 1050 K

Although the three processes of drying, devolatilization, and char oxidation occur simultaneously for large particles such as the 11 mm poplar particle used in this investigation, they can still be approximately identified from both experimental data and model predictions, as shown in Figure 66 and Figure 97. Drying mainly finishes in the first 20 seconds followed by primary devolatilization that lasts about 30 seconds; char oxidation requires an additional 30 seconds. The modeling results also show that the particle shrinks slightly during drying and shrinks more rapidly during char burning.

The pressure profile in the particle during drying and the first half of devolatilization appears in Figure 98. The particle pressure of the inner part first starts to drop due to vapor recondensation during drying, and then it increases as devolatilization begins at the

outer layer of the particle. The particle pressure continues increasing through the end of the particle devolatilization. When the particle devolatilization is almost finished, the particle pressure drops but does not reach atmospheric pressure until the completion of char burning, as illustrated in Figure 99.

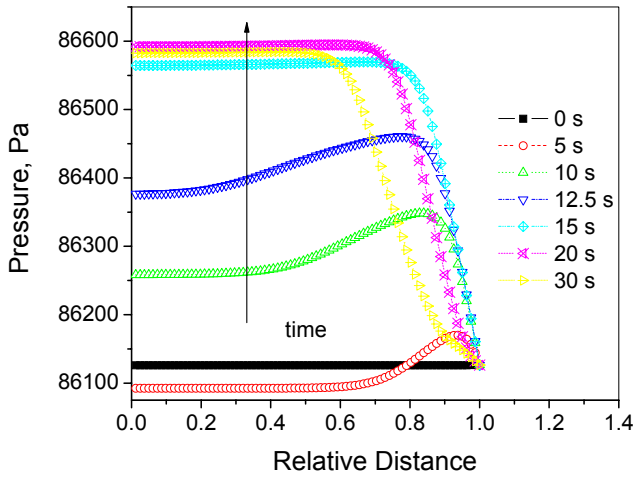

Figure 98 Particle pressure distribution during drying and first half of devolatilization
d_p = 9.5 mm, AR=1.0, MC = 6 % (wt), T_w = 1273 K, T_g = 1050 K

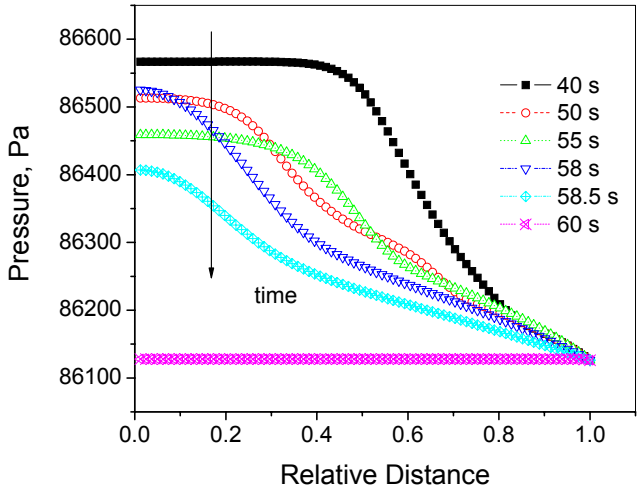

Figure 99 Particle pressure distribution at the end of devolatilization
d_p = 9.5 mm, AR=1.0, MC = 6 % (wt), T_w = 1273 K, T_g = 1050 K

The species concentrations profiles for several major species provide additional insight. The free water concentration profiles inside the particle as functions of time appear in Figure 100. When free water in the outer layer starts to evaporate, moisture in the gas phase diffuses both directions and the free water density in the inner layer starts to increase due to the vapor recondensation since the inner part of the particle remains at a low temperature.

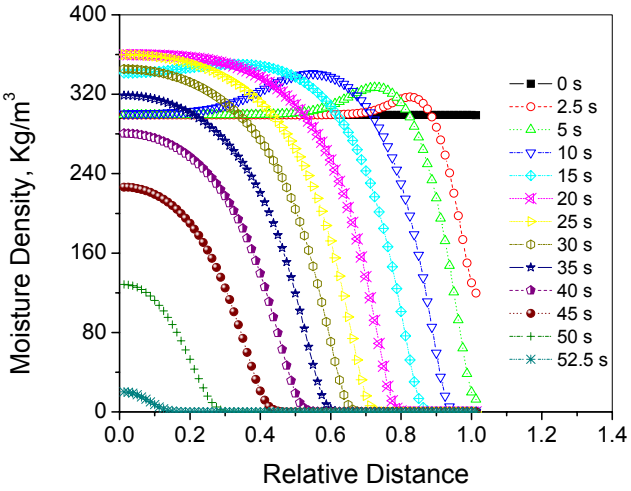

Figure 100 Free water concentration profiles during drying
d_p = 9.5 mm, AR=1.0, MC = 6 % (wt), T_w = 1273 K, T_g = 1050 K

The concentration profiles of the other two solid species at different residence times appear in Figure 101 and Figure 102. The pyrolysis front moves from the outer layer to the particle center with increasing time and a monotonic decrease in biomass (as opposed to char) concentration. The pyrolysis front is steep, reasonably approaching a step function through most of the particle history.

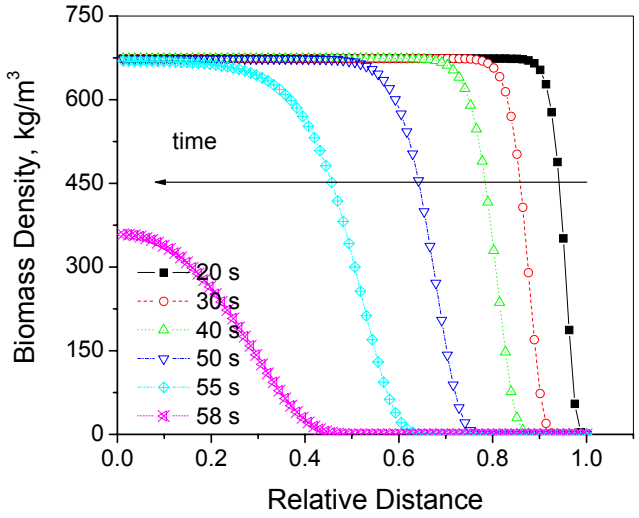

Figure 101 Biomass concentration profile at different residence time
d_p = 9.5 mm, AR=1.0, MC = 6 % (wt), T_w = 1273 K, T_g = 1050 K

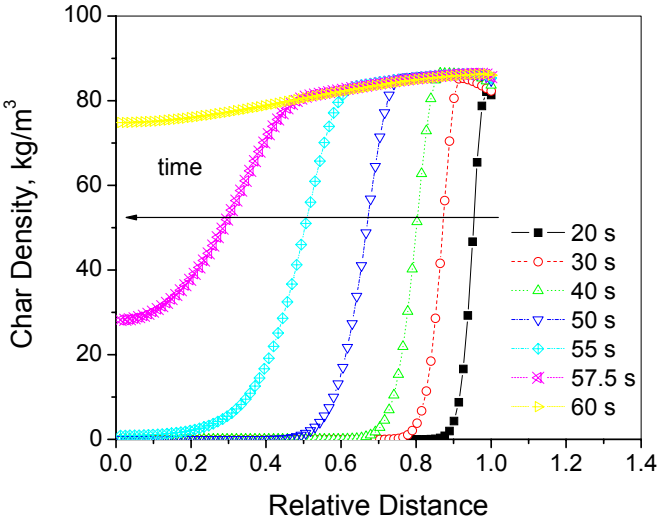

Figure 102 Char concentration profile at different residence time
d_p = 9.5 mm, AR=1.0, MC = 6 % (wt), T_w = 1273 K, T_g = 1050 K

Figure 103 is the concentration distribution of hydrocarbon gases and oxygen during devolatilization process. The flame position in the boundary layer corresponds to the location where these two profiles simultaneously approach zero.

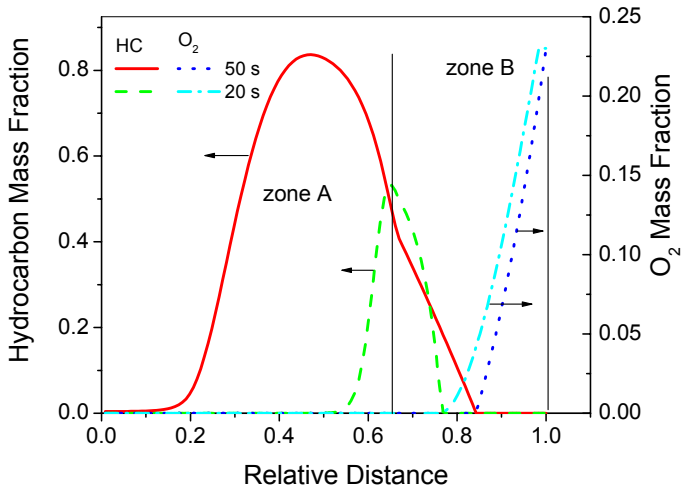

Figure 103 Hydrocarbon gases and oxygen profiles during devolatilization
Zone A is particle solid domain and Zone B is the flame zone; d_p = 9.5 mm, AR=1.0, MC = 6 % (wt), T_w = 1273 K, T_g = 1050 K

The concentration profiles of carbon monoxide and oxygen during char burning appear in Figure 104.

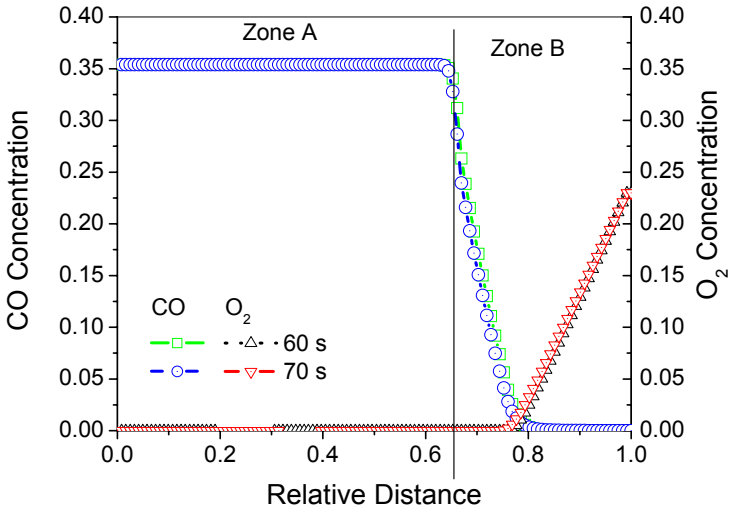

Figure 104 CO and oxygen concentration during char burning in air
Zone A is particle solid domain and Zone B is the flame zone; d_p = 9.5 mm, AR=1.0, MC = 6 % (wt), T_w = 1273 K, T_g = 1050 K

The oxidizer is nearly consumed before it reaches the surface of the char particle, and the oxidation rate of the char particle is diffusion controlled. These O2 and CO concentration profiles are similar to what predicted by a two-film model explained in (Turns, 2000) for coal char particle combustion.

6.4.4. Preliminary Black Liquor Combustion Simulation

The single particle combustion model has been used to preliminarily model combustion of a 3.3 mm black liquor droplet. The black liquor droplet has 30%(wt) moisture content and 15%(wt) inorganic material. In this simulation, inorganic material is assumed to be inert, and no smelt reactions are considered – a poor assumption that will be relaxed later by other students working in this area. The same conditions as the biomass combustion are used with a wall temperature of 1273 K and a bulk gas temperature of 1050 K. The swelling and mass loss of the particle during drying and devolatilization appear in Figure 105.

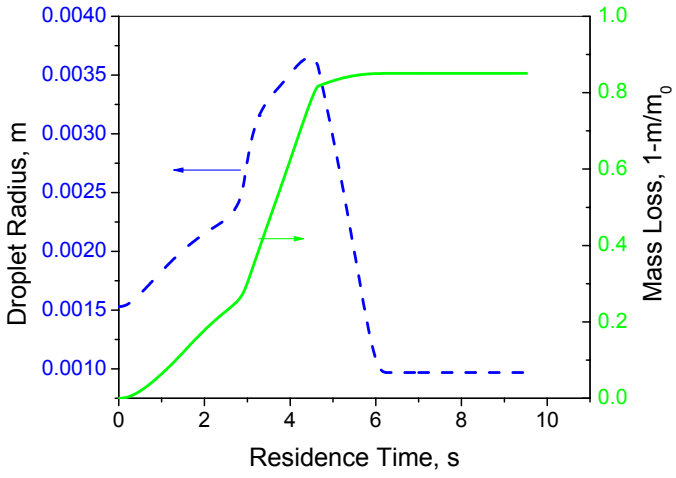

Figure 105 Predicted mass loss and swelling of a black liquor droplet during combustion in air
d_p=3.3 mm, MC = 30 % (wt), T_w = 1273 K, T_g = 1050 K

Modeling results show that the droplet starts to swell during drying and reaches a peak value at the end devolatilization. The swelling ratio is about 2.5. The droplet shrinks dramatically during the char burning stage. The modeled particle surface temperature and center temperature appear in Figure 106.

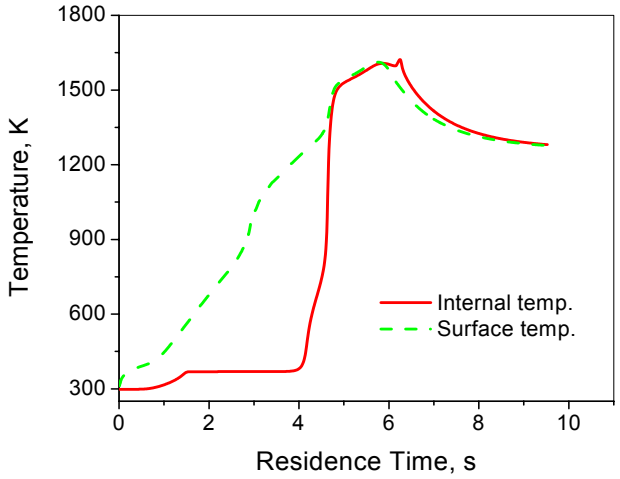

Figure 106 Predicted black liquor temperatures as function of time during combustion in air
d_p=3.3 mm, MC = 30 % (wt), T_w = 1273 K, T_g = 1050 K

Similar predictions for particle of various shapes and sizes qualitatively indicate the same behavior as those illustrated for near-spherical particles.

6.5. Combustion of Wheat Straw

In this project, knees and stalks of wheat straw were also burned in the single-particle reactor. Mass loss data as function of residence time were recorded for both knees and stalks. Results indicate that stalks burn about three times faster than knees due to the larger surface area and lower particle density of stalks than those of knees, as shown in Figure 107.

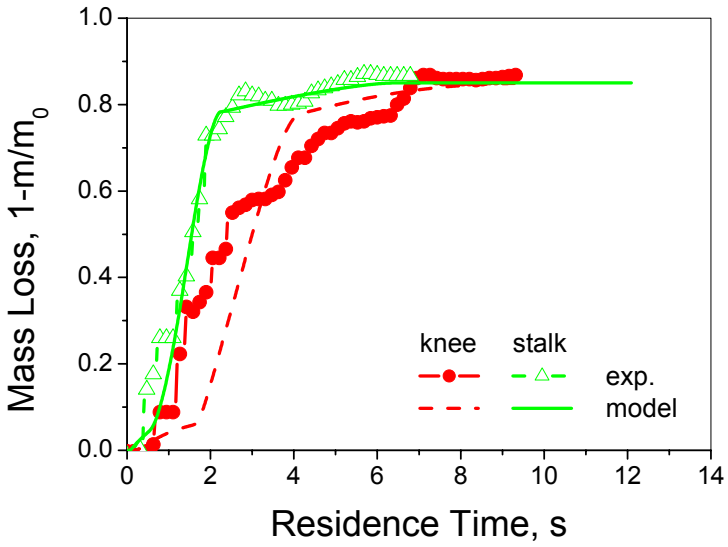

Figure 107 Mass loss of wheat straw knee and stalk during combustion in air
d_p = 4 mm, T_w = 1123 K, T_g = 1023 K

With such substantial difference in combustion rate demonstrated in Figure 107, biomass fuels similar to straw may have to be treated separately for knees and stalks when modeling their combustion behavior in boiler.

6.6. Summary

In this chapter, experimental data, including particle temperature and mass loss, for sawdust particle samples and poplar dowel particle samples of different shape and size were presented. The single particle combustion model was validated using experimental data collected in the single-particle reactor and the entrained-flow reactor.

Biomass particle combustion including drying, devolatilization, and char burning and were studied both experimentally and theoretically using two reactors and a single particle combustion model. The effects of solid particle shape and size on particle

combustion reactivity were studied and discussed based on experimental data and modeling results.

Effect of particle density on combustion rate was also demonstrated with experimental data collected with wheat straw knees and stalks.

7. Conclusions and Recommendations

7.1. Accomplishments

In this project, experimental data and a single particle combustion model was developed to describe drying, devolatilization, and char oxidation of biomass particles of varied shape and size. Experimental data were collected in both an entrained-flow reactor and a single-particle reactor. Particle surface and flame temperature were measured with a color-band imaging pyrometry developed and applied in the investigation. Particle volumes and surface areas of irregular particles were measured with a particle shape reconstruction algorithm developed in this investigation. The last two diagnostics represent the first-ever application of such tools to particle combustion experiments.

Accomplishements from each part of this project are as follows:

- A single particle combustion model has been developed.

  A relatively general purpose particle combustion model capable of simulating drying, recondensation, devolatilization, and char oxidation and gasification, and swelling/shrinking as well as gas-phase combustion surrounding biomass particles was developed to compare with original data. Comparisons were made of particle center and surface temperatures and overall mass loss. Model predictions included many additional features of biomass combustion less amenable to direct measurement.

- An entrained-flow reactor was designed and built.

  An entrained-flow reactor designed, constructed, and used in this project provided unique access to combustion characterization of aspherical particles. The combustor provided optical access at three levels in three orthogonal directions. A particle residence time of up to 2 seconds was obtained in this reactor. The reactor provided a maximum wall temperature of 1600 K. An imaging system associated with this reactor provided raw data that, when combined in alorgithms described below, captured three-dimensional combustion features of aspherical particles.

- A color-band pyrometry was developed and successfully applied to measure particle surface and flame temperature.

  A color-band pyrometry was developed based on CCD/CMOS digital cameras. Particle surface temperature and flame temperature measurements generally agreed with thermocouple measurements and model predictions when artifacts from each were removed, although small differences were observed between predictions and measurements. This new diagnostic provides pixel-by-pixel particle (and flame) temperature and emissivity data from widely available and relatively inexpensive cameras. Depending on magnification, shutter speed, etc., useful temperature and emissivity data were obtained at temperatures greater than about 750 K, with the lower limit based on signal intensity. Cameras more sensitive in the infrared produced useful data at lower temperatures.

  These non-contact particle temperature data compared reasonably well with both predicted and thermocouple measurements for both suspended and entrained-flow systems. The images allowed three-dimensional reconstruction of particle

temperature profiles that revealed large spatial differences in particle surface temperature – a feature that cannot be captured in one-dimensional transient models of any complexity. This investigation represents the first-ever development or application of this technique to particle combustion investigations.

- A particle shape reconstruction algorithm was developed to measure particle external surface area and volume for particles with irregular shape.

  An algorithm was developed which reconstructs a three dimensional representation of a particle based on three orthogonal profiles of the particle shape. Coordinates of six extreme points were determined based on the orientation of the images, and points on the particle surface were interpolated with the inverse distance weighting method. The average error of this algorithm was about 10% based on measurement of the surface area and volume of a piece of rock with irregular shape. This investigation represents the first-ever development or application of this technique to particle combustion investigations.

- Particle shape and size impact fuel reactivity substaneously.

  A comprehensive data set of biomass particle reaction was obtained as a function of sample shape, size, and composition with the entrained-flow reactor and the single-particle reactor, the color-band pyrometer, and the particle reconstruction algorithm. The single particle combustion model provided a theoetical basis for analyzing the experimental results.

7.2. Principal Conclusions

Both experimental and theoretical investigations indicated that particle shape and size both impact overall particle reactivity. Experiments conducted on biomass particles at relevant temperatures and a variety of well-characterized shapes indicate that particle shape impacts overall reaction rates relative to those of spheres with the same mass/volume by factors of two or more at sizes and shapes of commercial relevance. Data and theoretical models indicate that the impact of shape increases with increasing size and increasing asphericity and is large at sizes relevant to biomass utilization in industry. Generally speaking, spherical mathematical approximations for fuels that either originate in or form aspherical shapes during combustion poorly represent combustion behavior when particle size exceeds a few hundred microns. This includes a large fraction of the particles in both biomass and black liquor combustion.

Shape impacts on combustion also influence overall conversion times by factors of two to three, depending on size and combustion conditions. In particular, composition and temperature gradients in particles strongly influence the predicted and measured rates of temperature rise and combustion, with large particles reacting more slowly than is predicted from isothermal models.

The data and model developed in this investigation describe single-particle biomass combustion rates reasonably well. Generally agreement within a few percent of the measured values is achieved, though in most cases there remain generally small but statistically signficant differences between predictions and measurements. However, relative to the factors of 2 or more errors associated with isothermal, spherical, or other common assumptions, this investigation provides substantial improvement in predicting biomass behavior. Most of the remaining difference between measurement and

predictions may be related to uncertainties in physical properties, experimental artifacts, or model assumptions inherent in this approach (see below).

7.3. Recommendations

The model developed in this investigation provides detailed predictions of biomass combustion behavior. However, the data suggest some features of biomass combustion that require fundamentally different modeling approaches. For example, the three-dimensional reconstruction of shape and size routinely show that large or aspherical particle combustion (and possibly small particle combustion) is at least two dimensional. Particle reaction rates and temperatures differ markedly at different regions on the particle surface, a feature that cannot be resolved with a one-dimensional model of any complexity. This also suggests that the conceptual model of char oxidation, for example, may be fundamentally flawed. It is possible (likely in the cases investigated here) that oxidation does not occur by oxygen diffusion to the surface and product diffusion back to the bulk along similar paths, but rather by oxygen diffusion/convection to one side of the particle (typically the windward side) and product diffusion/convection to the bulk gas from a separate region (typically the leeward side). This fundamentally changes concepts of diffusion limitations, maximum burning rates, temperature profiles, and peak particle temperatures during combustion. Further investigation of this phenomenon is highly recommended.

Many of the diagnostics innovated and demonstrated here have much greater potential application than has been exploited for this investigation. The color-band temperature measurement and the particle shape reconstruction techniques, as well and the reactors, are highly versatile instruments that can be applied to many investigations in

and out of combustion. These are being pursued by colleagues in several contexts but could be developed much further in many areas.

The particle model described here could make essential contributions to combustion simulators. While the efficiency of the current code increased dramatically as part of this investigation, it still may not be (probably is not) sufficiently efficient to incorporate into such codes. Efforts currently underway by colleagues to increase the efficiency could make these results much more useful. In a related matter, the C++ coding of this model is in general compliance with the coding standards of Larry Baxter's research group but could be improved significantly.

Finally, some of the predictions made by the particle model could be more thoroughly verified through additional experimentation. Specifically, the particle and gas composition data predicted by the code possibly could be verified by creative particle characterization and in situ gas characterization techniques. Such verification would prove useful in extending the validation beyond temperature and mass loss data.

8. References

Abreu, H. D. S., A. M. D. Nascimento and M. A. Maria, "Lignin structure and Wood Properties," *Wood and Fiber Science*, **31**, (4): 426-433 (1999).

Adanez, J., L. F. de Diego, F. Garcia-Labiano, A. Abad and J. C. Abanades, "Determination of Biomass Char Combustion Reactivities for FBC Applications by a Combined Method," *Ind. Eng. Chem. Res.*, **40**, (20): 4317-4323 (2001).

Antal, M. J. J. and V. Gabor, "Cellulose Pyrolysis Kinetics: the Current State of Knowledge," *Ind. Eng. Chem. Res.*, **34**: 703-717 (1995).

Baxter, L. L., *Physical and combustion properties of biomass*, http://www.et.byu.edu /%7Elarryb/Biomass.htm, 2000.

Baxter, L. L., "Biomass-coal co-combustion: opportunity for affordable renewable energy," *Fuel*, **84**, (10): 1295-1302 (2005).

Baxter, L. L. and A. L. Robinson. Engineering Models of Biomass Combustion Processes. Biomass for Energy and Industry: 1st World Conference and Technology Exhibition, Seville, Spain (2000).

Bayer, B., *Bayer Color Filter*, http://en.wikipedia.org/wiki/Bayer_filter,

Bird, R. B., W. E. Stewart and L. E. N. Transport Phenomena. New York / Chichester / Weinheim / Brisbane / Singapore / Toronto, John Wiley & Sons, Inc. (2002)

Blackham, A. U., L. D. Smoot and P. Yousefi, "Rates of oxidation of millimetre-sized char particles: simple experiments," *Fuel*, **73**, (4): 602-612 (1994).

Bockaert, V., *Color Filter Array Sensor*, http://www.dpreview.com/learn/?/key=color +filter+array, 2003.

Bradbury, A. G. W., Y. Sakai and F. Shafizadeh, "A Kinetic Model for Pyrolysis of Cellulose," *Journal of Applied Polymer Science*, **23**: 3271-3280 (1979).

Brewster, B. S., S. C. Hill, P. T. Radulovic and L. D. Smoot. Fundamentals of Coal Combustion for Clean and Efficient Use. London, Elsevier Applied Science Publishers. (1993)

Broido, A., *Kinetics of Solid-Phase Cellulose Pyrolysis*, Thermal Uses and Properties of Carbohydrates and Lignins, New York, Academic Press, 19-35 (1976).

Broido, A. and M. A. Nelson, "Char Yield on Pyrolysis of Cellulose," *Combustion and Flame*, **24**: 263-268 (1975).

Bryden, K. M., Computational Modeling of Wood Combustion. Mechanical Engineering Department, University of Wisconsin-Madison. (1998)

Bryden, K. M. and M. J. Hagge, "Modeling the combined impact of moisture and char shrinkage on the pyrolysis of a biomass particle," *Fuel*, **82**: 1633-1644 (2003).

Chan, W.-C. R., M. Kelbon and B. B. Krieger, "Modeling and experimental verification of physical and chemical processes during pyrolysis of a large biomass particle," *Fuel*, **64**, (11): 1505-1513 (1985).

Chen, G., Q. Yu and K. Sjostrom, "Reactivity of Char from Pyrolysis of Birch Wood," *Journal of Analytic and Applied Pyrolysis*, **40-41**: 491-499 (1997).

Chen, Y. G., S. Charpenay, A. Jensen and M. A. Wojtowicz. Modeling of Biomass Pyrolysis Kinetics. Twenty-seventh Symposium (International) on Combustion / The Combustion Institute 1327-1334 (1998).

De Paiva Souza, M. E. and S. A. Nebra, "Heat and mass transfer model in wood chip drying," *Wood and Fiber Science*, **32**, (2): 153-163 (2000).

Demirbas, A., "Mechanism of Liquefaction and Pyrolysis Reactions of Biomass," *Energy Conversion & Management*, **41**: 633-646 (2000).

Demyirbas, A., "Hydrocarbons from Pyrolysis and Hydrolysis Processes of Biomass," *Energy Sources*, **25**: 67-75 (2003).

Di Blasi, C., "Analysis of convection and secondary reaction effects within porous solid fuels undergoing pyrolysis," *Combustion Science and Technology*, **90**: 315-340 (1993).

Di Blasi, C., "Heat, Momentum and Mass Transport through a Shrinking Biomass Particle Exposed to Thermal Radiation," *Chemical Engineering Science*, **51**, (7): 1121-1132 (1996a).

Di Blasi, C., "Kinetics and Heat Transfer Control in the Slow and Flash Pyrolysis of Solids," *Ind. Eng. Chem. Res.*, **35**: 37-46 (1996b).

Di Blasi, C., "Influences of Physical Properties on Biomass Devolatilization Characteristics," *Fuel*, **76**: 957-964 (1997).

Di Blasi, C., F. Buonanno and C. Branca, "Reactivities of Some Biomass Chars in Air," *Carbon*, **37**: 1227-1238 (1999).

DIPPR, *Design Institute of Physical Property Data*, Chemical Engineering Department, Brigham Young University, http://dippr.byu.edu/index.asp,

EIA, "Renewable energy annual 2002 with preliminary data for 2002," Washington, DC, (2003).

Epix Inc, *Spectral responsivity of ZR32112 CMOS sensor*, http://www.epixinc.com /products/ZR32112spectralresponsivity.pdf,

Evans, D. H. and H. W. Emmons, "Combustion of wood charcoal," *Fire Research*, (1): 57-66 (1977).

Evans, R. J. and T. A. Milne, "Molecular Characterization of the Pyrolysis of Biomass. 1. Fundamentals," *Energy & Fuels*, **1**, (2): 123-137 (1987a).

Evans, R. J. and T. A. Milne, "Molecular Characterization of the Pyrolysis of Biomass. 2. Applications," *Energy & Fuels*, **1**, (4): 311-319 (1987b).

Fletcher, T. H., A. R. Kertein, R. J. Pugmire and D. M. Grant, "Chemical Percolation Moddel for devolatilization. 3. Direct used of 13C NMR data to predict effects of coal type," *Energy & Fuels*, **6**, (4): 414-431 (1992).

Fletcher, T. H., H. R. Pond, J. Webster, J. Wooters and L. L. Baxer. Prediction of Tar and Light Gas during Pyrolysis of Black Liquor and Biomass. 3rd Annual Joint Meeting of the U.S. Sections of the Combustion Institute, Chicago, IL (2003).

Font, F., A. Marcilla, E. Verdu and J. Devesa, "Kinetics of the pyrolysis of almond shells and almond shells impregnated with CoCl2 in a fluidized bed reactor and in a pyroprobe 100," *Ind. Eng. Chem. Res.*, **29**: 1846-1855 (1990).

Forest Products Laboratory United States Department of Agriculture Forest Service, *Chapter 3, Physical Properties and Moisture Relations of Wood*, Wood Handbook: Wood as an Engineering Material, Madison, Wisconsin, Forest Products Society, 3-5 (1999).

Gronli, M. G. and M. C. Melaaen, "Mathematical model for wood pyrolysis - comparison of experimental measurements with model predictions," *Energy & Fuels*, **14**, (4): 791-800 (2000).

Guzenda, R. and W. Olek. Identification of free and bound water content in wood by means of NMR relaxometry. 12th International Symposium on Nondestructive Testing of Wood, Sopron, Hungary, **Vol.6 No.3** (3) (2000).

Hautman, D. J., L. Dryer, K. P. Schug and I. Glassman, "A multiple-step overall kinetic mechanism for the oxidation of hydrocarbons," *Combustion Science and Technology*, **25**: 219-235 (1981).

Horbaj, P., "Model of the Kinetics of Biomass Pyrolysis," *Drevarsky Vyskum*, **42**, (4): 15-23 (1997).

Incropera, F. P. and D. P. Dewitt. Fundamentals of Heat and Mass Transfer, John Wiley & Sons. (1996)

Ingle Jr., J. D. and S. R. Crouch, *Chapter 4. Optical Sources, Transducers, and Measurement Systems*, Spectrochemical Analysis, Upper Saddle River, New Jersey 07458, Prentice-Hall, Inc., 88 (1988).

Ip, L.-T., Comprehensive black liquor droplet combustion studies. Chemical Engineering, Brigham Young University. (2005)

Jalan, R. K. and V. K. Srivastava, "Studies on Pyrolysis of a Single Biomass Cylindrical Pellet Kinetic and Heat Transfer Effects," *Energy Conversion & Management*, **40**, (5): 467-494. (1999).

Janse, A. M. C., H. G. de Jonge, W. Prins and W. P. M. van Swaaij, "Combustion kinetics of char obtained by flash pyrolysis of pine wood," *Industrial & Engineering Chemistry Research*, **37**, (10): 3909-3918 (1998).

Janse, A. M. C., R. W. J. Westerhout and W. Prins, "Modelling of Flash Pyrolysis of a Single Wood Particle," *Chemical Engineering and Processing*, **39**: 239-252 (2000).

Jensen, A., K. Dam-Johansen, M. W. Wojtowicz and M. A. Serio, "TG-FTIR Study of Influence of Potassium Chloride on Wheat Straw Pyrolysis," *Energy & Fuels*, **12**: 929-938 (1998).

Kansa, E., J., H. E. Perlee and R. F. Chaiken, "Mathematical model of wood pyrolysis including internal forced convection," **29**, (3): 311-324 (1977).

Komatsu, K., "3-D shape reconstruction of human face from a 2-D facial image and provision for change of expression," *Systems and Computers in Japan*, **22**, (7): 63-74 (1991).

Koufopanos, C. A., G. Maschio and A. Lucchesi, "Kinetic Modelling of the Pyrolysis of Biomass and Biomass Components," *The Canadian Journal of Chemical Engineering*, **67**: 75-84 (1989).

Koufopanos, C. A., N. Papayannakos, G. Maschio and A. Lucchesi, "Modelling of the Pyrolysis of Biomass Particles. Studies on Kinetics, Thermal and Heat Transfer Effects,," *The Canadian Journal of Chemical Engineering*, **69**, (4): 907-915 (1991).

Kurdyumov, V. N. and E. Fernandez, "Heat transfer from a circular cylinder at low Reynolds numbers," *Journal of Heat Transfer, Transactions ASME*, **120**, (1): 72-75 (1998).

Kutulakos, K. N. and S. M. Seitz, "A theory of shape by Space Carving," *International Journal of Computer Vision*, **38**, (3): 199-218 (2000).

Lee, C. K., R. F. Chaiken and J. M. Singer, "Charring pyrolysis of wood in fires by laser simulation," *Symp (Int) on Combust, 16th, MIT, Aug 15-20 1976*: 1459-1470 (1976).

Liden, C. K., F. Berruti and D. S. Scott, "A kinetic model for the production of liquids from the flash pyrolysis of biomass," *Chemical Engineering Communications*, **65**: 207-221 (1988).

Liliedahl, T. and K. Sjostrom, "Heat transfer controlled pyrolysis kinetics of a biomass slab, rod or sphere," *Biomass and Bioenergy*, **15**, (6): 503-509 (1998).

Lu, H., W. Robert, L. Werret, G. Peirce and L. L. Baxter. Comprehensive study of biomass particle combustion. 31st International Symposium on Combustion Heidelberg, Germany (submitted). (2006)

Mann, M., *A Comparison of the Environmental Consequences of Power from Biomass, Coal, and Natural Gas*, NREL, http://www.nrel.gov/analysis/pdfs/ 2001/nov_dc.pdf, 2001.

Masliyah, J. H. and N. Epstein, "Numerical solution of heat and mass transfer from spheroids in steady axisymmetric flow," *Prog. Heat Mass Transfer*, **6**: 613-632. (1972).

Mermoud, F., F. Golfier, S. Salvador, L. Van de Steene and J. L. Dirion, "Experimental and numerical study of steam gasification of a single charcoal particle," *Combustion and Flame*, **145**: 59-79 (2006).

Merrick, D., "Mathematical models of the thermal decomposition of coal - 2. Specific heats and heats of reaction," *Fuel*, **62**, (5): 540-546 (1983).

Miller, R. S. and J. Bellan, "Analysis of Reaction Products and Conversion Time in the Pyrolysis of Cellulose and Wood Particles," *Combustion Science and Technology*, **119**: 331-373 (1996).

Miller, R. S. and J. Bellan, "A Generalized Biomass Pyrolysis Model Based on Superimposed Cellulose, Hemicellulose and Lignin Kinetics," *Combustion Science and Technology*, **126**: 97-137 (1997).

Niksa, S. Predicting the rapid devolatilization of diverse forms of biomass with bio-FLASHCHAIN. 28th International Symposium on Combustion, Edinburgh, United Kingdom, **28** 2727-2733 (2000).

Northey, B., *Wood Chemistry*, http://depts.washington.edu/pse406/40inter.htm, 1998.

Nunn, T. R., J. B. Howard, J. P. Longwell and W. A. Peters, "Product compositions and kinetics in the rapid pyrolysis of sweet gum hardwood," *Industrial & Engineering Chemistry, Process Design and Development*, **24**, (3): 836-844 (1985).

Olek, W., P. Perre and J. Weres, "Inverse analysis of the transient bound water diffusion in wood," *Holzforschung*, **59**, (1): 38-45 (2005).

Orfao, J. J., F. J. A. M. Antunes and J. L. Figueiredo, "Pyrolysis Kinetics of Lignocellulosic Materials, Three Independent Reactions Model," *Fuel*, **78**: 349-358 (1999).

Ouelhazi, N., G. Arnaud and J. P. Fohr, "A Two-dimensional study of wood plank drying. The effect of gaseous pressure below boiling point," *Transport in Porous Media*, **7**, (1): 39-61 (1992).

Patankar, S. V. Numerical Heat Transfer and Fluid Flow, Taylor & Francis. (1980)

Raveendran, K., A. Ganesh and K. C. Khilar, "Pyrolysis Characteristics of Biomass and Biomass Components.," *Fuel*, **75**, (8): 987-998 (1996).

Raveendran, K., A. Ganesh and K. C. Khilart, "Influence of Mineral Matter on Biomass Pyrolysis Characteristics," *Fuel*, **74**, (12): 1812-1822 (1995).

Roberts, W., Personal Communication, 2005.

Robinson, A. L., S. G. Buckley and L. L. Baxter, "Thermal Conductivity of Ash Deposits 1: Measurement Technique," *Energy & Fuels*, **15**: 66-74 (2001a).

Robinson, A. L., S. G. Buckley, N. Y. C. Yang and L. L. Baxter, "Thermal Conductivity of Ash Deposits 2: Effects of Sintering," *Energy & Fuels*, **15**: 75-84 (2001b).

Saaddjian, E., N. Midoux, M. I. Gastou Chassaing, J. C. Leprevost and J. C. Andre, "Chaotic mixing and heat transfer between confocal ellipses: experimental and numerical results," *Phys. Fluids*, **8**, (3): 677-691 (1996).

Saito, H. and T. Kanade, "Shape reconstruction in projective grid space from large number of images," *Proceedings of the 1999 IEEE Computer Society Conference on Computer Vision and Pattern Recognition (CVPR'99)*, **2**: 49-54 (1999).

Siegel, R. and J. Howell, *Chapter Six - Radiation exchange in enclosures composed of black and/or diffuse-gray surfaces*, Thermal radiation heat transfer, Taylor & Francis, (2002).

Smith, K. L., L. D. Smoot, T. H. Fletcher and R. J. Pugmire. The structure and reaction processes of coal. New York and London, Plenum Press. (1994)

Smoot, L. D. and P. J. Smith. Coal Combustion and Gasification. New York, Plenum Press. (1985)

Sony Inc, *ICX285AQ CCD sensor spectral responsivity*, http://products.sel.sony.com/semi/PDF/ICX285AQ.pdf, 2005.

Stenius, P. Forest Products Chemistry, Fapet Oy. (2000)

Thunman, H., F. Niklasson, F. Johnsson and B. Leckner, "Composition of Volatile Gases and Thermochemical Properties of Wood for Modeling of Fixed or Fluidized Beds," *Energy & Fuels*, **15**: 1488-1497 (2001).

Turns, S. R. An Introduction to Combustion: Concepts and Applications, Thomas Casson. (2000)

Wagenaar, B. M., W. Prins and W. P. M. Van Swaaij, "Flash pyrolysis kinetics of pine wood," *Fuel Processing Technology*, **36**: 291 (1993).

Warnatz, J., "Hydrocarbon oxidation high-temperature chemistry," *Pure Appl. Chem.*, **72**, (11): 2101-2110 (2000).

Williams, P. T. and P. A. Horne, "Role of Metal Salts in the Pyrolysis of Biomass," *Renewable Energy*, **4**, (1): 1-13 (1994).

Wornat, M. J., R. H. Hurt, K. A. Davis and N. Y. C. Yang. Single-Particle Combustion of Two Biomass Chars. Twenty-Sixth Symposium (International) on Combustion / The Combustion Institute 3075-3083 (1999).

Zhang, X., A. Dukhan and I. I. Kantorovich. Structural changes of char particles during chemically controlled oxidation. Twenty-Sixth Symposium (International) on Combustion / The Combustion Institute, Napoli, Italy, **2** 3111-3118 (1996).

Appendix A Sawdust Sample Preparation Procedure

- *Step 1 Separation with sieve shaker* ---- This step preliminarily separates the sample by size. A series of standard sieves were put in a sieve shaker in order from 25 to 80 mesh, with the 80 mesh sieve at the bottom of the stack. The top sieve is filled with sawdust particles and the sieve shaker operates for 40 – 45 minutes. Samples left in each sieve are collected in sample bags respectively.
- *Step 2 Aerodynamic classification* ---- A tunnel separator was built to aerodynamically classify sawdust samples by shape and density (**Error! Reference source not found.**). Compressed air is introduced from the air inlet at the bottom of the air distribution pipe. Sawdust particles are fed from the top of the tunnel. Drag forces and gravity determine the trajectory of each particle. Less dense and fuzzy particles end up in tray four or out the end of the tunnel. Trays two and three are normally mixed together and used to get flakes and cylinders, while tray one is used to primarily get cubical/spherical particles. Samples collected in these four trays may have to run through the tunnel separator more than once.
- *Step 3 Shape separation by sieve*---- In this step, samples collected with the tunnel separator in tray one, tray two, and tray three are separated into near-spherical, flake-like, and cylinder-like particles. While shaking the sieve with samples in, particles with smaller aspect ratios fall through the sieve before

the larger ones. Based on the residence time difference, particles with different shapes and aspect ratios can be separated. Usually near-spherical particles are pass through the sieve most quickly, followed by flake-like and cylinder-like particles. Samples with different residence time are collected separately.

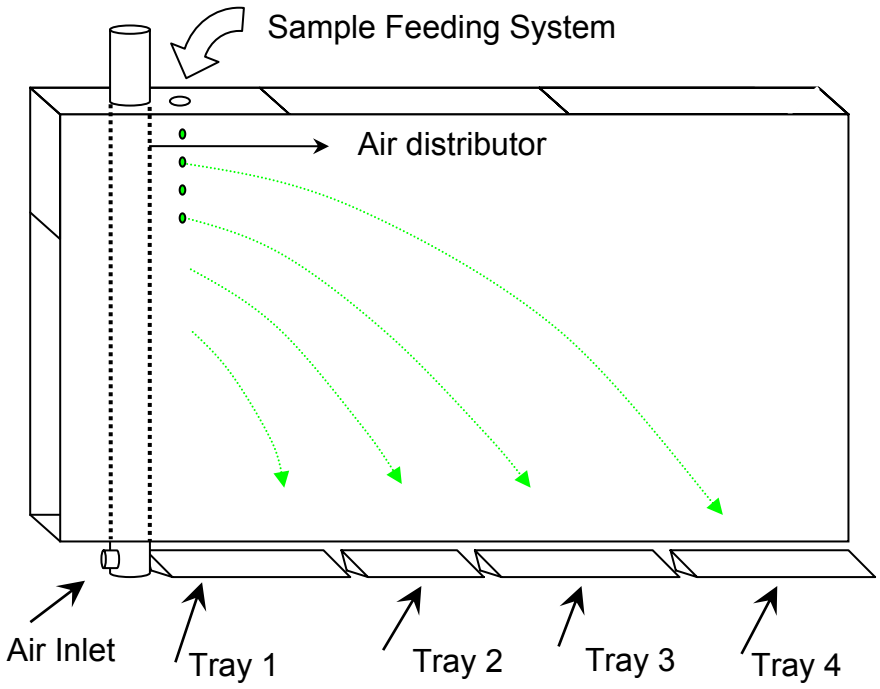

Figure 108 Tunnel separator schematic diagram

- *Step 4* *Further shape separation by friction plate* ---- A two-foot-long board with 600 grit sand paper along the length of it refines the particle shape separation so that more uniform particles with specific shape and size can be obtained,. The board is held at about a thirty degree angle and one or two grams of sample are poured at the top. Sawdust samples proceed to fall the length of the board, with only the most cubical/spherical particles making it

all the way to the bottom. The sand paper has the effect of increasing the frictional resistance to the sawdust particles. Those with the smallest surface-area-to-volume ratio travel the furthest along the length of the board.

Parts or all of these procedures sometimes must be repeated to improve separation.

Appendix B Spectral Responsivity Data of the CCD Camera

Spectral responsivity data of the CCD camera

Red channel		Green channel		Blue channel	
Wavelength	Response	Wavelength	Response	Wavelength	Response
0.35	0	0.35	0	0.35	0
0.353	0	0.353	0.00181	0.353	0.0065
0.369	0	0.368	0.013	0.37	0.068
0.386	0	0.386	0.024	0.386	0.149
0.394	0	0.394	0.026	0.392	0.e196
0.405	0	0.404	0.032	0.403	0.24
0.412	0.00157	0.412	0.036	0.411	0.304
0.419	0.00214	0.419	0.04	0.42	0.374
0.438	0.00488	0.438	0.054	0.429	0.455
0.449	0.00723	0.449	0.067	0.444	0.563
0.459	0.00895	0.458	0.076	0.453	0.68
0.468	0.00952	0.468	0.099	0.467	0.724
0.476	0.00952	0.476	0.143	0.479	0.701
0.484	0.01	0.484	0.229	0.49	0.563
0.492	0.013	0.492	0.36	0.495	0.482
0.502	0.016	0.502	0.539	0.502	0.325
0.516	0.024	0.513	0.721	0.516	0.199
0.529	0.029	0.524	0.845	0.529	0.116
0.54	0.026	0.54	0.906	0.54	0.057
0.55	0.023	0.553	0.859	0.55	0.035
0.56	0.032	0.563	0.785	0.56	0.016

0.57	0.136	0.57	0.683	0.57	0.016
0.58	0.572	0.58	0.569	0.58	0.012
0.59	0.919	0.59	0.419	0.59	0.00679
0.6	1	0.6	0.248	0.6	0.00588
0.61	0.997	0.61	0.12	0.61	0.00197
0.62	0.96	0.62	0.065	0.62	6.83E-04
0.63	0.941	0.63	0.045	0.63	9.16E-04
0.64	0.908	0.64	0.036	0.64	7.58E-04
0.65	0.88	0.65	0.03	0.65	8.44E-04
0.66	0.831	0.66	0.031	0.66	0.00202
0.67	0.784	0.67	0.039	0.67	0.00219
0.68	0.734	0.68	0.058	0.68	0.00284
0.69	0.705	0.69	0.086	0.69	0.00387
0.699	0.658	0.7	0.114	0.7	0.00464
0.71	0.623	0.71	0.126	0.71	0.00375
0.72	0.595	0.72	0.12	0.72	0.00276
0.73	0.55	0.73	0.113	0.73	0.00234
0.74	0.52	0.74	0.125	0.74	0.00345
0.75	0.471	0.75	0.144	0.75	0.00399
0.76	0.439	0.76	0.156	0.76	0.00396
0.77	0.397	0.77	0.164	0.77	0.00469
0.78	0.352	0.78	0.177	0.78	0.011
0.79	0.323	0.79	0.189	0.79	0.046
0.8	0.3	0.8	0.2	0.8	0.123
0.81	0.271	0.81	0.205	0.81	0.178
0.82	0.238	0.82	0.199	0.82	0.189
0.83	0.219	0.829	0.193	0.83	0.19
0.84	0.207	0.84	0.188	0.84	0.185
0.85	0.193	0.849	0.182	0.85	0.178
0.86	0.183	0.859	0.175	0.859	0.172
0.87	0.172	0.87	0.165	0.87	0.162

0.88	0.16	0.88	0.155	0.88	0.152
0.89	0.147	0.89	0.143	0.89	0.141
0.9	0.135	0.9	0.131	0.9	0.13
0.911	0.126	0.91	0.123	0.91	0.121
0.92	0.117	0.92	0.114	0.92	0.113
0.93	0.104	0.93	0.102	0.93	0.101
0.94	0.093	0.94	0.091	0.94	0.09
0.95	0.084	0.95	0.082	0.95	0.08
0.96	0.071	0.96	0.07	0.96	0.069
0.97	0.061	0.97	0.06	0.97	0.059
0.98	0.051	0.98	0.05	0.98	0.049
0.99	0.043	0.99	0.041	0.99	0.041
1	0.035	1	0.034	1	0.034
1.01	0.029	1.01	0.029	1.01	0.028
1.02	0.023	1.02	0.023	1.02	0.022
1.03	0.018	1.03	0.017	1.03	0.017
1.04	0.014	1.04	0.013	1.04	0.013
1.05	0.01	1.049	0.01	1.05	0.00991
1.06	0.0079	1.06	0.0077	1.06	0.00774
1.07	0.00596	1.07	0.00577	1.07	0.00566
1.08	0.00471	1.08	0.00451	1.08	0.00441
1.09	0.00368	1.09	0.0036	1.09	0.00358
1.1	0.0028	1.1	0.0025	1.1	0.0022
1.11	0.00221	1.11	0.002	1.11	0.0018
1.13	0.00123	1.13	0.0012	1.13	0.00115
1.15	0	1.15	0	1.15	0

Appendix C Limitations and Accuracy of the Particle Shape Reconstruction Algorithm

When creating tetrahedrals out of the interpolated points, concavity presents a challenge. When modeling a hand, for example, the tetrahedralization algorithm does not know where the edge of one finger begins and the other starts. This results in a volume and surface area that would include the space between the fingers as well as an inaccurate surface area and surface rendering. This challenge might be resolved with the idea that every object with concavity can be broken down into smaller convex objects.

The current algorithm needs to know the orientation of the camera with which the three images are taken and the three images have to be taken from three orthogonal directions.

To examine the accuracy of this algorithm for a randomly shaped particle with respect of volume and surface area, two pieces of randomly chosen rocks were used since it is difficult to directly measure small sawdust particle. The volumes of the two rocks were measured with containers filled with water and the surface areas were measured with paper wrapped around the rock surface. The surface-area to volume ratios of the two rocks were calculated using the particle shape reconstruction algorithm with several sets of images taken from different positions, and compared with measured results in Figure 109. Errors of the current algorithm appear in Figure 110. Results show that the average

volume calculation error is - 5.1 % and the average surface area calculation error is + 6.2 %. So it results in an average surface-area to volume ratio error of about 10.3 %.

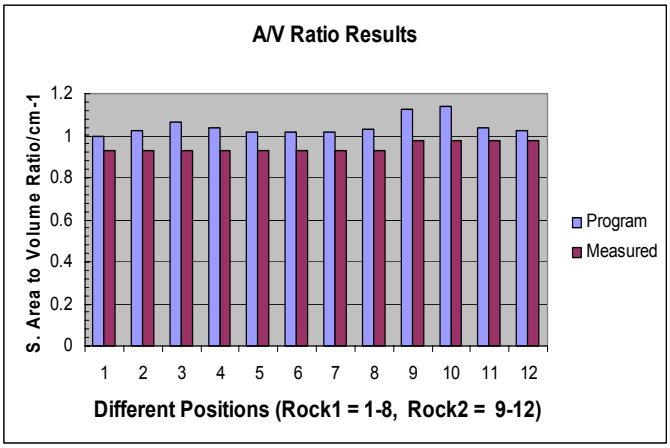

Figure 109 Comparisons of measured and calculated surface-area to volume ratios for two rocks

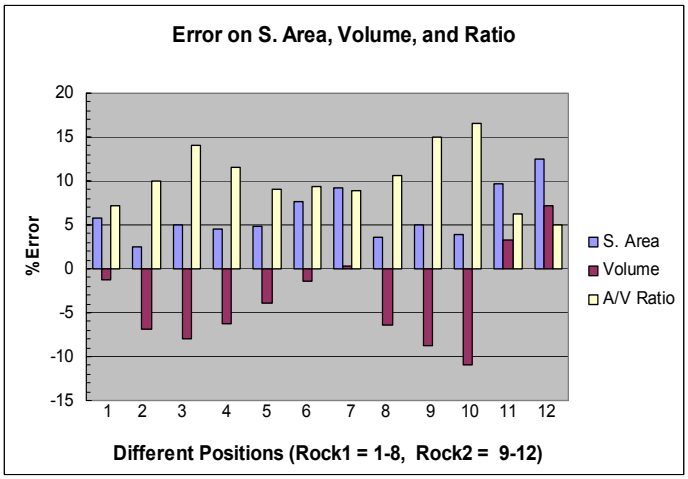

Figure 110 Error analysis of surface area, volume, and surface-area to volume ratio